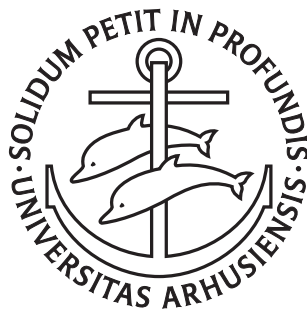

STRONG-FIELD IONIZATION OF TWO-ELECTRON MODEL ATOMS

CHUAN YU

PHD THESIS

SEPTEMBER 2017

SUPERVISOR: LARS BOJER MADSEN



DEPARTMENT OF PHYSICS AND ASTRONOMY
AARHUS UNIVERSITY

English Summary

With the rapid development of laser technology, it is nowadays possible to produce intense laser pulses with frequencies ranging from the terahertz to the X-ray regimes. When a multi-electron atom is irradiated by such intense laser pulses, it can undergo various ionization processes, ending up with an ion plus one or more free electrons. The knowledge about such strong-field ionization processes is of fundamental interest, because it can provide the possibility to understand the structure and dynamics of the microscopic world.

This thesis considers two-electron model atoms as typical examples of multi-electron atoms, and discusses theoretical studies on the strong-field ionization of two-electron model atoms. The theoretical research basically relies on numerical solution of the time-dependent Schrödinger equation and extraction of continuum observables, for which some efficient numerical methods are implemented. The ionization of two-electron model atoms is classified into different channels, including single ionization with different ionic states and double ionization. The main focus of this thesis is the strong-field phenomena among different ionization channels, in both the extreme-ultraviolet and the near-infrared regimes. To explain the new findings and discover the underlying mechanisms, several theoretical approaches are applied for analyzing the results.

Dansk Resumé

Med den hurtige udvikling af laserteknologi er det nu blevet muligt at skabe intense laserpulser med frekvenser fra terahertz til Røngtenområdet. Når et mange-elektron atom bliver bestrålet med sådanne intense laserpulser, kan det undergå forskellige ionisationsprocesser ledende til en ion med en eller flere frie elektroner. Viden omkring sådanne stærkfelts-ionisationsprocesser er af fundamental interesse, da de kan give mulighed for at forstå strukturen og dynamikken i den mikroskopiske verden.

Denne afhandling omhandler to-elektron modelatomer, som typiske eksempler på mange-elektron atomer, og diskuterer teoretiske studier af stærkfeltsionisation af to-elektron modelatomer. Den teoretiske forskning afhænger af numeriske løsninger af den tidsafhængige Schrödingerligning og ekstraktion af kontinuumsobservable til hvilket nogle effektive numeriske metoder er implementeret. Ionisation af to-elektron modelatomer er klassificeret i forskellige kanaler, så som enkeltionisation med forskellige ioniske tilstande og dobbeltionisering. Hovedfokus i denne afhandling er stærkfeltsfænomener heriblandt forskellige ionisationskanaler i det ekstremt ultraviolette og nærinfrarøde område. For at forklare de nye opdagelser og for at finde de underlæggende mekanismer, bliver adskillige metoder anvendt til at analysere resultaterne.

Preface

This thesis summarizes some of the work I have done during my PhD studies at the Department of Physics and Astronomy, Aarhus University, Denmark. The studies were carried out from October 2014 to September 2017, under the supervision of Professor Lars Bojer Madsen.

Notations

Atomic units ($\hbar = m_e = -q_e = 4\pi\epsilon_0 = 1$) are used throughout the thesis, unless explicitly stated otherwise.

Acknowledgments

First of all, I would like to thank my supervisor Lars Bojer Madsen for providing me the opportunity to carry out my PhD studies in his group at Aarhus University. Lars is always kind, patient and enthusiastic, and gives me excellent guidance during my research.

Also, I thank Wenliang Li for his warm-hearted help when I arrived at Aarhus for the first time, Haruhide Miyagi and Siddhartha Chattopadhyay for giving me an introduction to some time-dependent many-body theories when I started as a beginner. I am very thankful to Lun Yue, who shares his knowledge about physics, numerics, and many other topics with me. I am also grateful to the group members I have met in the past three years: it is enjoyable to work with all of you. A special thank goes to Kenneth Hansen for helping me with the Dansk Resumé. In addition, I wish to express my gratitude to Liangyou Peng for hosting me when I visited his group at Peking University.

At last, thanks to my family and friends for their constant support.

*Chuan Yu,
September 29, 2017.*

List of Abbreviations

SAE	single-active-electron
SFA	strong-field approximation
ATI	above-threshold ionization
LIED	laser-induced electron diffraction
NIR	near-infrared
MIR	mid-infrared
XUV	extreme ultraviolet
KH	Kramers-Henneberger
HFFT	high-frequency Floquet theory
TDSE	time-dependent Schrödinger equation
IMST	intense-field many-body S-matrix theory
NSDI	non-sequential double ionization
TPDI	two-photon double ionization
tSURFF	time-dependent surface flux
VG	velocity gauge
LG	length gauge
3D	three-dimensional
1D	one-dimensional
ITP	imaginary time propagation
DVR	discrete variable representation
FEDVR	finite-element discrete variable representation
CAP	complex absorbing potential
ECS	exterior complex scaling
irECS	infinite-range exterior complex scaling
SPDI	single-photon double ionization
SPM	saddle-point method
MCTDHF	multi-configuration time-dependent Hartree-Fock
TDCIS	time-dependent configuration-interaction singles
TD-RASSCF	time-dependent restricted-active-space self-consistent-field
TD-GASCI	time-dependent generalized-active-space configuration-interaction

Contents

Preface	iii
Part One Overview	1
1 Introduction	3
1.1 Strong-field Concepts	3
1.2 Two-electron Problems	7
1.3 Thesis Outline	10
2 Theory for Modeling Atoms in Laser Fields	11
2.1 Non-relativistic Time-dependent Hamiltonian	11
2.2 Dipole Approximation and Gauges	12
2.3 Separation of Center-of-mass Motion	14
2.4 Reduced-dimensional Models	17
3 Numerical Methods for Solving the TDSE	19
3.1 Generic Concepts for Time-evolution	19
3.2 Discretization of Wave Function	21
3.3 Krylov-subspace Time Propagator	29
3.4 Absorbing Boundary Conditions	31
3.5 One-dimensional TDSE Examples	39
4 Extraction of Continuum Information	45
4.1 One-electron Time-dependent Surface Flux Method	46
4.2 Two-electron Time-dependent Surface Flux Method	49
4.3 Suppression of Rydberg-state Contributions	52
4.4 One-dimensional Examples of the tSURFF Method	53
5 Ionization of Helium in the XUV Regime	59
5.1 Motivation	59
5.2 Theory and Main Findings	60
5.3 Concluding Remarks	63

6 Ionization of Helium in the NIR Regime	65
6.1 Motivation	65
6.2 Theory and Main Findings	66
6.3 Concluding Remarks	69
7 Summary and Outlook	71
Part Two Publications	75
Paper I. Physical Review A 93, 043412 (2016)	77
Paper II. Physical Review A 94, 053424 (2016)	85
Paper III. Physical Review A 95, 063407 (2017)	95
Copyright Licenses	105
Bibliography	115

PART ONE
OVERVIEW

Introduction

Our knowledge about the light-matter interaction lays an important foundation for understanding the structure and dynamics of the microscopic world. With Albert Einstein's concept of light quanta (known as photons nowadays) in 1905, Niels Bohr's atomic model in 1913, and the development of quantum mechanics in the 20th century, numerous breakthroughs have been made in the research area of the interaction of atoms with electromagnetic fields.

Since the first laser^[i] built by Theodore Maiman in 1960 [1], the utilization of such a coherent light source has been developed into a powerful and popular tool for investigating the properties of atoms and molecules. As the laser technology has been significantly advanced during the past decades, new light sources with field strengths comparable to the Coulomb interaction in atoms and molecules are readily available. Thus our research on the laser-matter interaction is driven into a strong-field regime, where the perturbative treatment of the external fields is no longer applicable.

The strong-field laser-matter interactions result in a number of non-linear and non-perturbative phenomena, which stimulate the continuous development of the theoretical methods in the strong-field regime. In addition to expanding and deepening our theoretical knowledge about the laser-matter interactions, the studies in the strong-field regime also give birth to new experimental techniques for monitoring ultrafast processes in atomic and molecular systems. For example, the pump-probe schemes based on ultrashort laser pulses with durations in the femtosecond or even the attosecond time regime, open up the possibility to observe and to control dynamics of atoms and molecules on their natural time scales [2].

1.1 Strong-field Concepts

First of all, we will briefly introduce some fundamental concepts in the strong-field physics, which are closely related to the topics of this thesis. Since this thesis mainly discusses on strong-field ionization processes, here we only focus on several

^[i]The term "laser" originated from an acronym for "light amplification by stimulated emission of radiation".

strong-field concepts about ionization, among numerous strong-field phenomena. For simplicity, the introduction in this section is restricted to a single-active-electron (SAE) scenario. Possible extension of these strong-field concepts beyond the SAE picture will be further discussed in §1.2.

Multi-photon Ionization

Multi-photon ionization, which results from the simultaneous absorption of several photons, is a generalization of the well-known photoelectric effect that is induced by a single photon. The possibility of multi-photon transitions was theoretically predicted by Maria Göppert-Mayer in 1931. Since the cross sections for multi-photon transitions are typically very small, the experimental observation requires an intense light source, which was not available at that time. After the invention of laser, the experimental observation of multi-photon ionization was for the first time achieved in the 1960s [3, 4].

According to the perturbation theory, the scaling law of multi-photon ionization says that the \mathcal{K} -photon ionization rate $\mathcal{R}_{\mathcal{K}}$ (in units of s^{-1}) is proportional to the \mathcal{K} -th power of the laser photon flux Φ (the laser intensity I divided by the photon energy $\hbar\omega$), i.e.,

$$\mathcal{R}_{\mathcal{K}} = \sigma_{\mathcal{K}} \Phi^{\mathcal{K}} = \frac{\sigma_{\mathcal{K}}}{(\hbar\omega)^{\mathcal{K}}} I^{\mathcal{K}} \quad (1.1)$$

with $\sigma_{\mathcal{K}}$ the generalized cross section (in units of $\text{cm}^{2\mathcal{K}}\text{s}^{\mathcal{K}-1}$) [5].

Tunneling and Barrier-suppression Ionization

In some cases the ionization processes can be elucidated from a quasi-static point of view. In the presence of an intense electric field, the potential barrier of an atom is drastically distorted. As described by quantum mechanics, the electron has probability to escape from the deformed potential barrier. The ionization is termed as tunneling if the initial electron energy is lower than the potential barrier, which implies that electron escape is forbidden by classical mechanics. If the initial electron energy is higher than the distorted potential barrier, the ionization is in the barrier-suppression (or over-the-barrier) regime [6–10].

The tunneling ionization rate of the ground-state Hydrogen atom in the presence of a static electric field was solved by Lev Landau and Evgeny Lifshitz [11]. Later it was generalized to an arbitrary atom in alternating electromagnetic fields [12]. For an alternating electric field with field strength F_0 , the cycle-averaged tunneling ionization rate \mathcal{R}_T is proportional to the same exponential factor in the static case,

i.e.,

$$\mathcal{R}_T \propto \exp \left[-\frac{2}{3} \frac{(2I_p)^{3/2}}{F_0} \right] \quad (1.2)$$

with I_p the ionization potential. In the quasi-static case, the tunneling ionization occurs mainly at the times when the electric field reaches its maxima.

Keldysh Parameter

In order to classify different ionization regimes, Leonid Keldysh [13] introduced a dimensionless parameter γ , which can be interpreted as the ratio between the characteristic time of tunneling through the barrier and the time period of the alternating external field. In the presence of an alternating electric field with field strength F_0 and angular frequency ω , a free electron has cycle-averaged quiver energy given by

$$U_p = \frac{F_0^2}{4\omega^2}, \quad (1.3)$$

which is termed as the ponderomotive potential. Then the Keldysh parameter γ is often expressed in terms of the ionization potential I_p and the ponderomotive potential U_p as

$$\gamma = \sqrt{\frac{I_p}{2U_p}}. \quad (1.4)$$

The quasi-static tunneling (or barrier-suppression) picture is valid for $\gamma \ll 1$, which means that the electron has sufficient time to escape from the barrier due to the slow variance of the external field. For the opposite case $\gamma \gg 1$, the ionization is considered to happen in the multi-photon regime.

Strong-field Approximation

On the basis of the Keldysh theory [13], an important analytical approach called the strong-field approximation (SFA) has been developed and widely applied for describing strong-field phenomena. The SFA approach, which is also known as the Keldysh-Faisal-Reiss theory [13–15], describes the transition amplitude between an initial bound state and a final continuum state^[iii]. The key idea of the SFA is to represent the continuum state with a Volkov state, which is the solution for a free electron moving in the presence of the laser field (with the Coulomb interaction neglected). In this introduction, here we prefer not to present detailed formulas for

^[iii]The SFA theory has been extended to some strong-field effects such as high-order harmonic generation [16, 17], where the considered final state is not a continuum state. In this thesis, however, we focus on the SFA for describing the ionization processes.

the SFA theory. For more discussions about the SFA formulation and applications, we refer to a review article [18].

It is worth mentioning that the SFA approach is still under investigation and modification. It is well known that the traditional SFA [13–15] has some drawbacks such as the neglect of Coulomb effects. There have been a few studies aiming at improving the SFA (see, e.g., Refs. [19–27]). The improved SFA methods, are expected to provide more insights into the strong-field physics.

Above-threshold Ionization

Above-threshold ionization (ATI), which was for the first time observed in 1979 [28], is a strong-field phenomenon where the photoelectron absorbs more photons than the minimum required for ionization.

There have been numerous experimental and theoretical studies performed to explore the ATI spectral features (see, e.g., Refs. [29–31] for reviews). When irradiated by an intense laser field, a bound electron may be freed, drift away from the ion, and directly contribute to the low-energy part of the ATI spectrum. The final energy of this direct electron is typically below $2U_p$, where U_p is the ponderomotive energy defined by Eq. (1.3). Alternatively the freed electron may be driven back to the ion by the laser field and rescatter^[iii]. The back-scattered electron will gain more energy than the direct electron and contribute to the plateau-like high-energy part of the ATI spectrum, typically ranging from $2U_p$ to $10U_p$. The high-energy photoelectron can be used for ultrafast imaging. One example application is the laser-induced electron diffraction (LIED) [33], which is a time-resolved molecular self-imaging technique of extracting structural information from strong-field-induced rescattering.

With recent development of laser sources in the long-wavelength regime, an “unexpected” low-energy structure was discovered in the ATI spectrum [34]. This causes great surprise and new interest in the investigation of the ATI (see, e.g., Refs. [35–42]). According to the corresponding theoretical studies in recent years, the low-energy structure in the ATI spectrum is usually considered as a feature of the forward-scattered electrons, and the ionic Coulomb potential plays an important role in this phenomenon. Also, research on the interference between the scattered and unscattered photoelectron gives birth to an ultrafast imaging technique called strong-field holography [43].

Note that the above introduction of the ATI in the rescattering scenario is mainly restricted in the long-wavelength [e.g., near-infrared (NIR) or mid-infrared (MIR)] regime. In the short-wavelength [e.g., extreme-ultraviolet (XUV) or X-ray] regime,

^[iii]This is the well-known three-step model [32] in the strong-field physics.

the discrete ATI peaks in the photoelectron spectrum can be easily elucidated from the multi-photon picture.

Atomic Stabilization

Atomic stabilization is a strong-field effect in the short-wavelength regime, where the ionization rate does not follow Eq. (1.1) predicted by the perturbation theory, but “counter-intuitively” shows a decreasing trend with increasing laser intensity. This phenomenon typically requires the photon energy $\hbar\omega$ to be larger than the ionization potential I_p . It was first discovered by theoretical calculations [44, 45], and later confirmed by a few experiments performed on Rydberg atoms [46–50].

A mainstream theoretical explanation for atomic stabilization is based on the Kramers-Henneberger (KH) frame [51] and high-frequency Floquet theory (HFFT) [52]. The KH frame is an oscillating frame for the time-dependent Schrödinger equation (TDSE), where the laser-field interaction is described by a time-dependent potential. For example, in the presence of a monochromatic electric field linearly polarized in the \hat{e} -direction

$$\mathbf{F}(t) = \hat{e}F_0 \cos(\omega t), \quad (1.5)$$

a classical electron in the laboratory frame has a quiver motion

$$\boldsymbol{\alpha}(t) = \hat{e}\alpha_0 \cos(\omega t), \quad (1.6)$$

with the quiver radius

$$\alpha_0 = \frac{F_0}{\omega^2}. \quad (1.7)$$

The laser interaction in the KH frame is then represented by an oscillating potential $V[\mathbf{r} + \boldsymbol{\alpha}(t)]$, which means that the classical electron is considered to be at rest in the KH frame. The ionization rate can be extracted from the quasi-stationary solutions within the Floquet approach [53, 54]. In the case of a high-frequency field, the key idea of the HFFT is to solve the Floquet system by successive iterations of increasing order in ω^{-1} . For more topics on stabilization and details about the HFFT approach, we refer to two review articles [55, 56].

We note by passing that the quiver radius α_0 defined by Eq. (1.7) is also an important parameter for numerical simulations of the TDSE, i.e., the simulation volume should be large enough to ensure that the electron quiver motion is correctly simulated.

1.2 Two-electron Problems

The strong-field physics would be much more complicated if one goes beyond the SAE picture. Although the SAE picture is still valid for some strong-field processes

in multi-electron systems, there do exist some multi-electron effects that cannot be explained by the SAE model. For better understanding of the multi-electron effects, we can start by investigating a two-electron system, which is a typical and simple example of multi-electron systems. In this section we will briefly discuss some two-electron problems that are of interest in the strong-field ionization.

Regarding the strong-field ionization, one of the most important features of a multi-electron system is that it has multiple continua corresponding to different ionic states, which are also referred to as ionization channels. According to the perturbation theory, the multi-photon rate of the form Eq. (1.1) can be generalized for the description of multiple ionization and excitation [57, 58]. In some cases, the multi-photon rate-equation approach is actually applicable for describing the multi-electron systems irradiated by intense laser fields, especially in the high-frequency regime (see, e.g., Refs. [59–62]). The multi-electron dynamics in the strong-field regime, however, may be far more interesting than the rate-equation description.

Note that the SFA theory introduced in §1.1 can be generalized to multi-electron systems, i.e., the so-called intense-field many-body S-matrix theory (IMST) [63]. The IMST is a systematic approach to calculate the transition amplitude from an initial state to a final state, which can be applied to analyze two-electron dynamics (see, e.g., Refs. [64–67]).

Double Ionization

Laser-induced double ionization, where two electrons are freed by intense laser fields, is one of the most representative two-electron problems. Typically, the research interest in double ionization includes the dependence of double ionization probability on laser parameters, the role of the electron correlation, the energy-sharing between the two electrons, and also the corresponding mechanisms and dynamics.

Double ionization can be classified into two categories: sequential and non-sequential. In the sequential mechanism, the SAE picture interprets the ionization as two uncorrelated steps. In the non-sequential mechanism, where the two electrons are strongly correlated, the SAE picture fails. The observation of non-sequential double ionization (NSDI) [68–70] has stimulated the development of theoretical methods beyond the SAE model (see, e.g., Ref. [71] for a review). Note that this NSDI concept usually refers to the long-wavelength regime, where the corresponding theoretical explanation is based on the tunneling and rescattering picture. In the short-wavelength regime where the photon-energy picture is more useful, there also exist sequential and non-sequential mechanisms to be investigated. For example, the mechanisms of two-photon double ionization (TPDI) have caused great interest in recent years (see, e.g., Refs. [72–76]).

In addition to the double ionization probability as a function of laser parameters, the correlated photoelectron energy spectrum (or momentum distribution) may contain more information about the underlying two-electron dynamics. Note that the ATI concept introduced in §1.1 can be extended to the double ionization case. As predicted by theoretical calculations [77, 78] and observed by recent experiments [79, 80], the correlated photoelectron energy spectra for double ionization also contain the discrete ATI-peak structures.

Single Ionization

Single ionization of a multi-electron system is also an interesting topic, since there are many different singly-ionized continua involved. The ATI concept introduced in §1.1 is still valid for single ionization of a multi-electron system. In the multi-electron case, however, the photoelectron should be characterized by a series of ATI spectra corresponding to different ionization channels, i.e., the channel-resolved ATI [81, 82]. As demonstrated in Ref. [82], the channel-resolved ATI can serve as a useful tool for probing the multiple continua participation in the strong-field dynamics of polyatomic molecules.

With the advances of attosecond technology, attosecond-scale time-delays in the photoelectron emission can be determined (see, e.g., Ref. [2, 83] for reviews). Such ultrafast information can be extracted from the photoelectron energy spectra by the attosecond streaking scheme [84], which may provide insight into the electron correlation in multi-electron systems [85]. For example, a recent paper [86] reported the attosecond streaking spectroscopy applied to helium, and the authors recorded the relative timing difference between different single ionization channels. The role of the electron correlation was found to be reflected as a correlation-induced time shift, which indicates the breakdown of the SAE model.

Stabilization of Two-electron Atoms

As introduced in §1.1, atomic stabilization typically happens in the high-frequency regime where the photon energy $\hbar\omega$ is larger than the ionization potential I_p . In two-electron atoms, the multiple ionization channels have different values of I_p , which make the high-frequency condition ($\hbar\omega > I_p$) obscure. Also, the concept of stabilization needs to be clarified for two-electron atoms, i.e., it is usually considered with respect to the total ionization probability. In principle, one can investigate the laser-intensity dependence of the total, double and single ionization probability, or even the channel-resolved ionization probabilities. However, one may refrain from using the term “stabilization” for specific ionization channels, since the system may not be actually “stabilized” in terms of the total ionization probability.

Extension of the HFFT to the two-electron case predicted that stabilization could occur in two-electron atoms [87]. By performing numerical simulations of the TDSE, some researchers found that stabilization of two-electron atoms indeed happens for high-energy photons that exceed all the ionization potentials [88–90]. The authors also discussed the role of the electron correlation, and concluded that the electron correlation would reduce the stabilization effect.

1.3 Thesis Outline

This thesis covers some theoretical studies on strong-field ionization of two-electron model atoms. It contains two parts: **Part One** provides an overview of the discussed topics while **Part Two** is composed of our publications [91–93] that are related to this thesis. The remaining chapters of **Part One** are organized as follows:

- **Chapter 2** introduces the non-relativistic TDSE for modeling atoms in laser fields, and discusses some approximations and models that are usually used in the TDSE approach.
- **Chapter 3** introduces some numerical aspects of *ab initio* TDSE calculations, including numerical techniques for discretization, time propagation, and absorbing boundary conditions.
- **Chapter 4** introduces the time-dependent surface flux (tSURFF) method for extracting continuum information from the TDSE calculations, which is the key tool used in our studies on strong-field ionization.
- **Chapter 5** discusses the strong-field ionization of model helium in the short-wavelength (XUV) regime, and gives an overview of our published papers [91, 92].
- **Chapter 6** discusses the strong-field ionization of model helium in the long-wavelength (NIR) regime, and gives an overview of our published paper [93].
- **Chapter 7** summarizes our research, concludes this thesis, and gives a brief outlook.

Note that although each publication in **Part Two** is self-consistent, the abbreviations and notations used in the published papers may differ from those used in **Part One**. Apart from this exception, the whole thesis is written in a self-consistent manner.

Theory for Modeling Atoms in Laser Fields

2.1 Non-relativistic Time-dependent Hamiltonian

To theoretically describe laser-matter interaction in the non-relativistic regime, we consider the time-dependent Schrödinger equation (TDSE) as the starting point. For generality, we consider a many-body system consisting of \mathcal{N} charged particles with Coulomb interaction in between. If the system is not subjected to any external field, its field-free Hamiltonian reads

$$\tilde{H}_0 = \sum_{J=1}^{\mathcal{N}} \frac{\tilde{\mathbf{p}}_J^2}{2m_J} + \sum_{J=1}^{\mathcal{N}} \sum_{K>J}^{\mathcal{N}} \frac{q_J q_K}{|\tilde{\mathbf{r}}_J - \tilde{\mathbf{r}}_K|}, \quad (2.1)$$

where m_J , q_J , $\tilde{\mathbf{r}}_J$ and $\tilde{\mathbf{p}}_J$ are the mass, charge, coordinate and momentum of the J -th particle. If the system is exposed to strong laser fields, we can treat the external electromagnetic fields classically. According to classical electrodynamics, the electric field $\mathbf{F}(\mathbf{r}, t)$ and the magnetic field $\mathbf{B}(\mathbf{r}, t)$ can be expressed in terms of a scalar potential $\phi(\mathbf{r}, t)$ and a vector potential $\mathbf{A}(\mathbf{r}, t)$ ^[1]

$$\mathbf{F}(\mathbf{r}, t) = -\frac{\partial}{\partial \mathbf{r}} \phi(\mathbf{r}, t) - \frac{\partial}{\partial t} \mathbf{A}(\mathbf{r}, t), \quad (2.2)$$

$$\mathbf{B}(\mathbf{r}, t) = \frac{\partial}{\partial \mathbf{r}} \times \mathbf{A}(\mathbf{r}, t). \quad (2.3)$$

For the system coupled with $\mathbf{A}(\mathbf{r}, t)$ and $\phi(\mathbf{r}, t)$, the time-dependent Hamiltonian in the minimal-coupling scheme reads

$$\begin{aligned} \tilde{H}(t) &= \sum_{J=1}^{\mathcal{N}} \frac{[\tilde{\mathbf{p}}_J - q_J \mathbf{A}(\tilde{\mathbf{r}}_J, t)]^2}{2m_J} + \sum_{J=1}^{\mathcal{N}} q_J \phi(\tilde{\mathbf{r}}_J, t) + \sum_{J=1}^{\mathcal{N}} \sum_{K>J}^{\mathcal{N}} \frac{q_J q_K}{|\tilde{\mathbf{r}}_J - \tilde{\mathbf{r}}_K|} \\ &= \tilde{H}_0 + \tilde{V}_I(t), \end{aligned} \quad (2.4)$$

^[1]In this thesis, we use the notation $\frac{\partial}{\partial \mathbf{r}}$ for the del (nabla) operator ∇ .

where $\tilde{V}_I(t)$ is the laser-interaction term

$$\tilde{V}_I(t) = \sum_{J=1}^{\mathcal{N}} \frac{-q_J [\tilde{\mathbf{p}}_J \cdot \mathbf{A}(\tilde{\mathbf{r}}_J, t) + \mathbf{A}(\tilde{\mathbf{r}}_J, t) \cdot \tilde{\mathbf{p}}_J] + q_J^2 |\mathbf{A}(\tilde{\mathbf{r}}_J, t)|^2}{2m_J} + \sum_{J=1}^{\mathcal{N}} q_J \phi(\tilde{\mathbf{r}}_J, t). \quad (2.5)$$

There exists a gauge freedom in the choice of the scalar and vector potentials $\phi(\mathbf{r}, t)$ and $\mathbf{A}(\mathbf{r}, t)$, i.e., the electromagnetic fields $\mathbf{F}(\mathbf{r}, t)$ and $\mathbf{B}(\mathbf{r}, t)$ remain unchanged under the gauge transformation

$$\phi(\mathbf{r}, t) \rightarrow \phi(\mathbf{r}, t) - \frac{\partial}{\partial t} \Lambda(\mathbf{r}, t), \quad (2.6)$$

$$\mathbf{A}(\mathbf{r}, t) \rightarrow \mathbf{A}(\mathbf{r}, t) + \frac{\partial}{\partial \mathbf{r}} \Lambda(\mathbf{r}, t). \quad (2.7)$$

We choose to work in the Coulomb gauge

$$\frac{\partial}{\partial \mathbf{r}} \cdot \mathbf{A}(\mathbf{r}, t) = 0, \quad (2.8)$$

and assume a source-free condition for the electromagnetic fields which gives

$$\phi(\mathbf{r}, t) = 0. \quad (2.9)$$

Thus the laser-interaction term has the simple form

$$\tilde{V}_I(t) = \sum_{J=1}^{\mathcal{N}} \frac{-2q_J \mathbf{A}(\tilde{\mathbf{r}}_J, t) \cdot \mathbf{p}_J + q_J^2 |\mathbf{A}(\tilde{\mathbf{r}}_J, t)|^2}{2m_J}. \quad (2.10)$$

2.2 Dipole Approximation and Gauges

For the description of laser fields, we may use a vector potential of the form

$$\mathbf{A}(\mathbf{r}, t) = \hat{\mathbf{e}} \tilde{A}_0(t) \frac{1}{2i} \left[\exp(+i\tilde{\mathbf{k}} \cdot \mathbf{r} - i\omega t) - \exp(-i\tilde{\mathbf{k}} \cdot \mathbf{r} + i\omega t) \right], \quad (2.11)$$

which is a solution to the Maxwell equations. Such a solution describes an $\hat{\mathbf{e}}$ -polarized laser pulse propagating with wave vector $\tilde{\mathbf{k}}$, angular frequency ω and time-domain envelope $\tilde{A}_0(t)$.

Very often we can assume that there is no spatial dependence of the laser fields over the considered system, which is known as the dipole approximation. Suppose that the considered system is confined in a small region where $\tilde{\mathbf{k}} \cdot \mathbf{r} \ll 1$ is satisfied, we can approximate $\exp(i\tilde{\mathbf{k}} \cdot \mathbf{r}) \approx 1$ and simply use

$$\mathbf{A}(t) = \hat{\mathbf{e}} \tilde{A}_0(t) \frac{1}{2i} \left[\exp(-i\omega t) - \exp(+i\omega t) \right] = \hat{\mathbf{e}} \left[-\tilde{A}_0(t) \sin(\omega t) \right], \quad (2.12)$$

for the vector potential. The electromagnetic fields (in the considered region) are given by

$$\mathbf{F}(t) = -\frac{\partial}{\partial t} \mathbf{A}(t), \quad (2.13)$$

$$\mathbf{B}(t) = 0. \quad (2.14)$$

Therefore the dipole approximation implies that any effect induced by the magnetic field is neglected.

Within the dipole approximation, there are various ways to formulate the \mathcal{N} -particle TDSE

$$i \frac{\partial}{\partial t} |\tilde{\Psi}(t)\rangle = \tilde{H}(t) |\tilde{\Psi}(t)\rangle. \quad (2.15)$$

In general, we can perform a unitary transformation on the state $|\tilde{\Psi}(t)\rangle$ to obtain a new state

$$|\tilde{\Psi}'(t)\rangle = \tilde{U}^\dagger(t) |\tilde{\Psi}(t)\rangle. \quad (2.16)$$

Then the TDSE for the new state $|\tilde{\Psi}'\rangle$ is

$$i \frac{\partial}{\partial t} |\tilde{\Psi}'(t)\rangle = \tilde{H}'(t) |\tilde{\Psi}'(t)\rangle = \left(\tilde{U}^\dagger(t) \tilde{H}(t) \tilde{U}(t) - i \tilde{U}^\dagger(t) \frac{\partial}{\partial t} \tilde{U}(t) \right) |\tilde{\Psi}'(t)\rangle. \quad (2.17)$$

Following the minimal-coupling scheme, the TDSE with the laser-interaction term

$$\tilde{V}_I(t) = \sum_{J=1}^{\mathcal{N}} \frac{-2q_J \mathbf{A}(t) \cdot \tilde{\mathbf{p}}_J + q_J^2 |\mathbf{A}(t)|^2}{2m_J}, \quad (2.18)$$

is referred to as velocity gauge (VG). On the basis of the VG TDSE, a unitary transformation [94]

$$\tilde{U}^\dagger(t) = \exp \left[i \mathbf{A}(t) \cdot \sum_{J=1}^{\mathcal{N}} q_J \tilde{\mathbf{r}}_J \right], \quad (2.19)$$

leads to a new Hamiltonian $\tilde{H}'(t) = \tilde{H}_0 + \tilde{V}'_I(t)$ with

$$\tilde{V}'_I(t) = -\mathbf{F}(t) \cdot \sum_{J=1}^{\mathcal{N}} q_J \tilde{\mathbf{r}}_J. \quad (2.20)$$

The TDSE with the laser interaction given by Eq. (2.20) is referred to as length gauge (LG), which is also frequently used for describing the laser interaction^[iii]. It

^[iii]For example, the tunneling picture introduced in §1.1 is actually based on the LG interaction.

can also be seen as a result of the gauge transformation on the scalar and vector potentials, i.e., choosing $\Lambda(\mathbf{r}, t) = -\mathbf{A}(t) \cdot \mathbf{r}$ in Eqs. (2.6) and (2.7) gives

$$\phi'(t) = 0 - \frac{\partial}{\partial t}[-\mathbf{A}(t) \cdot \mathbf{r}] = -\mathbf{F}(t) \cdot \mathbf{r}, \quad (2.21)$$

$$\mathbf{A}'(t) = \mathbf{A}(t) + \frac{\partial}{\partial \mathbf{r}}[-\mathbf{A}(t) \cdot \mathbf{r}] = 0. \quad (2.22)$$

In the VG TDSE with the laser interaction given by Eq. (2.18), the $|\mathbf{A}(t)|^2$ term can be unitarily transformed away. By performing a transformation [94]

$$\tilde{U}^\dagger(t) = \exp \left[i \sum_{J=1}^{\mathcal{N}} \frac{q_J^2}{2m_J} \int_{-\infty}^t dt' |\mathbf{A}(t')|^2 \right], \quad (2.23)$$

we obtain a simpler expression for the laser-interaction term

$$\tilde{V}'_I(t) = \sum_{J=1}^{\mathcal{N}} \frac{-q_J \mathbf{A}(t) \cdot \tilde{\mathbf{p}}_J}{m_J}. \quad (2.24)$$

The corresponding TDSE is referred to as reduced VG, which is convenient to use in practical calculations. Note that within the dipole approximation, the $|\mathbf{A}(t)|^2$ term simply corresponds to a shift in the energy scale. So it only contributes a global phase factor to the wave function, and does not contain any physical significance. We also note that the TDSE in different gauges will in principle produce equivalent results. In practical calculations, however, the numerical performance of different gauges may not be the same [95, 96].

Validity of Dipole Approximation

In fact, our theoretical studies presented in this thesis are all restricted within the dipole approximation. However, it is worth mentioning that the dipole approximation may break down in the strong-field ionization. It is already known that the breakdown of the dipole approximation can lead to non-dipole effects in both the short-wavelength [97, 98] and the long-wavelength [99, 100] regimes. The non-dipole effects are interesting in nature, but not the main focus of this thesis. In this thesis we discuss the strong-field ionization of two-electron model atoms within the commonly-used dipole approximation, and simply discard all the possible non-dipole effects.

2.3 Separation of Center-of-mass Motion

For the considered \mathcal{N} -particle system, the center-of-mass motion can be separated from the internal motion. This allows us to work with the TDSE of $(\mathcal{N} - 1)$ particles in practice.

By introducing the center-of-mass coordinate

$$\mathbf{R} = \frac{1}{\mathcal{M}} \sum_{J=1}^{\mathcal{N}} m_J \tilde{\mathbf{r}}_J, \quad \mathcal{M} = \sum_{J=1}^{\mathcal{N}} m_J, \quad (2.25)$$

and the relative coordinates (with respect to the \mathcal{N} -th particle)

$$\mathbf{r}_J = \tilde{\mathbf{r}}_J - \tilde{\mathbf{r}}_{\mathcal{N}}, \quad (J = 1, \dots, \mathcal{N} - 1), \quad (2.26)$$

we can use their associated momenta $\mathbf{P} = -i \frac{\partial}{\partial \mathbf{R}}$ and $\mathbf{p}_J = -i \frac{\partial}{\partial \mathbf{r}_J}$ ($J = 1, \dots, \mathcal{N} - 1$) to express the original momenta $\tilde{\mathbf{p}}_J = -i \frac{\partial}{\partial \tilde{\mathbf{r}}_J}$ ($J = 1, \dots, \mathcal{N}$) as

$$\tilde{\mathbf{p}}_J = \begin{cases} \frac{m_J}{\mathcal{M}} \mathbf{P} + \mathbf{p}_J, & (J = 1, \dots, \mathcal{N} - 1) \\ \frac{m_J}{\mathcal{M}} \mathbf{P} - \sum_{K=1}^{\mathcal{N}-1} \mathbf{p}_K, & (J = \mathcal{N}) \end{cases}. \quad (2.27)$$

In the reduced VG TDSE without the $|\mathbf{A}(t)|^2$ term, the time-dependent Hamiltonian is then expressed in terms of the new coordinates and momenta:

$$\begin{aligned} \tilde{H}(t) &= \frac{\mathbf{P}^2}{2\mathcal{M}} - \frac{Q\mathbf{A}(t) \cdot \mathbf{P}}{\mathcal{M}} \\ &+ \sum_{J=1}^{\mathcal{N}-1} \frac{\mathbf{p}_J^2}{2\mu_J} + \sum_{J=1}^{\mathcal{N}-1} \sum_{K \neq J}^{\mathcal{N}-1} \frac{\mathbf{p}_J \cdot \mathbf{p}_K}{2m_{\mathcal{N}}} - \sum_{J=1}^{\mathcal{N}-1} \left(\frac{q_J}{m_J} - \frac{q_{\mathcal{N}}}{m_{\mathcal{N}}} \right) \mathbf{A}(t) \cdot \mathbf{p}_J \\ &+ \sum_{J=1}^{\mathcal{N}-1} \sum_{K > J}^{\mathcal{N}-1} \frac{q_J q_K}{|\mathbf{r}_J - \mathbf{r}_K|} + \sum_{J=1}^{\mathcal{N}-1} \frac{q_J q_{\mathcal{N}}}{|\mathbf{r}_J|}, \end{aligned} \quad (2.28)$$

where $Q = \sum_{J=1}^{\mathcal{N}} q_J$ is the total charge of the system and μ_J is the reduced mass

$$\mu_J = \frac{m_J m_{\mathcal{N}}}{m_J + m_{\mathcal{N}}} = \frac{m_J}{1 + \frac{m_J}{m_{\mathcal{N}}}}, \quad (J = 1, \dots, \mathcal{N} - 1). \quad (2.29)$$

We can write the \mathcal{N} -particle state $|\tilde{\Psi}(t)\rangle$ is a product of the center-of-mass part $|\Psi_{\text{CM}}(t)\rangle$ and the remaining part $|\Psi(t)\rangle$:

$$|\tilde{\Psi}(t)\rangle = |\Psi_{\text{CM}}(t)\rangle \otimes |\Psi(t)\rangle. \quad (2.30)$$

The center-of-mass part has a trivial motion (a Volkov solution) satisfying the TDSE

$$i \frac{\partial}{\partial t} |\Psi_{\text{CM}}(t)\rangle = \left[\frac{\mathbf{P}^2}{2\mathcal{M}} - \frac{Q\mathbf{A}(t) \cdot \mathbf{P}}{\mathcal{M}} \right] |\Psi_{\text{CM}}(t)\rangle. \quad (2.31)$$

The TDSE for the the remaining part is then

$$i \frac{\partial}{\partial t} |\Psi(t)\rangle = H(t) |\Psi(t)\rangle, \quad (2.32)$$

with the corresponding Hamiltonian $H(t)$ given by

$$H(t) = \sum_{J=1}^{\mathcal{N}-1} \left[\sum_{K \neq J}^{\mathcal{N}-1} \frac{\mathbf{p}_J \cdot \mathbf{p}_K}{2m_{\mathcal{N}}} + \frac{\mathbf{p}_J^2}{2\mu_J} - \left(\frac{q_J}{m_J} - \frac{q_{\mathcal{N}}}{m_{\mathcal{N}}} \right) \mathbf{A}(t) \cdot \mathbf{p}_J \right] + \sum_{J=1}^{\mathcal{N}-1} \left[\sum_{K>J}^{\mathcal{N}-1} \frac{q_J q_K}{|\mathbf{r}_J - \mathbf{r}_K|} + \frac{q_J q_{\mathcal{N}}}{|\mathbf{r}_J|} \right]. \quad (2.33)$$

The terms containing $\mathbf{p}_J \cdot \mathbf{p}_K$ ($K \neq J$) are known as the mass-polarization terms, which only appear in many-body systems composed of three or more particles.

In the above derivation, we distinguish the \mathcal{N} -th particle from the other ($\mathcal{N} - 1$) particles. For atomic systems, it is natural to choose the nucleus as the \mathcal{N} -th particle and the electrons as the other ($\mathcal{N} - 1$) particles. Due to the fact that the nucleus has much larger mass than the electrons, i.e., $m_{\mathcal{N}} \gg m_J$ ($J = 1, \dots, \mathcal{N} - 1$), we can neglect the mass polarization terms and approximate the Hamiltonian $H(t)$ as

$$H(t) \approx \sum_{J=1}^{\mathcal{N}-1} \left[\frac{\mathbf{p}_J^2}{2m_J} - \frac{q_J}{m_J} \mathbf{A}(t) \cdot \mathbf{p}_J + \sum_{K>J}^{\mathcal{N}-1} \frac{q_J q_K}{|\mathbf{r}_J - \mathbf{r}_K|} + \frac{q_J q_{\mathcal{N}}}{|\mathbf{r}_J|} \right]. \quad (2.34)$$

For example, we consider a two-electron atomic system with the nuclear charge number \mathcal{Z} (e.g., $\mathcal{Z} = 1$ for hydrogen anion and $\mathcal{Z} = 2$ for helium atom). After the separation of the center-of-mass motion, in the reduced VG TDSE we approximately use

$$H(t) \approx \sum_{J=1}^2 \left[\frac{\mathbf{p}_J^2}{2} + \mathbf{A}(t) \cdot \mathbf{p}_J - \frac{\mathcal{Z}}{|\mathbf{r}_J|} \right] + \frac{1}{|\mathbf{r}_1 - \mathbf{r}_2|}, \quad (2.35)$$

to describe the time-dependent dynamics of the two-electron atomic system. Such a Hamiltonian implies that we work in a coordinate system with the nucleus fixed at the origin, which is referred to as the infinite-nuclear-mass approximation.

In this section the separation of the center-of-mass motion is derived from the reduced VG TDSE. As discussed in §2.2, the $|\mathbf{A}(t)|^2$ term does not contain any physical significance within the dipole approximation. Therefore it is feasible and straightforward to modify Eqs. (2.34) and (2.35) for other gauges by performing the corresponding gauge transformations.

2.4 Reduced-dimensional Models

In the strong-field regime where the laser interaction cannot be treated by the perturbation theory, one needs to solve the TDSE numerically. Full-dimensional TDSE simulations usually require huge computational resources, so they are only feasible for some small systems. For the simplest one-electron atom (or the SAE model), there have been many publications based on three-dimensional (3D) TDSE simulations (see, e.g., Refs. [101–105]). Also, a few 3D TDSE solvers and codes are already available [106–109]. If two electrons are assumed to be active in a multi-electron system, it is still possible, but rather difficult to solve the full-dimensional TDSE. Some researchers have performed full-dimensional TDSE simulations for two-active-electron atoms [76, 77, 89, 90, 110–128]. However, these calculations are usually performed on large-scale super-computers, and the considered laser parameters are quite limited. As for strong-field ionization by low-frequency laser pulses (in the NIR or MIR regime), the long wavelength can result in a large quiver radius of the electron, and many angular momentum states are involved in the dynamics. Therefore the corresponding full-dimensional TDSE simulations are very challenging [129]. So far the longest wavelength considered in the two-electron full-dimensional TDSE simulations is, to our knowledge, ~ 800 nm [122, 128]. The corresponding computational cost is also quite large. For example, more than 4000 cores were utilized for the calculations in Ref. [122]. The calculations in Ref. [128] were performed in a more efficient manner, and the authors used 128 cores running for more than 10 days for the simulations at the wavelength of ~ 800 nm.

Instead of solving the full-dimensional TDSE of real systems, the utilization of reduced-dimensional models offers a different avenue to investigate strong-field phenomena. In the late 1980s, a one-dimensional (1D) model for the SAE case was first introduced for studying the ATI [130, 131]. Soon afterwards the same model was used for studying other strong-field phenomena such as high-order harmonic generation [132, 133] and atomic stabilization [134, 135]. Also, some properties of the 1D model were investigated in Ref. [136]. Later the idea of using 1D models was extended to two-active-electron systems [137–140]. Since these early attempts, numerical experiments based on reduced-dimensional models have been widely applied in the strong-field regime (see, e.g., Refs. [78, 81, 88, 141–148] for applications of the 1D two-electron models).

Regarding reduced-dimensional models, there are some remarks that should be made. First, the use of reduced-dimensional models may result in a restriction of the laser polarization that can be considered. For example, only linearly-polarized laser interaction can be simulated within a 1D model, because the electron motion is intrinsically restricted to one dimension by the model. Second, the results obtained from reduced-dimensional models should not be quantitatively compared to those

obtained from experiments or full-dimensional calculations. Instead, we should analyze the simulation results within the model itself and conclude some qualitative tendencies. The conclusions could be reasonable for real systems, as long as the underlying physics does not significantly depend on the dimensionality. Third, the reduced-dimensional simulations allow us to investigate the strong-field phenomena in a wide range of laser parameters. As shown in one of our published papers [93], within the 1D two-electron model, we performed *ab initio* calculations for a long wavelength of 2400 nm. Last, another advantage of using reduced-dimensional models is that they can serve as a practical testbed for examining theoretical and numerical methods.

Numerical Methods for Solving the TDSE

3.1 Generic Concepts for Time-evolution

To solve the TDSE, one can make use of the time-evolution operator $U(t, t')$, which propagates the state at time t' to the state at time t as

$$|\Psi(t)\rangle = U(t, t') |\Psi(t')\rangle. \quad (3.1)$$

Normally $U(t, t')$ is a unitary operator due to the requirement of probability conservation, and it solves the TDSE

$$i \frac{\partial}{\partial t} U(t, t') = H(t) U(t, t'). \quad (3.2)$$

The formal expression for the time-evolution operator is

$$U(t, t') = \mathcal{T} \exp \left[-i \int_{t'}^t dt'' H(t'') \right], \quad (3.3)$$

where \mathcal{T} is the time-ordering operator.

Short-time Propagator

In numerical simulations, the time propagation is usually performed with a series of time steps. We can choose the time-step size Δt to be small enough such that the variation of the time-dependent Hamiltonian $H(t)$ over the interval $[t, t + \Delta t]$ is negligible. Thus a short-time propagator $U(t + \Delta t, t)$ can be used to evolve the state from time t to time $(t + \Delta t)$ as

$$U(t + \Delta t, t) \approx \exp [-i \Delta t H(t)]. \quad (3.4)$$

If the initial state of the system is known, the time propagation can be performed by applying a series of short-time propagators

$$U(t + s\Delta t, t) \approx U(t + s\Delta t, t + s\Delta t - \Delta t) \cdots U(t + 2\Delta t, t + \Delta t) U(t + \Delta t, t). \quad (3.5)$$

Note that the time propagators used in practice may not be unitary. For example, absorbing boundary conditions (absorbers) introduced in the TDSE simulations will make the Hamiltonian non-Hermitian, leading to non-unitary time propagators and loss of wave function norm. Details about two types of absorbers will be discussed in §3.4. Another useful application of non-unitary time propagators is the imaginary time propagation (ITP) method [149], which can be used to prepare the initial state for real time propagation.

Imaginary Time Propagation

The ITP method [149] offers a convenient way to obtain the field-free ground state, which can be chosen as the initial state for real time propagation. Suppose that the time-independent Hamiltonian H_0 has a series of eigen states $|\psi_n\rangle$ and eigen energies E_n , i.e.,

$$H_0 |\psi_n\rangle = E_n |\psi_n\rangle, \quad (3.6)$$

an arbitrary state of the system $|\mathcal{A}\rangle$ can be expressed as a linear combination of $|\psi_n\rangle$ as

$$|\mathcal{A}\rangle = \sum_n a_n |\psi_n\rangle. \quad (3.7)$$

By defining a pure imaginary time $\tau = it$, we introduce a non-unitary time propagator for the time-independent Hamiltonian H_0 :

$$U'(\tau + \Delta\tau, \tau) = \exp[-\Delta\tau H_0]. \quad (3.8)$$

Applying this time propagator onto $|\mathcal{A}\rangle$ gives a new state

$$|\mathcal{A}'\rangle = U'(\tau + \Delta\tau, \tau) |\mathcal{A}\rangle = \sum_n a'_n |\psi_n\rangle, \quad (3.9)$$

with

$$a'_n = a_n \exp[-\Delta\tau E_n]. \quad (3.10)$$

Thus the updated ground-state coefficient a'_g gets the largest positive multiplying factor $\exp[-\Delta\tau E_g]$ among all the coefficients. For any state with a non-zero ground-state coefficient a_g , if we repeat applying the non-unitary time propagator Eq. (3.8) and renormalize the updated state at each time step, then the ground-state portion will eventually increase to 1 while all the excited-state coefficients will decrease to 0, i.e., the ITP will converge to the ground state $|\psi_g\rangle$.

3.2 Discretization of Wave Function

To solve the TDSE numerically, the first step is discretization, i.e., representing the wave function by a finite set of numbers that can be manipulated by computers. Also, one has to describe how operators act on the discretized wave function.

In this section we will illustrate the discretization methods by considering the 1D one-electron TDSE

$$i \frac{\partial}{\partial t} \Psi(x, t) = H(x, t) \Psi(x, t). \quad (3.11)$$

with the Hamiltonian

$$H(x, t) = \begin{cases} \frac{1}{2} \left[-i \frac{\partial}{\partial x} + A(t) \right]^2 + V(x), & \text{VG} \\ -\frac{1}{2} \frac{\partial^2}{\partial x^2} - \frac{\partial}{\partial t} A(t)x + V(x), & \text{LG} \end{cases}. \quad (3.12)$$

The time-independent case can be obtained by setting the vector potential $A(t) = 0$.

One idea for discretization is to expand the wave function with a set of time-independent basis functions $\{f_n(x)\}_{n=1}^N$, i.e.,

$$\Psi(x, t) = \sum_{n=1}^N c_n(t) f_n(x), \quad (3.13)$$

where $\{c_n(t)\}_{n=1}^N$ are the corresponding time-dependent coefficients. This idea, which is referred to as the spectral method, has been widely used in quantum mechanics. Due to the finite number of basis functions, the basis set is not complete in principle. However, if we properly choose the basis set such that the wave function can be effectively represented by a linear combination of the basis functions, then the numerical simulations based on the discretized TDSE should be acceptable.

For simplicity, the considered basis functions are usually chosen to be real-valued, but they are not necessarily orthonormal^[i]. For this reason we introduce an overlap matrix \mathbf{S} with each element defined by

$$S_{mn} = \langle f_m | f_n \rangle = \int dx f_m(x) f_n(x). \quad (3.14)$$

Normally the inverse of the overlap matrix \mathbf{S}^{-1} exists, as long as the basis functions are properly chosen such that they are linearly independent. There is a discrete

^[i]Actually orthonormal basis functions are used in our practical calculations. However, here we still prefer to introduce a general discretization approach that also works for a non-orthonormal basis set. A typical example of non-orthonormal basis functions is the application of B-splines (see, e.g., Refs. [150, 151] for reviews).

completeness relation for the linear space spanned by the basis set,

$$\sum_{n=1}^N \sum_{m=1}^N |f_n\rangle S_{nm}^{-1} \langle f_m| = \mathbb{1}, \quad (3.15)$$

where S_{nm}^{-1} stands for a matrix element of \mathbf{S}^{-1} . Then the coefficients in Eq. (3.13) are given by

$$c_n(t) = \sum_{m=1}^N S_{nm}^{-1} \langle f_m | \Psi(t) \rangle. \quad (3.16)$$

By arranging the time-dependent coefficients into a column vector

$$\mathbf{c}(t) = [c_1(t), \dots, c_N(t)]^T, \quad (3.17)$$

and constructing the time-dependent Hamiltonian matrix $\mathbf{H}(t)$ with each element defined by

$$H_{mn}(t) = \langle f_m | H(t) | f_n \rangle = \int dx [f_m(x) H(x, t) f_n(x)], \quad (3.18)$$

we can write the discretized TDSE in a matrix form

$$i \frac{\partial}{\partial t} \mathbf{c}(t) = \mathbf{S}^{-1} \mathbf{H}(t) \mathbf{c}(t). \quad (3.19)$$

Note that the key procedure of discretization relies on Eq. (3.15). Here we briefly summarize two types of basic operations that should be “translated” into matrix language by discretization. The first type is applying an operator \mathcal{O} onto a known state to obtain a new state $|\Psi'\rangle = \mathcal{O} |\Psi\rangle$. With the old state $|\Psi\rangle$ represented by a coefficient vector \mathbf{c} as Eq. (3.17) and the operator \mathcal{O} represented by a matrix \mathbf{O} similar to Eq. (3.18), the coefficient vector of the new state is then

$$\mathbf{c}' = \mathbf{S}^{-1} \mathbf{O} \mathbf{c}. \quad (3.20)$$

The second type is evaluating a scalar of the form $\langle \Psi_j | \mathcal{O} | \Psi_k \rangle$. With the state $|\Psi_k\rangle$ ($|\Psi_j\rangle$) represented by the corresponding coefficient vector \mathbf{c}_k (\mathbf{c}_j) and the operator \mathcal{O} represented by a matrix \mathbf{O} , the scalar $\langle \Psi_j | \mathcal{O} | \Psi_k \rangle$ can be computed by matrix multiplication as

$$\langle \Psi_j | \mathcal{O} | \Psi_k \rangle = \mathbf{c}_j^\dagger \mathbf{O} \mathbf{c}_k. \quad (3.21)$$

If an orthonormal basis set is used, the overlap matrix becomes the identity matrix, i.e., $\mathbf{S}^{-1} = \mathbf{S} = \mathbf{1}$. Actually, it is possible and convenient to transform from a non-orthonormal to an orthonormal basis set by defining

$$\tilde{\mathbf{c}}(t) = \mathbf{S}^{+1/2} \mathbf{c}(t), \quad (3.22)$$

$$\tilde{\mathbf{H}}(t) = \mathbf{S}^{-1/2} \mathbf{H}(t) \mathbf{S}^{-1/2}, \quad (3.23)$$

thus the discretized TDSE can be written in a simpler form

$$i \frac{\partial}{\partial t} \tilde{\mathbf{c}}(t) = \tilde{\mathbf{H}}(t) \tilde{\mathbf{c}}(t). \quad (3.24)$$

To evaluate the matrix elements for the Hamiltonian given by Eq. (3.12), we need to calculate three types of integrals:

$$P_{mn} = -i \int dx \left[f_m(x) \frac{\partial}{\partial x} f_n(x) \right], \quad (3.25)$$

$$T_{mn} = -\frac{1}{2} \int dx \left[f_m(x) \frac{\partial^2}{\partial x^2} f_n(x) \right], \quad (3.26)$$

$$V_{mn} = \int dx \left[f_m(x) V(x) f_n(x) \right]. \quad (3.27)$$

Here P_{mn} defines the momentum operator matrix \mathbf{P} , T_{mn} defines the kinetic energy matrix \mathbf{T} , and V_{mn} defines the matrix \mathbf{V} for a scalar function $V(x)$. For example, if $V(x) = 1$, we evaluate the overlap matrix \mathbf{S} ; if $V(x) = x$, we evaluate the matrix \mathbf{X} for the coordinate operator. In practical simulations, we typically use basis functions $\{f_n(x)\}_{n=1}^N$ that satisfy

$$f_n(x) \Big|_{x \rightarrow \pm\infty} = 0, \quad \frac{\partial}{\partial x} f_n(x) \Big|_{x \rightarrow \pm\infty} = 0. \quad (3.28)$$

For such basis functions, we can evaluate the kinetic matrix elements by performing partial integration in Eq. (3.26), i.e.,

$$T_{mn} = \frac{1}{2} \int dx \left[\frac{\partial}{\partial x} f_m(x) \right] \left[\frac{\partial}{\partial x} f_n(x) \right]. \quad (3.29)$$

Discrete Variable Representation

Discrete variable representation (DVR) [152] essentially follows the idea of the spectral method. However, it looks like a grid method where the wave function is represented by discrete values on a set of selected grid points. The DVR basis functions are localized about discrete values of the variables, and Gaussian quadratures are employed for the evaluation of integrals. Due to the accuracy and efficiency of Gaussian quadratures, the DVR is a reliable and popular method for numerical computations.

A DVR basis set is intimately linked with a Gaussian quadrature rule. For example, an integral of a function $\mathcal{F}(x)$ weighted by a function $\mathcal{W}(x)$ over an interval $[u, v]$ can be approximated by a Gaussian quadrature

$$\int_u^v dx \mathcal{W}(x) \mathcal{F}(x) \approx \sum_{g=0}^{G-1} w_g^{[u,v]} \mathcal{F}(x_g^{[u,v]}), \quad (3.30)$$

with $\{x_g^{[u,v]}\}_{g=0}^{G-1}$ the quadrature points and $\{w_g^{[u,v]}\}_{g=0}^{G-1}$ the quadrature weights. It is exact for polynomials up to some degree, depending on the specific quadrature rule used. The key idea of a Gaussian quadrature is to maximize the degree of exactness by a good choice of the quadrature points and weights.

The Gaussian quadrature points, which can also be seen as interpolation points, make the DVR method grid-like. Once a set of interpolation points $\{x_g^{[u,v]}\}_{g=0}^{G-1}$ is selected, we can construct the corresponding Lagrange polynomials

$$\pi_g^{[u,v]}(x) = \prod_{g' \neq g}^{G-1} \frac{x - x_{g'}^{[u,v]}}{x_g^{[u,v]} - x_{g'}^{[u,v]}}, \quad (g = 0, \dots, G-1), \quad (3.31)$$

which satisfy $\pi_g^{[u,v]}(x_{g'}^{[u,v]}) = \delta_{g'g}$. We approximate the integral Eq. (3.30) by using the Lagrange interpolation of $\mathcal{F}(x)$,

$$\int_u^v dx \mathcal{W}(x) \mathcal{F}(x) \approx \int_u^v dx \mathcal{W}(x) \sum_{g=0}^{G-1} \mathcal{F}(x_g^{[u,v]}) \pi_g^{[u,v]}(x), \quad (3.32)$$

which provides an expression for the quadrature weights

$$w_g^{[u,v]} = \int_u^v dx \mathcal{W}(x) \pi_g^{[u,v]}(x), \quad (g = 0, \dots, G-1). \quad (3.33)$$

There are various types of Gaussian quadrature rules and the corresponding DVRs. Here we will illustrate some properties of the DVR method by taking the Gauss-Legendre DVR as an example^[iii], which corresponds to the simple form of the weight function $\mathcal{W}(x) = 1$. The Gauss-Legendre quadrature points and weights are constructed with the Legendre polynomials, which can be expressed by a three-term recurrence

$$(g+1)\mathcal{P}_{g+1}(x) = (2g+1)x\mathcal{P}_g(x) - g\mathcal{P}_{g-1}(x), \quad (3.34)$$

with the first two polynomials given by

$$\mathcal{P}_0(x) = 1, \quad \mathcal{P}_1(x) = x. \quad (3.35)$$

The Legendre polynomials are mutually orthogonal over $[-1, +1]$ with the weight function $\mathcal{W}(x) = 1$,

$$\int_{-1}^{+1} dx \mathcal{P}_{g'}(x) \mathcal{P}_g(x) = \delta_{g'g} \frac{2}{2g+1}. \quad (3.36)$$

^[iii]In fact the Gauss-Legendre DVR is not used in our work, however, it is a simple illustrative example. Also, it is beneficial to give a brief description of the Gauss-Legendre quadrature before introducing the Gauss-Legendre-Lobatto DVR used in our work (see the next subsection).

For the interval $[-1, +1]$, the Gauss-Legendre quadrature points $\{\hat{x}_g^{[-1,+1]}\}_{g=0}^{G-1}$ are the roots of $\mathcal{P}_G(x)$ and the corresponding weights $\{\hat{w}_g^{[-1,+1]}\}_{g=0}^{G-1}$ are given by

$$\hat{w}_g^{[-1,+1]} = \frac{2 \left[1 - \left(\hat{x}_g^{[-1,+1]} \right)^2 \right]}{\left[(G+1) \mathcal{P}_{G+1}(\hat{x}_g^{[-1,+1]}) \right]^2} = \frac{2 \left[1 - \left(\hat{x}_g^{[-1,+1]} \right)^2 \right]}{\left[G \mathcal{P}_{G-1}(\hat{x}_g^{[-1,+1]}) \right]^2}. \quad (3.37)$$

With these quadrature points and weights, the quadrature rule

$$\int_{-1}^{+1} dx \mathcal{F}(x) \approx \sum_{g=0}^{G-1} \hat{w}_g^{[-1,+1]} \mathcal{F}(\hat{x}_g^{[-1,+1]}), \quad (3.38)$$

is exact for polynomials of degree $(2G - 1)$ or less.

The quadrature rule over $[-1, +1]$ can be scaled to an arbitrary interval $[u, v]$ by a simple variable change

$$x \in [-1, +1] \mapsto \left(\frac{v-u}{2}x + \frac{u+v}{2} \right) \in [u, v], \quad (3.39)$$

Thus the quadrature points $\{\hat{x}_g^{[u,v]}\}_{g=0}^{G-1}$ and weights $\{\hat{w}_g^{[u,v]}\}_{g=0}^{G-1}$ for the interval $[u, v]$ are related to those for $[-1, +1]$ as

$$\hat{x}_g^{[u,v]} = \frac{v-u}{2} \hat{x}_g^{[-1,+1]} + \frac{u+v}{2}, \quad (3.40)$$

$$\hat{w}_g^{[u,v]} = \frac{v-u}{2} \hat{w}_g^{[-1,+1]}. \quad (3.41)$$

The Gauss-Legendre DVR basis functions can be constructed with the Lagrange polynomials $\{\hat{\pi}_g^{[u,v]}(x)\}_{g=0}^{G-1}$, which are of degree $(G - 1)$. Considering the inner product of two Lagrange polynomials

$$\int_u^v dx \hat{\pi}_{g'}^{[u,v]}(x) \hat{\pi}_g^{[u,v]}(x) = \sum_{g''=0}^{G-1} \hat{w}_{g''}^{[u,v]} \hat{\pi}_{g'}^{[u,v]}(\hat{x}_{g''}^{[u,v]}) \hat{\pi}_g^{[u,v]}(\hat{x}_{g''}^{[u,v]}) = \delta_{g'g} \hat{w}_g^{[u,v]}, \quad (3.42)$$

we define a set of orthonormal DVR basis functions

$$\hat{f}_g^{\circ}(x) = \frac{\hat{\pi}_g^{[u,v]}(x)}{\sqrt{\hat{w}_g^{[u,v]}}, \quad (g = 0, \dots, G - 1). \quad (3.43)$$

For a scalar function $V(x)$, we apply the quadrature rule to evaluate the corresponding matrix element

$$\begin{aligned} V_{g'g} &= \langle f_{g'}^\circ(x) | V(x) | f_g^\circ(x) \rangle \approx \sum_{g''=0}^{G-1} \dot{w}_{g''}^{[u,v]} \frac{\pi_{g'}^\circ(x_{g''}^{[u,v]})}{\sqrt{\dot{w}_{g'}^{[u,v]}}} V(x_{g''}^{[u,v]}) \frac{\pi_g^\circ(x_{g''}^{[u,v]})}{\sqrt{\dot{w}_g^{[u,v]}}} \\ &= \delta_{g'g} V(x_g^{[u,v]}). \end{aligned} \quad (3.44)$$

Thus the DVR basis set gives a diagonal matrix \mathbf{V} within the quadrature accuracy, which is an important feature and advantage of the DVR method. The matrices for the momentum operator and the kinetic energy operator can be accurately evaluated by applying the quadrature rule and the derivative of the Lagrange polynomials

$$\frac{\partial}{\partial x} \pi_g^\circ(x) = \pi_g^{[u,v]}(x) \sum_{g' \neq g}^{G-1} \frac{1}{x - x_{g'}^{[u,v]}}, \quad (g = 0, \dots, G-1). \quad (3.45)$$

Typically the DVR basis set leads to full matrices \mathbf{P} and \mathbf{T} that are defined as Eqs. (3.25) and (3.26).

Finite-Element Discrete Variable Representation

In pursuit of more efficient numerical computations, we prefer to use finite-element discrete variable representation (FEDVR) for discretization. In the FEDVR method [153–155], the whole coordinate space is divided into a number of subdomains called finite elements, and the discretized wave function and operators are described by the local DVR functions in each element. As in the DVR method, the matrix for a scalar function $V(x)$ is diagonal within quadrature accuracy. In addition, the FEDVR method leads to sparse matrices for the momentum operator and the kinetic energy operator. Due to this sparsity, a matrix-vector product can be computed efficiently in the FEDVR method.

In the FEDVR method, the grid is composed of many local subgrids for each element. For example, if we divide the coordinate space $[u, v]$ into M elements, in each element ξ ($\xi = 1, \dots, M$), we need to set up a subgrid of Gaussian quadrature points $\{x_g^\xi\}$ and weights $\{w_g^\xi\}$ ($g = 0, \dots, G_\xi$), with the number of quadrature points in element ξ denoted by G_ξ . To impose continuity for the represented wave function, we use the Gauss-Legendre-Lobatto quadrature for each element, where the first and last quadrature points are situated at the boundary of each element, i.e.,

$$x_0^1 = u, \quad x_{G_M-1}^M = v, \quad x_{G_\xi-1}^\xi = x_0^{\xi+1} \quad (\xi = 1, \dots, M-1). \quad (3.46)$$

The Gauss-Legendre-Lobatto quadrature over the interval $[-1, +1]$ is also constructed with the Legendre polynomials. It uses quadrature points $x_0^{[-1,+1]} = -1$

and $x_{G-1}^{[-1,+1]} = +1$, together with inner points $\left\{ x_g^{[-1,+1]} \right\}_{g=1}^{G-2}$ defined by the roots of $\left[\frac{\partial}{\partial x} \mathcal{P}_{G-1}(x) \right]$. All the quadrature weights $\left\{ w_g^{[-1,+1]} \right\}_{g=0}^{G-1}$ can be written as a unified expression

$$w_g^{[-1,+1]} = \frac{2}{G(G-1) \left[\mathcal{P}_{G-1}(x_g^{[-1,+1]}) \right]^2}. \quad (3.47)$$

The Gauss-Legendre-Lobatto quadrature is exact for polynomials of degree $(2G-3)$ or less. Similar to the Gauss-Legendre quadrature, the Gauss-Legendre-Lobatto quadrature rule over an arbitrary interval $[u, v]$ can be easily obtained by a linear variable change [see Eqs. (3.39)-(3.41)].

For constructing of the FEDVR basis functions, we introduce the corresponding Lagrange polynomials $\left\{ \pi_g^\xi(x) \right\}_{g=0}^{G_\xi-1}$ that are locally defined in each element as

$$\pi_g^\xi(x) = \begin{cases} \prod_{g' \neq g}^{G_\xi-1} \frac{x - x_{g'}^\xi}{x_g^\xi - x_{g'}^\xi}, & (x_0^\xi \leq x \leq x_{G_\xi-1}^\xi) \\ 0, & \text{else} \end{cases}. \quad (3.48)$$

Note that any integral over the whole interval $[u, v]$ can be written as a sum of integrals over each element and then calculated by applying the quadrature for each element. Therefore the inner product of two locally-defined Lagrange polynomials is

$$\int_u^v dx \pi_{g'}^\xi(x) \pi_g^\xi(x) \approx \delta_{\xi' \xi} \delta_{g' g} w_g^\xi. \quad (3.49)$$

At the boundary points of each element ($x_{G_\xi-1}^\xi = x_0^{\xi+1}$), we define bridge basis functions

$$f_{G_\xi-1}^\xi(x) = \frac{\pi_{G_\xi-1}^\xi(x) \cup \pi_0^{\xi+1}(x)}{\sqrt{w_{G_\xi-1}^\xi + w_0^{\xi+1}}}, \quad (3.50)$$

which connect the elements ξ and $(\xi + 1)$. Corresponding to the inner quadrature points of each element, we define inner basis functions that are localized in the element:

$$f_g^\xi(x) = \frac{\pi_g^\xi(x)}{\sqrt{w_g^\xi}}, \quad (g = 1, \dots, G_\xi - 2). \quad (3.51)$$

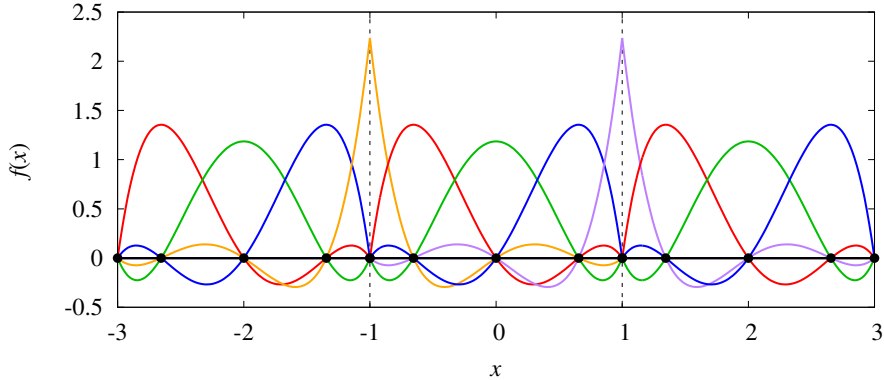


Figure 3.1: Three equally-sized finite elements and the corresponding FEDVR basis functions. The inner basis functions [Eq. (3.51)] are plotted with red, green and blue lines while two bridge functions [Eq. (3.50)] are plotted with orange and purple lines. The black solid dots indicate the Gauss-Legendre-Lobatto quadrature points.

All the inner basis functions and all the bridge functions compose the FEDVR basis set over the whole region $[u, v]$. In numerical simulations we usually assume a zero boundary condition for the 1D wave function, in which the basis functions corresponding to the boundary points u and v are simply dropped from the basis set. This means that the total number of the FEDVR basis functions is $N = \sum_{\xi=1}^M (G_{\xi} - 1) - 1$.

As an example, we show a small region $[-3, +3]$ discretized by 3 connected finite elements and the corresponding FEDVR basis functions in Figure 3.1. In this example, there are 5 Gauss-Legendre-Lobatto quadrature points in each element. With the functions corresponding to the boundary points ($x = \pm 3$) dropped from the basis set, there are 11 basis functions in total.

We note that in contrast to the DVR method, the FEDVR basis functions are approximately orthonormal, because the product of two Lagrange polynomials in each element is of degree $(2G_{\xi} - 2)$, for which the Gauss-Legendre-Lobatto quadrature is not exact. However, this deficiency of the FEDVR method has little effect in practice^[iii]. With an enough number of basis functions, the quadrature gives a good approximation to the integrals, and the FEDVR method performs well with acceptable numerical accuracy. Since the FEDVR basis functions are constructed from the locally-defined Lagrange polynomials Eq. (3.48), the matrices for the momentum operator and the kinetic energy operator are sparse in the FEDVR method.

^[iii]It can be seen as a feature of the DVR method, i.e., we treat the overlap matrix \mathbf{S} in the same way as a potential matrix \mathbf{V} [Eq. (3.27)].

3.3 Krylov-subspace Time Propagator

After discretizing the TDSE into a matrix form Eq. (3.19) [or Eq. (3.24), if an orthonormal basis set is preferred], we need to compute the time-evolution of the state by using the short-time propagator of the matrix form

$$\mathbf{c}(t + \Delta t) \approx \exp[-i\Delta t \mathbf{S}^{-1} \mathbf{H}(t)] \mathbf{c}(t). \quad (3.52)$$

With the total number of basis functions denoted by N , the discretized Hamiltonian $\mathbf{H}(t)$ is a $N \times N$ matrix. Exact evaluation of matrix exponential can be performed by finding a similarity transformation to diagonalize the exponent matrix,

$$\mathbf{\Xi}^{-1} [\mathbf{S}^{-1} \mathbf{H}(t)] \mathbf{\Xi} = \mathbf{\Upsilon}. \quad (3.53)$$

With the eigen-value diagonal matrix $\mathbf{\Upsilon}$ and the eigen-vector matrix $\mathbf{\Xi}$ solved, we can compute the short-time propagator

$$\exp[-i\Delta t \mathbf{S}^{-1} \mathbf{H}(t)] = \mathbf{\Xi} \exp[-i\Delta t \mathbf{\Upsilon}] \mathbf{\Xi}^{-1}. \quad (3.54)$$

However, the computational complexity of this approach typically scales as $O(N^3)$, which is only feasible for a small number of basis functions. Aiming at an efficient scheme to propagate the state, we introduce the Arnoldi-Lanczos propagator, which is also known as the Krylov-subspace propagator [156–159].

For a clear description of the Krylov-subspace propagator, we first apply the short-time propagator Eq. (3.4) on the state $|\Psi(t)\rangle$ and approximate the result as a truncation of the expansion, i.e.,

$$\begin{aligned} |\Psi(t + \Delta t)\rangle &= \exp[-i\Delta t H(t)] |\Psi(t)\rangle = \sum_{k=1}^{\infty} \frac{[-i\Delta t H(t)]^{k-1}}{(k-1)!} |\Psi(t)\rangle \\ &\approx \sum_{k=1}^L \frac{(-i\Delta t)^{k-1}}{(k-1)!} [H(t)]^{k-1} |\Psi(t)\rangle. \end{aligned} \quad (3.55)$$

This means that we approximately express the state $|\Psi(t + \Delta t)\rangle$ with a set of state vectors $[H(t)]^{k-1} |\Psi(t)\rangle$, ($k = 1, \dots, L$). The subspace spanned by these vectors is called the Krylov subspace^[iv]. In the Krylov subspace we can construct a set of orthonormal basis vectors $\{|\mathbf{q}_k(t)\rangle\}_{k=1}^L$, and then rewrite Eq. (3.55) as

$$\begin{aligned} |\Psi(t + \Delta t)\rangle &\approx \sum_{k=1}^L \sum_{j=1}^L |\mathbf{q}_k(t)\rangle \langle \mathbf{q}_k(t) | \exp[-i\Delta t H(t)] |\mathbf{q}_j(t)\rangle \langle \mathbf{q}_j(t) | \Psi(t)\rangle \\ &= \sum_{k=1}^L |\mathbf{q}_k(t)\rangle b_k(t), \end{aligned} \quad (3.56)$$

^[iv]In practice the Krylov subspace is constructed at each time step, so we keep the explicit time-dependence in the following formulation.

with the coefficient corresponding to $|\mathbf{q}_k(t)\rangle$ given by

$$b_k(t) = \sum_{j=1}^L \langle \mathbf{q}_k(t) | \exp[-i\Delta t H(t)] | \mathbf{q}_j(t) \rangle \langle \mathbf{q}_j(t) | \Psi(t) \rangle, \quad (k = 1, \dots, L). \quad (3.57)$$

According to the Arnoldi-Lanczos approach, the first Krylov vector $|\mathbf{q}_1(t)\rangle$ is obtained from $|\Psi(t)\rangle$ as

$$|\mathbf{q}_1(t)\rangle = \frac{|\Psi(t)\rangle}{\sqrt{\langle \Psi(t) | \Psi(t) \rangle}}, \quad (3.58)$$

which implies $\langle \mathbf{q}_j(t) | \Psi(t) \rangle = \delta_{j1} \sqrt{\langle \Psi(t) | \Psi(t) \rangle}$. By constructing the Krylov Hamiltonian matrix $\mathbf{h}(t)$ with each element given by

$$h_{jk}(t) = \langle \mathbf{q}_j(t) | H(t) | \mathbf{q}_k(t) \rangle, \quad (3.59)$$

we can see that the coefficient b_k in Eq. (3.57) is simply an element of the matrix exponential $\exp[-i\Delta t \mathbf{h}(t)]$, multiplied by $\sqrt{\langle \Psi(t) | \Psi(t) \rangle}$, i.e.,

$$b_k(t) = \sqrt{\langle \Psi(t) | \Psi(t) \rangle} \exp[-i\Delta t \mathbf{h}(t)]_{k1}, \quad (k = 1, \dots, L). \quad (3.60)$$

For a small L , the exponential of the $L \times L$ matrix $\mathbf{h}(t)$ can be easily evaluated according to the diagonalization approach shown in Eqs. (3.53) and (3.54).

Starting from $|\mathbf{q}_1(t)\rangle$ given by Eq. (3.58), we construct the Krylov basis vectors $\{|\mathbf{q}_k(t)\rangle\}_{k=1}^L$ and the matrix $\mathbf{h}(t)$ with a modified Gram-Schmidt orthogonalization, i.e., the Arnoldi iteration (see below).

Algorithm Pseudocode for the Arnoldi iteration

```

for  $k = 1, \dots, L$  do
   $|\mathbf{p}_1(t)\rangle = H(t) |\mathbf{q}_k(t)\rangle$ 
  for  $j = 1, \dots, k$  do
     $h_{jk}(t) = \langle \mathbf{q}_j(t) | \mathbf{p}_1(t) \rangle$ 
     $|\mathbf{p}_{j+1}(t)\rangle = |\mathbf{p}_1(t)\rangle - |\mathbf{q}_j(t)\rangle h_{jk}(t)$ 
  end for
   $h_{k+1,k}(t) = \sqrt{\langle \mathbf{p}_{k+1}(t) | \mathbf{p}_{k+1}(t) \rangle}$ 
   $|\mathbf{q}_{k+1}(t)\rangle = |\mathbf{p}_{k+1}(t)\rangle / h_{k+1,k}(t)$ 
end for

```

The matrix element $h_{jk} = 0$ for $(j > k + 1)$, i.e., the Krylov Hamiltonian $\mathbf{h}(t)$ obtained by the Arnoldi iteration is an upper Hessenberg matrix. For a Hermitian Hamiltonian $H(t)$, the Krylov Hamiltonian $\mathbf{h}(t)$ will become a tridiagonal matrix, and then the Arnoldi iteration can be replaced by a simpler algorithm called the

Lanczos recursion. Due to some absorbing boundary conditions introduced in the TDSE simulations, we usually have a non-Hermitian Hamiltonian $H(t)$ in practice. Therefore we always use the Arnoldi scheme for the time propagation.

For a fixed small time-step size Δt , the dimension of the Krylov subspace can be adaptively controlled. For convenience, we collect the coefficient $\{b_k(t)\}_{k=1}^L$ into a column vector

$$\mathbf{b}_L(t) = [b_1(t), \dots, b_L(t)]^T. \quad (3.61)$$

If the L -dimensional Krylov-subspace propagator already leads to converged time-evolution, increasing the Krylov dimension from L to $(L + 1)$ will only result in a negligible change in the coefficients of the Krylov vectors

$$\Delta \mathbf{b}_{L+1}(t) = \mathbf{b}_{L+1}(t) - [\mathbf{b}_L^T(t), 0]^T. \quad (3.62)$$

Therefore in each time step $t \rightarrow (t + \Delta t)$, we implement an adaptive control of the Krylov dimension by checking the ℓ^2 -norm $\|\Delta \mathbf{b}_{L+1}(t)\|$ against the error tolerance.

Note that the above Arnoldi-Lanczos approach can be easily “translated” into matrix language according to Eqs. (3.20) and (3.21). With the coefficient vectors of $\{|\mathbf{q}_k(t)\rangle\}_{k=1}^L$ arranged into a $N \times L$ matrix $\mathbf{Q}(t)$, the Krylov-subspace propagator produces the state at time $(t + \Delta t)$ represented in a matrix form

$$\mathbf{c}(t + \Delta t) \approx \mathbf{Q}(t)\mathbf{b}_L(t), \quad (3.63)$$

with $\mathbf{b}_L(t)$ defined in Eq. (3.61).

The Krylov-subspace propagator only requires simple computational manipulations such as matrix-vector products, vector-vector inner products and diagonalization of small matrices. So it can be generally applied to any many-body TDSE. Typically the computational complexity of the Krylov-subspace method scales as $O(N^2)$. In addition, combined with the FEDVR basis set, the sparsity of the Hamiltonian matrix $\mathbf{H}(t)$ will enable us to further improve the efficiency of the Krylov-subspace method.

3.4 Absorbing Boundary Conditions

In the numerical treatment of the TDSE, the wave function is usually discretized in a finite simulation box. If the simulation box is smaller than the range of the wave packet motion, there exists unphysical reflection at the boundaries, which will disturb the dynamics and lead to incorrect results. To avoid unphysical reflection at the boundaries, one can absorb the outgoing parts of the wave function when using a relatively smaller simulation volume. In principle, such an absorber should not modify the wave function in the inner region, where the observables are calculated.

Complex Absorbing Potential

One technique for absorbing the outgoing parts of the wave function is adding a complex absorbing potential (CAP) [160, 161] to the time-dependent Hamiltonian

$$H(t) \rightarrow H(t) + V_{\text{CAP}}, \quad (3.64)$$

where V_{CAP} is usually defined as a pure imaginary function that can damp the wave function smoothly in the absorbing regions.

The effect of the CAP can be understood by taking a view of the short-time propagator approximately,

$$U(t + \Delta t, t) \approx \exp\left(-i\frac{\Delta t}{2}V_{\text{CAP}}\right) \exp[-i\Delta t H(t)] \exp\left(-i\frac{\Delta t}{2}V_{\text{CAP}}\right). \quad (3.65)$$

In view of the fact that V_{CAP} and $H(t)$ do not commute, a split-operator scheme is used for better accuracy, which leads to error terms of order $O(\Delta t^3)$. We see from Eq. (3.65) that a properly chosen imaginary function V_{CAP} will result in smooth damping of the wave function in the absorbing regions.

There are various types of the CAP functions. As an illustrative example, for the 1D one-electron TDSE [Eq. (3.11)] we choose a CAP function of the form

$$V_{\text{CAP}}(x) = \begin{cases} 0, & |x| < r_c \\ -i \left\{ 1 - \cos \left[\frac{\pi(|x| - r_c)}{2(r_{\text{max}} - r_c)} \right] \right\}, & r_c \leq |x| \leq r_{\text{max}} \end{cases}. \quad (3.66)$$

This CAP has absorbing regions $r_c \leq |x| \leq r_{\text{max}}$, which should properly defined for good performance according to the laser parameters. For example, the CAP radius r_c should be larger than the electron quiver radius α_0 such that the quiver motion of the wave packet is not affected by the CAP. In two of our published papers [91, 92], where the considered laser interactions are in the short-wavelength (XUV) regime, the CAP of the form Eq. (3.66) is employed. It was also used in Refs. [162–167] by other researchers.

The CAP method is easy to implement, and it is applicable for both velocity and length gauges. However, it is not a perfect absorber. Although good performance can be achieved by tuning the CAP parameters, the CAP will inevitably cause some distortion of the wave function in the inner region. For the VG TDSE, there is another absorbing technique called exterior complex scaling (ECS), which rotates the coordinate into the complex plane in the outer region [168–171]. In principle, the ECS method allows absorbing the outgoing wave packet without distorting the inner-region wave function. In the next subsection, we will briefly introduce the ECS technique and its implementation in the framework of the FEDVR method [153, 170].

Exterior Complex Scaling

Similar to the CAP radius, a scaling radius r_c is defined in the ECS method to divide the coordinates into inner and outer regions. In the 1D case, the ECS method introduces a complex contour [169, 171]

$$z = \begin{cases} -r_c + (x + r_c) \exp(i\eta), & x < -r_c \\ x, & |x| \leq r_c \\ +r_c + (x - r_c) \exp(i\eta), & x > +r_c \end{cases}. \quad (3.67)$$

with a small scaling angle η that typically ranges from 0 to $\pi/4$. Correspondingly, all the operators should be transformed by a replacement $x \rightarrow z$. For example, the kinetic energy operator in the ECS method becomes

$$-\frac{1}{2} \frac{\partial^2}{\partial z^2} = \begin{cases} -\frac{1}{2} \frac{\partial^2}{\partial x^2}, & |x| < r_c \\ -\frac{\exp[-2i\eta]}{2} \frac{\partial^2}{\partial x^2}, & |x| > r_c \end{cases}. \quad (3.68)$$

We first take a look at the effect of the ECS transformation. An outgoing wave in the $\pm x$ direction is exponentially damped in the corresponding outer region as $x \rightarrow \pm\infty$,

$$\begin{aligned} \exp(+ikx) &\rightarrow \exp(+ikz) = \exp\{+ik[+r_c + (x - r_c) \cos(\eta)]\} \\ &\quad \times \exp[-k(x - r_c) \sin(\eta)], \quad (x > +r_c) \end{aligned} \quad (3.69)$$

$$\begin{aligned} \exp(-ikx) &\rightarrow \exp(-ikz) = \exp\{-ik[-r_c + (x + r_c) \cos(\eta)]\} \\ &\quad \times \exp[+k(x + r_c) \sin(\eta)], \quad (x < -r_c) \end{aligned} \quad (3.70)$$

with $k > 0$. In contrast, an incoming wave with $k < 0$ grows exponentially as $x \rightarrow \pm\infty$. Thus in the ECS method the outgoing and incoming waves have completely different asymptotic behavior and can be distinguished from each other by their norms. For a typical discretization with only square-integrable basis functions used, the incoming waves are completely excluded by complex scaling. This may explain why the ECS method works for the VG TDSE but fails for the LG TDSE. The 1D Volkov wave function $\chi_k(x, t)$ has different forms in velocity and length gauges,

$$\chi_k(x, t) = \begin{cases} (2\pi)^{-1/2} \exp[-iS_k(t)] \exp(ikx), & \text{VG} \\ (2\pi)^{-1/2} \exp[-iS_k(t)] \exp\{i[k + A(t)]x\}, & \text{LG} \end{cases} \quad (3.71)$$

where $S_k(t)$ is a time-dependent phase given by

$$S_k(t) = \int_{-\infty}^t dt' \frac{[k + A(t')]^2}{2}. \quad (3.72)$$

With complex scaling, the asymptotic behavior of the VG Volkov wave function is always of the same form as Eqs. (3.69) and (3.70), while the asymptotic behavior of the LG Volkov wave function is time-dependent due to the vector potential $A(t)$ involved. Therefore the distinction between the outgoing and incoming waves by their norms, which is the key feature of the ECS method, is only feasible for the VG TDSE [172].

With the FEDVR basis set, the ECS method can be conveniently implemented by choosing $\pm r_c$ as finite-element boundary points [170]. We suppose that $(+r_c)$ is the connecting point of elements ζ_{\oplus} and $(\zeta_{\oplus} + 1)$ while $(-r_c)$ is the connecting point of elements ζ_{\ominus} and $(\zeta_{\ominus} + 1)$, i.e.,

$$+r_c = x_{G_{\zeta_{\oplus}}-1}^{\zeta_{\oplus}} = x_0^{\zeta_{\oplus}+1}, \quad -r_c = x_{G_{\zeta_{\ominus}}-1}^{\zeta_{\ominus}} = x_0^{\zeta_{\ominus}+1}. \quad (3.73)$$

We can still use the locally-defined Lagrange polynomials [Eq. (3.48)] to construct the basis functions for the ECS method. Note that the inner product of two real-valued functions should be calculated as an integral along the complex contour, i.e.,

$$\begin{aligned} \langle f_m | f_n \rangle_{\eta} &= \int_{-r_{\max}}^{+r_{\max}} dz f_m(x) f_n(x) \\ &= \left[\int_{-r_{\max}}^{-r_c} dx f_m(x) f_n(x) + \int_{+r_c}^{+r_{\max}} dx f_m(x) f_n(x) \right] \exp(i\eta) \\ &\quad + \int_{-r_c}^{+r_c} dx f_m(x) f_n(x). \end{aligned} \quad (3.74)$$

Here the integral is divided into inner and outer regions, and in each region we can apply Gaussian quadrature rules for integrating the real-valued functions. This is the general procedure for constructing the basis set and the corresponding Hamiltonian matrix.

It is convenient to construct an orthonormal basis set with respect to the inner product defined in Eq. (3.74). For the FEDVR quadrature points in the inner region $(-r_c < x_g^{\xi} < +r_c)$, we define the ‘‘unscaled’’ basis functions according to Eqs. (3.50) and (3.51)

$$f_g^{\xi}(x) = \begin{cases} \frac{\pi_g^{\xi}(x)}{\sqrt{w_g^{\xi}}}, & (g = 1, \dots, G_{\xi} - 2) \\ \frac{\pi_{G_{\xi}-1}^{\xi}(x) \cup \pi_0^{\xi+1}(x)}{\sqrt{w_{G_{\xi}-1}^{\xi} + w_0^{\xi+1}}}, & (g = G_{\xi} - 1) \end{cases}, \quad (|x_g^{\xi}| < r_c) \quad (3.75)$$

For the FEDVR quadrature points in the outer region ($x_g^\xi < -r_c$) or ($x_g^\xi > +r_c$), we define the “scaled” basis functions

$$f_g^\xi(x) = \begin{cases} \frac{\pi_g^\xi(x)}{\sqrt{w_g^\xi \exp(i\eta)}}, & (g = 1, \dots, G_\xi - 2) \\ \frac{\pi_{G_\xi-1}^\xi(x) \cup \pi_0^{\xi+1}(x)}{\sqrt{(w_{G_\xi-1}^\xi + w_0^{\xi+1}) \exp(i\eta)}}, & (g = G_\xi - 1) \end{cases}, \quad (|x_g^\xi| > r_c) \quad (3.76)$$

The basis functions corresponding to $\pm r_c$ need a special treatment, i.e., we define the “half-scaled” bridge functions

$$f_{G_{\zeta_\oplus}-1}^{\zeta_\oplus}(x) = \frac{\pi_{G_{\zeta_\oplus}-1}^{\zeta_\oplus}(x) \cup \pi_0^{\zeta_\oplus+1}(x)}{\sqrt{w_{G_{\zeta_\oplus}-1}^{\zeta_\oplus} + w_0^{\zeta_\oplus+1} \exp(i\eta)}}, \quad (x_{G_{\zeta_\oplus}-1}^{\zeta_\oplus} = x_0^{\zeta_\oplus+1} = +r_c), \quad (3.77)$$

$$f_{G_{\zeta_\ominus}-1}^{\zeta_\ominus}(x) = \frac{\pi_{G_{\zeta_\ominus}-1}^{\zeta_\ominus}(x) \cup \pi_0^{\zeta_\ominus+1}(x)}{\sqrt{w_{G_{\zeta_\ominus}-1}^{\zeta_\ominus} \exp(i\eta) + w_0^{\zeta_\ominus+1}}}, \quad (x_{G_{\zeta_\ominus}-1}^{\zeta_\ominus} = x_0^{\zeta_\ominus+1} = -r_c). \quad (3.78)$$

By applying Eq. (3.74) and the Gauss-Legendre-Lobatto quadrature in each finite element, we can easily verify that Eqs. (3.75)-(3.78) compose the orthonormal basis set within the ECS scheme^[v]. Correspondingly, the matrix elements of the operators can be evaluated as an integral along the complex contour, following the same idea as in Eq. (3.74). In the limit of $\eta = 0$, the normal FEDVR discretization without the ECS technique is recovered.

Infinite-range Exterior Complex Scaling

There is an efficient implementation of the ECS method called the infinite-range exterior complex scaling (irECS), which was proposed by Armin Scrinzi [172]. The key idea is to extend the outer region to infinity, i.e.,

$$[+r_c, +r_{\max}] \rightarrow [+r_c, +\infty), \quad [-r_{\max}, -r_c] \rightarrow (-\infty, -r_c]. \quad (3.79)$$

^[v]In the evaluation of the inner product [Eq. (3.74)] according to this scheme, the complex-valued basis functions [Eqs. (3.76)-(3.78)] should not be complex conjugated when appearing as a bra-vector.

Since the ECS method results in exponentially-damping outgoing waves in the outer region [see Eqs. (3.69) and (3.70)], it will be efficient to choose basis functions of the same form for the infinite-range outer region $[+r_c, +\infty)$ or $(-\infty, -r_c]$.

To develop the corresponding DVR method for such semi-infinite domains, we first review the Gauss-Laguerre quadrature for the interval $[0, +\infty)^{[vi]}$,

$$\int_0^{+\infty} dx \exp(-x) \mathcal{F}(x) \approx \sum_{g=0}^{G-1} \dot{w}_g^{[0,+\infty)} \mathcal{F}(\dot{x}_g^{[0,+\infty)}). \quad (3.80)$$

The Gauss-Laguerre quadrature points and weights are constructed on the basis of the Laguerre polynomials, which can be expressed by a three-term recurrence

$$(g+1)\mathcal{L}_{g+1}(x) = (2g+1-x)\mathcal{L}_g(x) - g\mathcal{L}_{g-1}(x), \quad (3.81)$$

with the first two polynomials given by

$$\mathcal{L}_0(x) = 1, \quad \mathcal{L}_1(x) = 1 - x. \quad (3.82)$$

The Laguerre polynomials are mutually orthonormal over $[0, +\infty)$ with the weight function $\mathcal{W}(x) = \exp(-x)$, i.e.,

$$\int_0^{+\infty} dx \exp(-x) \mathcal{L}_{g'}(x) \mathcal{L}_g(x) = \delta_{g'g}. \quad (3.83)$$

The Gauss-Laguerre quadrature points $\left\{ \dot{x}_g^{[0,+\infty)} \right\}_{g=0}^{G-1}$ are the roots of $\mathcal{L}_G(x)$ and the corresponding quadrature weights $\left\{ \dot{w}_g^{[0,+\infty)} \right\}_{g=0}^{G-1}$ are given by

$$\dot{w}_g^{[0,+\infty)} = \frac{\dot{x}_g^{[0,+\infty)}}{\left[(G+1)\mathcal{L}_{G+1}(\dot{x}_g^{[0,+\infty)}) \right]^2} = \frac{\dot{x}_g^{[0,+\infty)}}{\left[G\mathcal{L}_{G-1}(\dot{x}_g^{[0,+\infty)}) \right]^2}. \quad (3.84)$$

Note that the Gauss-Laguerre quadrature does not include 0 as a quadrature point. Alternatively, we can choose the first quadrature point $x_0 = 0$ according to the Gauss-Laguerre-Radau quadrature. The Gauss-Laguerre-Radau quadrature points $\left\{ x_g^{[0,+\infty)} \right\}_{g=0}^{G-1}$ are roots of $\left[x \frac{\partial}{\partial x} \mathcal{L}_G(x) \right]$, and the corresponding quadrature weights $\left\{ w_g^{[0,+\infty)} \right\}_{g=0}^{G-1}$ are given by

$$w_g^{[0,+\infty)} = \frac{1}{G \left[\mathcal{L}_{G-1}(x_g^{[0,+\infty)}) \right]^2}. \quad (3.85)$$

^[vi]Our implementation of the irECS method relies on the Gauss-Laguerre-Radau quadrature only. Nevertheless, here we prefer to give a systematic introduction to both the Gauss-Laguerre and Gauss-Laguerre-Radau quadrature rules. A ring (°) is added above the notations for the unused quadrature.

The Gauss-Laguerre and Gauss-Laguerre-Radau quadrature rules are exact for polynomials of maximum degree $(2G - 1)$ and $(2G - 2)$, respectively.

The Laguerre polynomials of degree higher than 0 diverge as $x \rightarrow +\infty$. In practice, it is more convenient to work with bound functions. So the Lagrange functions $\tilde{\mathcal{L}}_g(x)$ ($g = 0, 1, \dots$) are introduced as

$$\tilde{\mathcal{L}}_g(x) = \exp\left(-\frac{x}{2}\right) \mathcal{L}_g(x), \quad (3.86)$$

and the modified quadrature weights are defined as $\tilde{w}_g^{[0,+\infty)} = \exp\left[x_g^{[0,+\infty)}\right] w_g^{[0,+\infty)}$, which can be obtained by replacing the Laguerre polynomial \mathcal{L}_{G-1} by the Laguerre function $\tilde{\mathcal{L}}_{G-1}$ in Eqs. (3.84) and (3.85). The use of the modified weights can be illustrated by considering Eq. (3.83) from the Gaussian quadrature perspective,

$$\begin{aligned} \delta_{g'g} &= \int_0^{+\infty} dx \exp(-x) \mathcal{L}_{g'}(x) \mathcal{L}_g(x) = \sum_{g''=0}^{G-1} w_{g''}^{[0,+\infty)} \mathcal{L}_{g'}(x_{g''}^{[0,+\infty)}) \mathcal{L}_g(x_{g''}^{[0,+\infty)}) \\ &= \int_0^{+\infty} dx \tilde{\mathcal{L}}_{g'}(x) \tilde{\mathcal{L}}_g(x) = \sum_{g''=0}^{G-1} \tilde{w}_{g''}^{[0,+\infty)} \tilde{\mathcal{L}}_{g'}(x_{g''}^{[0,+\infty)}) \tilde{\mathcal{L}}_g(x_{g''}^{[0,+\infty)}). \end{aligned} \quad (3.87)$$

This also inspires us to define the Gauss-Laguerre and Gauss-Laguerre-Radau DVR basis functions over the interval $[0, +\infty)$. With the quadrature points $\left\{x_g^{[0,+\infty)}\right\}_{g=0}^{G-1}$ and the modified quadrature weights $\left\{\tilde{w}_g^{[0,+\infty)}\right\}_{g=0}^{G-1}$, for the interval $[0, +\infty)$ we construct the corresponding DVR basis functions

$$\tilde{f}_g(x) = \frac{\exp\left[-\frac{1}{2}(x - x_g^{[0,+\infty)})\right] \pi_g^{[0,+\infty)}(x)}{\sqrt{\tilde{w}_g^{[0,+\infty)}}}, \quad (g = 0, \dots, G - 1), \quad (3.88)$$

where $\pi_g^{[0,+\infty)}(x)$ is the corresponding Lagrange polynomial [similar to Eqs. (3.31) and (3.48)]. The orthonormality of the basis set over the interval $[0, +\infty)$ can be easily verified by applying the quadrature rule, i.e.,

$$\int_0^{+\infty} dx \tilde{f}_{g'}(x) \tilde{f}_g(x) = \sum_{g''=0}^{G-1} \tilde{w}_{g''}^{[0,+\infty)} \tilde{f}_{g'}(x_{g''}^{[0,+\infty)}) \tilde{f}_g(x_{g''}^{[0,+\infty)}) = \delta_{g'g}. \quad (3.89)$$

To illustrate the Gauss-Laguerre-Radau DVR basis functions that are used in the irECS method, we consider the interval $[0, +\infty)$ discretized by 5 Gauss-Laguerre-Radau DVR basis functions [Eq. (3.88)] as a simple example. The basis functions are plotted in Figure 3.2. As one can see, the distance between adjacent quadrature

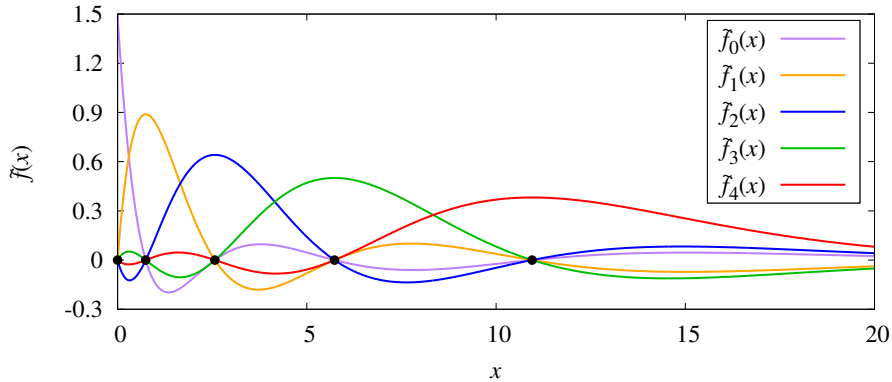


Figure 3.2: A set of the Gauss-Laguerre-Radau DVR basis functions $\left\{ \tilde{f}_g(x) \right\}_{g=0}^4$ for the interval $[0, +\infty)$. The black solid dots indicate the corresponding quadrature points.

points $\left(x_{g+1}^{[0,+\infty)} - x_g^{[0,+\infty)} \right)$ increases with the index g , which means that there are more basis functions distributed close to 0. Note that such a basis set can well represent exponentially-damping functions, which lays a foundation for the success of the irECS method. In practical calculations, we typically use 40 \sim 100 Gauss-Laguerre-Radau DVR basis functions for discretizing the outer regions.

The DVR method for the infinite-range outer region $[+r_c, +\infty)$ or $(-\infty, -r_c]$ can be obtained by a simple variable change

$$x \in [0, +\infty) \mapsto (+\beta^{-1}x + r_c) \in [+r_c, +\infty) \text{ or } (-\beta^{-1}x - r_c) \in (-\infty, -r_c], \quad (3.90)$$

where β is a positive factor that can be tuned for good performance. The irECS method can then be implemented by combining the Gauss-Legendre-Lobatto DVR for the inner region and the Gauss-Laguerre-Radau DVR for the outer regions. In this sense it is simply an efficient implementation of the ECS method by replacing the Gauss-Legendre-Lobatto DVR with the Gauss-Laguerre-Radau DVR in the outer regions. The construction of the orthonormal basis set for the irECS method essentially follows Eqs. (3.75)-(3.78), and the matrix elements of the operators can be evaluated by applying the quadrature rules^[vii].

Although the irECS method is tested to be a well-performed absorber for the TDSE simulations [172, 173], its applications are still not widespread so far. In one of our published papers [93], where the considered laser interactions are in the

^[vii]In contrast to the original formulation of the irECS method [172], our approach explicitly makes use of the Gauss-Laguerre-Radau DVR for the outer regions, which simplifies the implementation of the irECS absorber.

long-wavelength (NIR) regime, the irECS technique is employed. The choice of β is found to be uncritical for the irECS method [172]. In our calculations we simply use $\beta = 1$.

3.5 One-dimensional TDSE Examples

In this section we will give some illustrative examples of the 1D TDSE simulations, which are numerically solved by using the FEDVR discretization and the Arnoldi-Lanczos short-time propagator.

One-electron TDSE in One Dimension

The 1D one-electron TDSE is given by Eqs. (3.11) and (3.12). Here we consider the 1D hydrogen model with a soft-core Coulomb potential

$$V(x) = \frac{-1}{\sqrt{x^2 + 2}}. \quad (3.91)$$

The corresponding ground-state energy (obtained with the ITP method) is $E_g = -0.5$, which is the same as a real hydrogen atom.

With the ground state chosen as the initial state, for the real time propagation we consider a 2-cycle laser pulse with sine-squared envelope

$$A(t) = \begin{cases} -\frac{F_0}{\omega} \sin^2\left(\frac{\omega t}{4}\right) \sin(\omega t), & 0 \leq t \leq \frac{4\pi}{\omega} \\ 0, & \text{else} \end{cases} \quad (3.92)$$

with $F_0 = 0.0755$ and $\omega = 0.0285$, which correspond to a laser intensity of 2×10^{14} W/cm² and a long wavelength of 1600 nm. As discussed in §3.3, the dimension of the Krylov subspace is adaptively controlled when propagating the wave function. For a fixed time-step size $\Delta t = 0.01$ used in our calculations, the dimension of the Krylov subspace is less than 20.

We perform reference calculations (without absorbing boundary conditions) by using a large simulation volume $[-10000, +10000]$, discretized by 10000 equally-sized finite elements and 11 Gauss-Legendre-Lobatto DVR functions (quadrature points) in each element, i.e., $G_\xi = 11$ ($\xi = 1, \dots, 10000$). Therefore the total number of the FEDVR basis functions is 99999. To see how the wave function is modified by the laser pulse, we simply take a view of the probability density $|\Psi(x, t)|^2$ at $t = 1000$, which is larger the laser pulse duration. We first compare the reference calculations based the reduced VG TDSE and the LG TDSE, as shown in Figure 3.3.

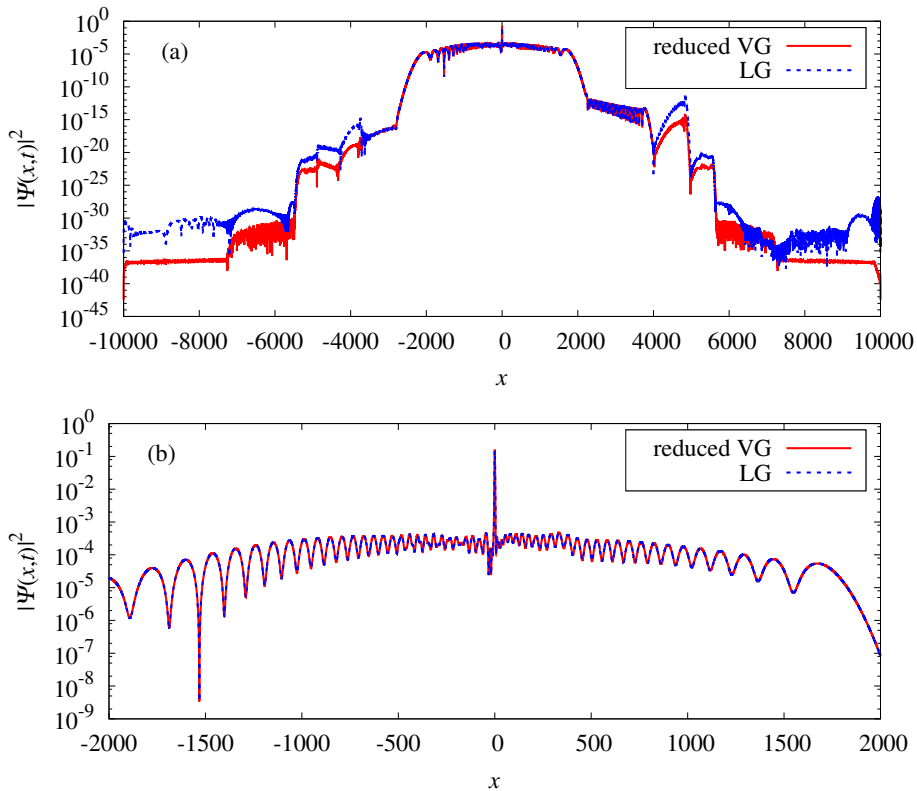


Figure 3.3: (a) The probability density $|\Psi(x,t)|^2$ at $t = 1000$, calculated from the reduced VG (red solid line) and the LG (blue dotted line) TDSE. (b) A zoom-in of (a) for the region $|x| < 2000$.

As mentioned in §2.2, the numerical performance of different gauges may be different. This can be observed from Figure 3.3(a), i.e., the results of the reduced VG TDSE and the LG TDSE indeed show some disagreement for large $|x| > 3000$. However, the differences are very weak signals, and they are actually related to the numerical errors. As seen from Figure 3.3(b), good agreement can be observed in the region $|x| < 2000$. So one can conclude that the reduced VG TDSE and the LG TDSE are consistent within acceptable accuracy. Also, it seems that the reduced VG TDSE is more preferable because the corresponding numerical errors are relatively smaller [see the region $|x| > 7000$ in Figure 3.3(a)].

Then we can demonstrate that the irECS method is indeed an efficient and well-performed absorber. For the considered laser parameters, the quiver radius of the electron is $\alpha_0 = \frac{F_0}{\omega^2} \approx 93$. So we define the inner region $[-100, +100]$ discretized by 100 equally-sized finite elements and 11 Gauss-Legendre-Lobatto DVR functions in

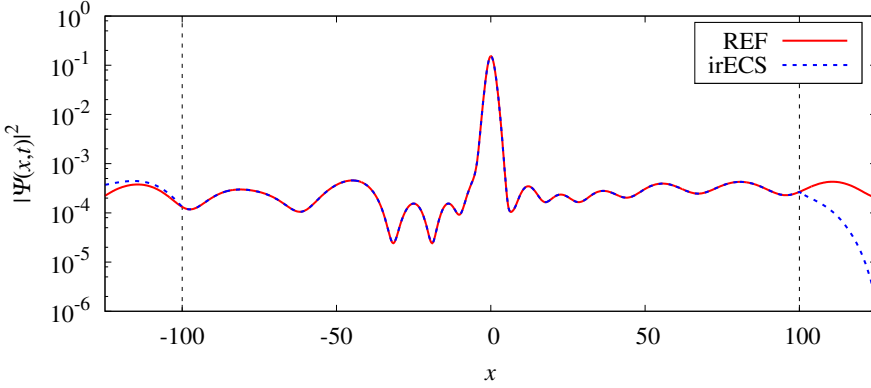


Figure 3.4: The probability density $|\Psi(x, t)|^2$ at $t = 1000$, calculated from the reduced VG TDSE without absorbing boundary conditions (red solid line) and that with the irECS method (blue dotted line).

each element. According to the irECS technique, the outer regions $[+100, +\infty)$ and $(-\infty, -100]$ are discretized by 100 Gauss-Laguerre-Radau DVR functions. Therefore the total number of the FEDVR basis functions with the irECS technique is only 1199. A scaling angle $\eta = 0.3$ is used in this example. The irECS method is applied in the reduced VG TDSE, and we compare the probability density $|\Psi(x, t)|^2$ at $t = 1000$ between the reference (the reduced VG TDSE with no absorber) and the irECS results. As shown in Figure 3.4, the irECS method can perfectly reproduce the probability density $|\Psi(x, t)|^2$ at $t = 1000$ in the inner region $|x| < 100$. In fact, the irECS method can keep the inner-region wave function exact at any time, which is important for extracting observables from the inner-region wave function. This example proves that the irECS technique is indeed a reliable absorber for the TDSE simulations.

Two-electron TDSE in One Dimension

Here we consider the 1D two-electron TDSE

$$i \frac{\partial}{\partial t} \Psi(x_1, x_2, t) = H(x_1, x_2, t) \Psi(x_1, x_2, t), \quad (3.93)$$

with the model Hamiltonian expressed in the reduced VG as

$$H(x_1, x_2, t) = \sum_{J=1}^2 \left[-\frac{1}{2} \frac{\partial^2}{\partial x_J^2} - iA(t) \frac{\partial}{\partial x_J} + \frac{-2}{\sqrt{x_J^2 + 0.5}} \right] + \frac{1}{\sqrt{(x_1 - x_2)^2 + 0.328}}. \quad (3.94)$$

In the field-free case $A(t) = 0$, the ground-state energy of this 1D model is -2.903 , which is the same as the real helium atom. Also, the ionic ground-state energy is -2.0 , which is the same as the real helium ion He^+ .

Contrary to the 1D one-electron TDSE, for the 1D two-electron model we do not have reference calculations performed with a large simulation volume. In view of the fact that the irECS method is tested to be an efficient and well-performed absorber in the 1D one-electron case, here we also apply the irECS technique for the 1D two-electron TDSE. For each electron x_1 or x_2 , the inner region $[-50, +50]$ is discretized by 50 equally-sized finite elements and 11 Gauss-Legendre-Lobatto DVR functions in each element, while the outer regions $[+50, +\infty)$ and $(-\infty, -50]$ are discretized by 50 Gauss-Laguerre-Radau DVR functions. We simply use the products of the 1D one-electron basis functions as the two-electron basis functions, and the total number of the two-electron basis functions is then 599^2 in this example. The scaling angle for this two-electron example is chosen to be $\eta = 0.2$.

With the two-electron ground state chosen as the initial state, for the real time propagation we consider a δ -like vector potential

$$A(t) = -0.0002 \exp \left[\frac{(t-1)^2}{2(0.1)^2} - \frac{1}{2} \right], \quad (3.95)$$

as a “kick” to the model. We record the dipole

$$d(t) = \iint dx_1 dx_2 \left[(x_1 + x_2) \left| \Psi(x_1, x_2, t) \right|^2 \right], \quad (3.96)$$

over a long time $0 \leq t \leq 4000$ (with a time-step size $\Delta t = 0.002$), and then perform a Fourier transform

$$D(\Omega) = \mathcal{F}[d(t)]. \quad (3.97)$$

Since many dipole-allowed transitions can be induced by the δ -like field, one can observe the corresponding energy differences between states from the spectral intensity $|D(\Omega)|^2$. This approach, similar to the dipole excitation spectra calculated in Refs. [143, 166]^[viii], can provide some information about the energy levels of the model system. We plot the spectral intensity $|D(\Omega)|^2$ in Figure 3.5. The spectral peaks correspond to the energy differences between states. As one can see, there are several bound states of the model helium below the ionic ground-state energy -2.0 . The ionization potential from the ground-state model He to the ground-state model He^+ is 0.903 , which is shown in Figure 3.5 as the first vertical arrow. The peaks above this ionization potential (see the green area in Figure 3.5) are signatures

^[viii]Instead of applying a δ -like dipole excitation in the LG as in Refs. [143, 166], here we use a δ -like “kick” of the vector potential $A(t)$, because the irECS method used in this example works in the VG (and the reduced VG) only.

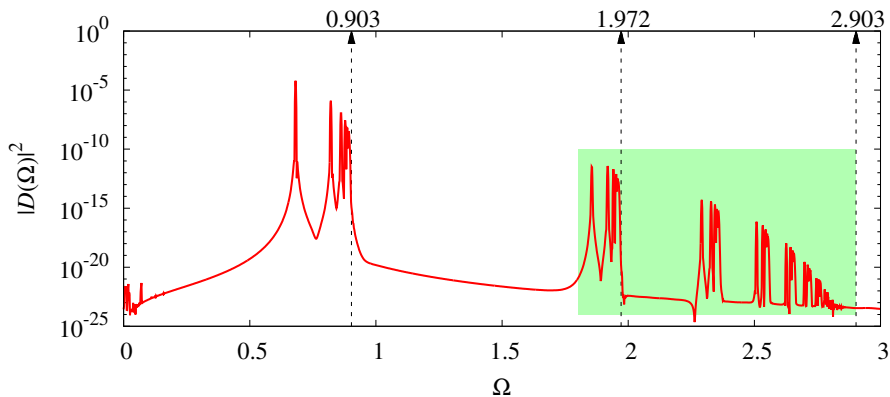


Figure 3.5: The δ -like “kick” spectral intensity $|D(\Omega)|^2$ [Eq. (3.97)]. Three arrows, from left to right, indicate the ionization potentials from the ground-state model atom to the ground-state singly-ionized ion, the first-excited-state singly-ionized ion and the doubly-ionized ion, respectively. The spectral peaks in the green area are signatures of some doubly-excited states.

of some doubly-excited states of the model helium. Also, the multiple continua of the two-electron model can be clearly seen from the spectrum. For example, the first-excited-state model He^+ has an ionic energy of -0.931 , which determines the corresponding ionization potential (for single ionization of the model helium) to be 1.972 (see the second vertical arrow in Figure 3.5).

One can conclude from this example that some features of a real two-electron atom, such as the multiple continua and the doubly-excited states, are actually reflected in the 1D two-electron model. Therefore the numerical simulations of the 1D two-electron model may to some extent provide insights into some two-electron problems that are introduced in §1.2.

Extraction of Continuum Information

In the research of strong-field ionization by laser pulses, we are usually interested in the continuum information, i.e., the photoelectron energy spectra or momentum distributions.

The most straightforward approach to extract such information is to project the final state onto the exact scattering states after the laser pulse. For simplicity, here we consider the SAE model for example. The momentum-resolved ionization probability can be computed as

$$\frac{d\mathcal{P}}{d\mathbf{k}} = \left| \langle \psi_{\mathbf{k}} | \Psi(t_p) \rangle \right|^2, \quad (4.1)$$

where $|\Psi(t_p)\rangle$ is the state corresponding to the ending time of the laser pulse t_p and $|\psi_{\mathbf{k}}\rangle$ is the outgoing state with an asymptotic momentum \mathbf{k} according to the scattering theory [11]. For hydrogen-like atoms, the scattering states are known analytically in terms of Coulomb wave functions. However, it is not a trivial task to construct the exact scattering states for a general atomic or molecular system. So we seek for other approximate approaches that do not require the exact scattering states. As shown in Ref. [174], we can extract the continuum information by performing a projection onto plane waves after a long time propagation, i.e.,

$$\frac{d\mathcal{P}}{d\mathbf{k}} = \lim_{t \rightarrow +\infty} \left| \langle \tilde{\chi}_{\mathbf{k}} | \Psi_C(t_p + t) \rangle \right|^2, \quad (4.2)$$

where $|\Psi_C(t_p + t)\rangle$ stands for the continuum part of the state after the laser pulse and $|\tilde{\chi}_{\mathbf{k}}\rangle$ is the 3D plane wave given by

$$\tilde{\chi}_{\mathbf{k}}(\mathbf{r}) = (2\pi)^{-3/2} \exp(i\mathbf{k} \cdot \mathbf{r}). \quad (4.3)$$

In Eq. (4.2) it is necessary to project out all the bound states $|\psi_{\mathbf{n}}\rangle$ due to the non-orthogonality $\langle \tilde{\chi}_{\mathbf{k}} | \psi_{\mathbf{n}} \rangle \neq 0$.

In fact, the bound states are mainly localized in an inner zone ($|\mathbf{r}| < r_s$) where the Coulomb interaction is important. Meanwhile, the continuum states will eventually go out of the inner zone. If we perform the projection only in the outer zone ($|\mathbf{r}| \geq r_s$) where the bound states can be approximately neglected, we may skip the

procedure of projecting out all the bound states $|\psi_n\rangle$ in Eq. (4.2). This gives an approximate approach to compute the momentum-resolved ionization probability

$$\frac{d\mathcal{P}}{d\mathbf{k}} \approx \lim_{t \rightarrow +\infty} \left| \langle \tilde{\chi}_k | \Theta | \Psi(t_p + t) \rangle \right|^2, \quad (4.4)$$

where $\Theta = \theta(|\mathbf{r}| - r_s)$ stands for the Heaviside step function.

In principle, Eq. (4.4) can give accurate results in the limit of an infinitely-large simulation volume and infinitely-long time propagation. Instead of performing the projection which requires an accurate wave function in the large outer zone, we can extract the same information by analyzing the flux passing through the surface defined by r_s . Such a flux analysis is referred to as the time-dependent surface flux (tSURFF) method [175], in which the wave function in the outer zone is not required for extracting the continuum information. Combined with efficient absorbers, the tSURFF method enables us to calculate the photoelectron spectra within a small simulation volume.

Details about the tSURFF method will be discussed in the remaining part of this chapter. Although we only present some applications of the tSURFF method for the 1D model atoms, the tSURFF method itself is applicable for the 3D systems with one or two active electrons [128, 175, 176]. It was also extended to diatomic molecular models for studying the dissociative ionization [177]. For completeness, here we will introduce the tSURFF method for one-electron and two-electron atomic systems in the 3D case, and briefly discuss its adaptation to the 1D case.

4.1 One-electron Time-dependent Surface Flux Method

In this section we will formulate the tSURFF method for one electron within the dipole approximation. The 3D Hamiltonian for one electron in the laser field reads

$$H(\mathbf{r}, t) = \begin{cases} \frac{[\mathbf{p} + \mathbf{A}(t)]^2}{2} + V(\mathbf{r}), & \text{VG} \\ \frac{\mathbf{p}^2}{2} - \frac{\partial}{\partial t} \mathbf{A}(t) \cdot \mathbf{r} + V(\mathbf{r}), & \text{LG} \end{cases}. \quad (4.5)$$

To perform the time-dependent surface flux analysis, we need to know the time evolution of the electron after passing through the surface [175]. We assume that the interaction $V(\mathbf{r})$ can be neglected in the outer zone ($|\mathbf{r}| \geq r_s$), and use the Volkov Hamiltonian

$$H_V(\mathbf{r}, t) = \begin{cases} \frac{[\mathbf{p} + \mathbf{A}(t)]^2}{2}, & \text{VG} \\ \frac{\mathbf{p}^2}{2} - \frac{\partial}{\partial t} \mathbf{A}(t) \cdot \mathbf{r}, & \text{LG} \end{cases}, \quad (4.6)$$

for describing the corresponding electron motion in the laser field. In principle, this approach is exact for the case of a short-range potential, i.e., if $V(\mathbf{r}) = 0$ for $(|\mathbf{r}| \geq r_s)$. In the case of a long-range Coulomb potential, the induced error can be controlled by increasing the surface radius r_s .

The Volkov solutions are analytically known:

$$\chi_{\mathbf{k}}(\mathbf{r}, t) = \begin{cases} (2\pi)^{-3/2} \exp[-iS_{\mathbf{k}}(t)] \exp(i\mathbf{k} \cdot \mathbf{r}), & \text{VG} \\ (2\pi)^{-3/2} \exp[-iS_{\mathbf{k}}(t)] \exp\{i[\mathbf{k} + \mathbf{A}(t)] \cdot \mathbf{r}\}, & \text{LG} \end{cases}, \quad (4.7)$$

where $S_{\mathbf{k}}(t)$ is a time-dependent phase given by

$$S_{\mathbf{k}}(t) = \int_{-\infty}^t dt' \frac{|\mathbf{k} + \mathbf{A}(t')|^2}{2}. \quad (4.8)$$

For a laser pulse with $\mathbf{A}(t \rightarrow \pm\infty) = 0$, the projection onto the plane waves in Eq. (4.4) can be replaced by the projection onto the Volkov solutions. Then we calculate the momentum-resolved ionization probability at a sampling time $t_s > t_p$ (after the laser pulse) and rewrite the projection as^[i]

$$\begin{aligned} P_{\mathbf{k}}(t_s) &= \langle \chi_{\mathbf{k}}(\mathbf{r}, t_s) | \Theta | \Psi(\mathbf{r}, t_s) \rangle \\ &= \int_{-\infty}^{t_s} dt \left[\frac{\partial}{\partial t} \langle \chi_{\mathbf{k}}(\mathbf{r}, t) | \Theta | \Psi(\mathbf{r}, t) \rangle \right] \\ &= i \int_{-\infty}^{t_s} dt \langle \chi_{\mathbf{k}}(\mathbf{r}, t) | [H_V(\mathbf{r}, t)\Theta - \Theta H(\mathbf{r}, t)] | \Psi(\mathbf{r}, t) \rangle \\ &= i \int_{-\infty}^{t_s} dt \langle \chi_{\mathbf{k}}(\mathbf{r}, t) | [H_V(\mathbf{r}, t), \Theta] | \Psi(\mathbf{r}, t) \rangle. \end{aligned} \quad (4.9)$$

Note that the commutator

$$[H_V(\mathbf{r}, t), \Theta] = \begin{cases} \frac{1}{2} [\mathbf{p}^2, \Theta] + [\mathbf{A}(t) \cdot \mathbf{p}, \Theta], & \text{VG} \\ \frac{1}{2} [\mathbf{p}^2, \Theta], & \text{LG} \end{cases} \quad (4.10)$$

gives a non-vanishing contribution only on the surface. Therefore the wave function beyond the surface is not required by the tSURFF method, which allows us to solve the TDSE with absorbing boundary conditions. This implies that the surface in the tSURFF method should be placed where the wave function is not affected by the

^[i]In this chapter, we sometimes put the “wave function” into the bra-ket notation [see, e.g., Eqs. (4.9) and (4.15)]. This notation, although inappropriate, is introduced as an easy way to keep track of the dimensionality (especially in §4.2), and it should still be seen as a representation-independent state according to the conventional bra-ket notation.

absorber used in the TDSE simulations. So we always choose $r_s < r_c$, with r_c the radius for the absorber introduced in §3.4.

In spherical coordinates (r, ϑ, φ) ^[ii], applying the commutator $[\mathbf{p}^2, \Theta]$ on a function $f(r, \vartheta, \varphi)$ gives

$$\begin{aligned} [\mathbf{p}^2, \Theta] f(r, \vartheta, \varphi) = & -\delta(r - r_s) \left\{ \frac{1}{r^2} \frac{\partial}{\partial r} [r^2 f(r, \vartheta, \varphi)] + \frac{\partial}{\partial r} f(r, \vartheta, \varphi) \right\} \\ & - f(r, \vartheta, \varphi) \frac{\partial}{\partial r} \delta(r - r_s), \end{aligned} \quad (4.11)$$

where the last term containing the derivative of $\delta(r - r_s)$ can be treated by partial integration in the evaluation of the inner product. For a laser field described by the vector potential (in Cartesian coordinates) $\mathbf{A}(t) = [A_x(t), A_y(t), A_z(t)]$, applying the commutator $[\mathbf{A}(t) \cdot \mathbf{p}, \Theta]$ on a function $f(r, \vartheta, \varphi)$ gives

$$\begin{aligned} [\mathbf{A}(t) \cdot \mathbf{p}, \Theta] f(r, \vartheta, \varphi) = \\ -i\delta(r - r_s) \left[A_x(t) \sin(\vartheta) \cos(\varphi) + A_y(t) \sin(\vartheta) \sin(\varphi) + A_z(t) \cos(\vartheta) \right] f(r, \vartheta, \varphi). \end{aligned} \quad (4.12)$$

Similarly, we have expressions for the commutators in the 1D case:

$$[\mathbf{p}^2, \theta(|x| - r_s)] f(x) = -\text{sgn}(x) \left[2\delta(|x| - r_s) \frac{\partial}{\partial x} f(x) + f(x) \frac{\partial}{\partial x} \delta(|x| - r_s) \right], \quad (4.13)$$

$$[\mathbf{A}(t)p, \theta(|x| - r_s)] f(x) = -i \text{sgn}(x) A(t) \delta(|x| - r_s) f(x). \quad (4.14)$$

With the 1D Volkov solutions given by Eqs. (3.71) and (3.72), for the 1D tSURFF method we evaluate the flux term

$$\begin{aligned} \langle \chi_k(x, t) | [H_V(x, t), \theta(|x| - r_s)] |\Psi(x, t)\rangle = \\ -\frac{1}{2} (2\pi)^{-1/2} \exp[iS_k(t)] \\ \times \begin{cases} \exp(-ikx) \left\{ \frac{\partial}{\partial x} \Psi(x, t) + i[k + 2A(t)]\Psi(x, t) \right\} \text{sgn}(x) \Big|_{x=\pm r_s}, & \text{VG} \\ \exp\{-i[k + A(t)]x\} \left\{ \frac{\partial}{\partial x} \Psi(x, t) + i[k + A(t)]\Psi(x, t) \right\} \text{sgn}(x) \Big|_{x=\pm r_s}, & \text{LG} \end{cases} \end{aligned} \quad (4.15)$$

In the 1D case, an outgoing wave with a positive momentum ($k > 0$) will eventually go through the surface ($x = +r_s$) while that with a negative momentum ($k < 0$) will eventually go through the surface ($x = -r_s$). Thus in the 1D tSURFF method we perform the tSURFF analysis at ($x = +r_s$) and ($x = -r_s$) for positive and negative final momenta, respectively.

^[ii]In the 3D implementation, the wave function is typically expanded into spherical harmonics (see, e.g., Refs. [107, 128]).

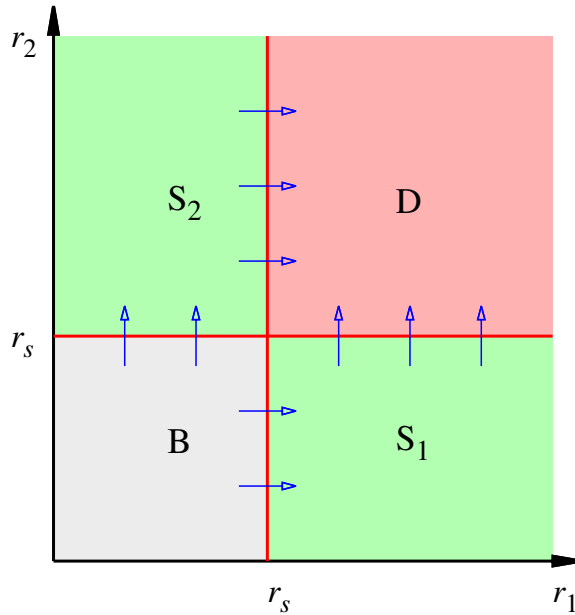


Figure 4.1: Partitioning of the two-electron coordinate space ($|\mathbf{r}_1|, |\mathbf{r}_2|$) into bound (B), singly ionized (S_1, S_2) and doubly ionized (D) regions. The arrows acrossing the surfaces indicate the flux that should be analyzed for ionization.

4.2 Two-electron Time-dependent Surface Flux Method

The tSURFF method can be extended to the two-electron case for both single and double ionization [128, 176]. Similar to the one-electron case, the key idea is to partition the coordinate space into different regions with surfaces. As shown in Figure 4.1, the two-electron coordinate space is partitioned into bound (B), singly ionized (S_1, S_2) and doubly ionized (D) regions.

We need to make reasonable assumptions for the time evolution after for the two-electron wave function passing through the surface. In both velocity and length gauges, the total Hamiltonian for the two electrons can be written as

$$H(\mathbf{r}_1, \mathbf{r}_2, t) = H_V(\mathbf{r}_1, t) + H_V(\mathbf{r}_2, t) + V_{e-n}(\mathbf{r}_1) + V_{e-n}(\mathbf{r}_2) + V_{e-e}(\mathbf{r}_1, \mathbf{r}_2) \quad (4.16)$$

where H_V is the one-electron Volkov Hamiltonian, V_{e-n} and V_{e-e} are the electron-nucleus and electron-electron interactions, respectively. As in the one-electron case, here we still restrict to a laser pulse with $\mathbf{A}(t \rightarrow \pm\infty) = 0$, which ensures

$$H_V(\mathbf{r}_J, t \rightarrow \pm\infty) = \frac{p_J^2}{2}, \quad (J = 1, 2). \quad (4.17)$$

Double Ionization

We first consider the case of double ionization. In the zone D defined by ($|\mathbf{r}_1| \geq r_s$) and ($|\mathbf{r}_2| \geq r_s$), we assume that the two electrons are described by a product of Volkov states. By introducing the notation $\Theta_J = \theta(|\mathbf{r}_J| - r_s)$ ($J = 1, 2$), for double ionization we evaluate the projection

$$\begin{aligned} P_{\mathbf{k}_1 \mathbf{k}_2}(t_s) &= \langle \chi_{\mathbf{k}_1}(\mathbf{r}_1, t_s) \chi_{\mathbf{k}_2}(\mathbf{r}_2, t_s) | \Theta_1 \Theta_2 | \Psi(\mathbf{r}_1, \mathbf{r}_2, t_s) \rangle \\ &= \int_{-\infty}^{t_s} dt \left[\frac{\partial}{\partial t} \langle \chi_{\mathbf{k}_1}(\mathbf{r}_1, t) \chi_{\mathbf{k}_2}(\mathbf{r}_2, t) | \Theta_1 \Theta_2 | \Psi(\mathbf{r}_1, \mathbf{r}_2, t) \rangle \right] \\ &= i \int_{-\infty}^{t_s} dt [F_1(\mathbf{k}_1, \mathbf{k}_2, t) + F_2(\mathbf{k}_1, \mathbf{k}_2, t)] \end{aligned} \quad (4.18)$$

with the surface flux

$$F_1(\mathbf{k}_1, \mathbf{k}_2, t) = \langle \chi_{\mathbf{k}_1}(\mathbf{r}_1, t) \chi_{\mathbf{k}_2}(\mathbf{r}_2, t) | [H_V(\mathbf{r}_2, t), \Theta_2] \Theta_1 | \Psi(\mathbf{r}_1, \mathbf{r}_2, t) \rangle, \quad (4.19)$$

$$F_2(\mathbf{k}_1, \mathbf{k}_2, t) = \langle \chi_{\mathbf{k}_1}(\mathbf{r}_1, t) \chi_{\mathbf{k}_2}(\mathbf{r}_2, t) | [H_V(\mathbf{r}_1, t), \Theta_1] \Theta_2 | \Psi(\mathbf{r}_1, \mathbf{r}_2, t) \rangle. \quad (4.20)$$

The electron exchange symmetry ensures $F_2(\mathbf{k}_1, \mathbf{k}_2, t) = F_1(\mathbf{k}_2, \mathbf{k}_1, t)$, so we only need to evaluate $F_1(\mathbf{k}_1, \mathbf{k}_2, t)$ in practice.

With a set of one-electron time-independent basis functions $\{f_n(\mathbf{r})\}$, which is assumed to be orthonormal and complete, $F_1(\mathbf{k}_1, \mathbf{k}_2, t)$ can be expressed as

$$\begin{aligned} F_1(\mathbf{k}_1, \mathbf{k}_2, t) &= \sum_n \langle \chi_{\mathbf{k}_2}(\mathbf{r}_2, t) | [H_V(\mathbf{r}_2, t), \Theta_2] | f_n(\mathbf{r}_2) \rangle \\ &\quad \times \langle f_n(\mathbf{r}_2) \chi_{\mathbf{k}_1}(\mathbf{r}_1, t) | \Theta_1 | \Psi(\mathbf{r}_1, \mathbf{r}_2, t) \rangle. \end{aligned} \quad (4.21)$$

As shown in Eqs. (4.10)-(4.12), the one-electron commutator $[H_V(\mathbf{r}_2, t), \Theta_2]$ can be easily evaluated. Meanwhile, for $\langle f_n(\mathbf{r}_2) \chi_{\mathbf{k}_1}(\mathbf{r}_1, t) | \Theta_1 | \Psi(\mathbf{r}_1, \mathbf{r}_2, t) \rangle$ we need to solve an inhomogeneous time-dependent equation

$$\begin{aligned} \frac{\partial}{\partial t} \langle f_n(\mathbf{r}_2) \chi_{\mathbf{k}_1}(\mathbf{r}_1, t) | \Theta_1 | \Psi(\mathbf{r}_1, \mathbf{r}_2, t) \rangle &= \\ -i \sum_m \langle f_n(\mathbf{r}_2) | [H_V(\mathbf{r}_2, t) + V_{e-n}(\mathbf{r}_2)] | f_m(\mathbf{r}_2) \rangle \langle f_m(\mathbf{r}_2) \chi_{\mathbf{k}_1}(\mathbf{r}_1, t) | \Theta_1 | \Psi(\mathbf{r}_1, \mathbf{r}_2, t) \rangle \\ +i \sum_m \langle \chi_{\mathbf{k}_1}(\mathbf{r}_1, t) | [H_V(\mathbf{r}_1, t), \Theta_1] | f_m(\mathbf{r}_1) \rangle \langle f_m(\mathbf{r}_1) f_n(\mathbf{r}_2) | \Psi(\mathbf{r}_1, \mathbf{r}_2, t) \rangle. \end{aligned} \quad (4.22)$$

This is the key equation for the two-electron tSURFF method, which should be propagated together with the two-electron TDSE. Note that in the above derivation we have not imposed any absorbing boundary conditions, i.e., the wave function $\Psi(\mathbf{r}_1, \mathbf{r}_2, t)$ is still assumed to be exact over all space in Eqs. (4.21) and (4.22). Due

to the one-electron commutator $[H_V(\mathbf{r}_J, t), \Theta_J]$ ($J = 1, 2$) in Eqs. (4.21) and (4.22), however, the tSURFF method only requires the wave function on the surfaces to be accurate. Therefore in Eq. (4.22) we can actually replace the exact wave function $\Psi(\mathbf{r}_1, \mathbf{r}_2, t)$ with the numerical solution that is computed with absorbing boundary conditions. Correspondingly, the Hamiltonian in Eq. (4.22) should also be modified to be non-Hermitian by the absorber as introduced in §3.4.

Single Ionization

In the case of single ionization, one electron is freed while the other one is bound. We assume that the freed electron has an asymptotic momentum \mathbf{k} while the bound electron is finally in a field-free ionic state denoted by $\psi_n(\mathbf{r})$, which fulfills

$$\left[\frac{\mathbf{p}^2}{2} + V_{e-n}(\mathbf{r}) \right] \psi_n(\mathbf{r}) = E_n \psi_n(\mathbf{r}). \quad (4.23)$$

The single continuum information is extracted in the zones S_1 and S_2 , where we project the final wave function at time $t_s > t_p$ (after the laser pulse) onto a product of the Volkov state and the ionic state, i.e.,

$$\begin{aligned} P_{k,n}(t_s) = & \langle \chi_k(\mathbf{r}_1, t_s) \psi_n(\mathbf{r}_2) | \Theta_1 (1 - \Theta_2) | \Psi(\mathbf{r}_1, \mathbf{r}_2, t_s) \rangle \\ & + \langle \chi_k(\mathbf{r}_2, t_s) \psi_n(\mathbf{r}_1) | \Theta_2 (1 - \Theta_1) | \Psi(\mathbf{r}_1, \mathbf{r}_2, t_s) \rangle. \end{aligned} \quad (4.24)$$

Due to the electron exchange symmetry, the two terms in Eq. (4.24) give the same contribution. With $\langle f_n(\mathbf{r}_2) \chi_k(\mathbf{r}_1, t_s) | \Theta_1 | \Psi(\mathbf{r}_1, \mathbf{r}_2, t_s) \rangle$ already solved according to Eq. (4.22), for single ionization we simply evaluate

$$P_{k,n}(t_s) = 2 \sum_n \langle \psi_n(\mathbf{r}_2) | (1 - \Theta_2) | f_n(\mathbf{r}_2) \rangle \langle f_n(\mathbf{r}_2) \chi_k(\mathbf{r}_1, t_s) | \Theta_1 | \Psi(\mathbf{r}_1, \mathbf{r}_2, t_s) \rangle. \quad (4.25)$$

Adaptation to One Dimension

The tSURFF method for the 1D two-electron model essentially follows the above formulation. Similar to the one-electron tSURFF method, the adaptation of the two-electron tSURFF method to the 1D case is also straightforward with the replacement $\mathbf{r} \rightarrow x$. The one-electron commutator in the 1D tSURFF method can be easily evaluated according the example given by Eq. (4.15). Here we just make one remark about the basis set $\{f_n(x)\}$ used in the 1D version of Eq. (4.22).

In the 1D case, we discretize the two-electron wave function $\Psi(x_1, x_2, t)$ with the direct products of the 1D FEDVR basis functions. For convenience, we also use the 1D FEDVR basis set for $\{f_n(x)\}$ in the 1D version of Eq. (4.22). Since

the FEDVR basis functions are locally defined and the corresponding matrices are sparse, the numerical effort of solving Eq. (4.22) is reduced. In our current implementation, the 1D version of Eq. (4.22) is numerically solved by using the Runge-Kutta method^[iii].

4.3 Suppression of Rydberg-state Contributions

In Eqs. (4.9), (4.18) and (4.24), the projections still contain contributions of bound (Rydberg) states extending beyond the tSURFF surfaces. It is important to suppress this type of artificial contributions, especially for long-wavelength laser interactions, which can produce considerable Rydberg-state populations. In this section, we will show that the Rydberg-state contributions can be effectively suppressed by time averaging [128].

The Rydberg-state contributions origin from the non-orthogonality between the Volkov states and the Rydberg states. Although these contributions are to some extent suppressed in the tSURFF method by restricting the projection with Θ , they are not completely excluded. To further suppress the Rydberg-state contributions, we consider the time dependence of the projection

$$\mathcal{R}_n(\mathbf{k}, t) = \langle \chi_{\mathbf{k}}(t) | \Theta | \psi_n(t) \rangle. \quad (4.26)$$

After the laser pulse, we have trivial time dependence for both states, and $\mathcal{R}_n(\mathbf{k}, t)$ will oscillate with time,

$$\mathcal{R}_n(\mathbf{k}, t) = \mathcal{R}_n(\mathbf{k}, t_p) \exp \left[i \left(E_n - \frac{|\mathbf{k}|^2}{2} \right) (t - t_p) \right], \quad (t \geq t_p). \quad (4.27)$$

If we average $\mathcal{R}_n(\mathbf{k}, t)$ over a long time t_a after the laser pulse, the Rydberg-state contributions can be suppressed as a result of the cancellation of $\mathcal{R}_n(\mathbf{k}, t)$. Thus in the tSURFF method, we can start a time-averaging approach from time $t_s > t_p$ to suppress the Rydberg-state contributions. True outgoing flux will not be affected by the time averaging, as long as it has already passed the surface at time t_s . This time-averaging approach simply makes use of the time-dependent phase difference between the Volkov states and the Rydberg states, and it is generally applicable in the tSURFF method. For the two-electron case, the time-averaging approach allows us to suppress the Rydberg-state contributions without solving the Rydberg states.

We apply the time-averaging scheme in the tSURFF method on the basis of Eqs. (4.9), (4.18) and (4.24). Then the momentum-resolved ionization probabilities

^[iii]In my experience, it usually requires a smaller time-step size Δt to propagate Eq. (4.22) than to propagate the TDSE. The efficiency of the two-electron tSURFF method may be further improved if one can use a more stable numerical method for solving Eq. (4.22) such that it uses the same time-step size Δt as the TDSE propagation.

($\frac{d\mathcal{P}}{dk}$ for the one-electron case, $\frac{d\mathcal{P}}{dk_1 dk_2}$ for the two-electron double ionization and $\frac{d\mathcal{P}_n}{dk}$ for the two-electron single ionization in the n -th ionic channel) are calculated as

$$\frac{d\mathcal{P}}{dk} = \left| \frac{1}{t_a} \int_0^{t_a} dt P_k(t_s + t) \right|^2, \quad (4.28)$$

$$\frac{d\mathcal{P}}{dk_1 dk_2} = \left| \frac{1}{t_a} \int_0^{t_a} dt P_{k_1 k_2}(t_s + t) \right|^2, \quad (4.29)$$

$$\frac{d\mathcal{P}_n}{dk} = \left| \frac{1}{t_a} \int_0^{t_a} dt P_{k,n}(t_s + t) \exp(iE_n t) \right|^2. \quad (4.30)$$

Here the phase factor $\exp(iE_n t)$ for the ionic state $|\psi_n\rangle$ with energy E_n has to be included in Eq. (4.30), simply because the time evolution of the ionic state $|\psi_n\rangle$ is not considered in Eqs. (4.23)-(4.25).

4.4 One-dimensional Examples of the tSURFF Method

A few applications of the tSURFF method in one dimension can be found in our published papers [91–93] (see **Part Two** of this thesis). Still, in this section we will show some simple examples that can demonstrate the performance of the tSURFF method, together with the time-averaging approach for suppressing the Rydberg-state contributions.

One-electron tSURFF Method in One Dimension

The one-electron tSURFF examples are based on the 1D hydrogen model that is considered in §3.5. As discussed in §3.5, we have reference calculations performed in a large simulation volume with no absorber. In such reference calculations, we can project the final wave functions onto plane waves (in the outer regions) to extract the continuum information. Here we use the same discretization scheme for the reference calculations as in §3.5, and choose the outer zone defined by ($|x| > 55$).

The most important advantage of the tSURFF method is that it allows us to extract the continuum information in a small simulation volume with an efficient absorber. So we apply the tSURFF method combined with the irECS technique. We first consider the same laser pulse as in the one-electron TDSE example [see Eq. (3.92) in §3.5], which is in the long-wavelength regime. The FEDVR discretization details and the irECS parameters are given in §3.5, and the tSURFF radius is chosen to be $r_s = 55$. To suppress the Rydberg-state contributions, we apply the time-averaging approach for $500 \leq t \leq 1000$, which is after the pulse interaction [see Figure 4.2(a)]. The photoelectron spectra $\frac{d\mathcal{P}}{dk}$ (with $k > 0$ for this example) are

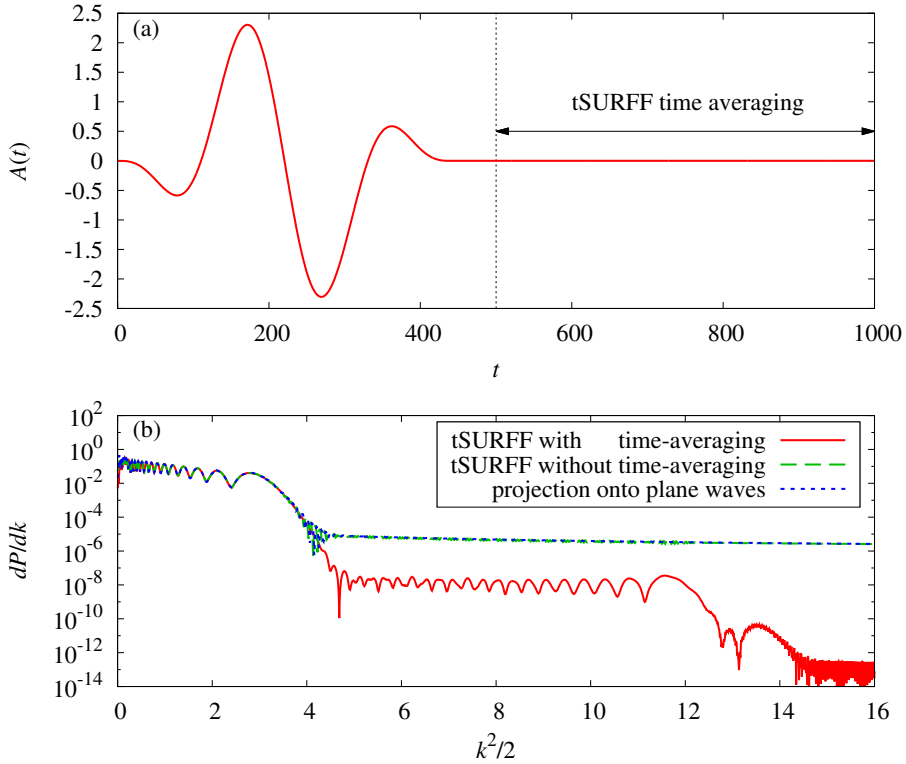


Figure 4.2: (a) The vector potential of the laser pulse, defined by Eq. (3.92). (b) The photoelectron spectra (with $k > 0$), calculated with the tSURFF method and the plane-wave projection approach.

presented in Figure 4.2(b), where we compare the tSURFF results (with and without the time-averaging approach) with the plane-wave projection performed in a large simulation volume (with no absorber).

One can observe that the tSURFF method without the time-averaging approach well reproduces the spectrum obtained by projecting the final wave functions onto plane waves, which proves the validity of the tSURFF method. In the considered long-wavelength regime, the rescattered electron should contribute to a plateau-like high-energy part in the ATI spectrum. However, the high-energy ATI spectral structures are “hidden” by the Rydberg-state contributions. By applying the time-averaging approach to suppress the Rydberg-state contributions, we are able to see the ATI plateau and cutoff features clearly. Note that for such a few-cycle pulse, the ATI cutoff energy is less than $10U_p$ (here $U_p = \frac{F_0^2}{4\omega^2} \approx 1.75$).

Then we present another example, where the laser interaction is in the short-

wavelength regime. In this example, we consider a 100-cycle long pulse

$$A(t) = \begin{cases} -\frac{F_0}{\omega} \sin^2\left(\frac{\omega t}{200}\right) \sin(\omega t), & 0 \leq t \leq \frac{200\pi}{\omega} \\ 0, & \text{else} \end{cases} \quad (4.31)$$

with $F_0 = 0.1$ and $\omega = 1.5$. In the short-wavelength case, the discretization with the irECS absorber uses a smaller basis set. Now we define the inner region $[-60, +60]$ discretized by 60 equally-sized finite elements and 11 Gauss-Legendre-Lobatto DVR functions in each element, and the outer regions $[+60, +\infty)$ and $(-\infty, -60]$ are discretized by 50 Gauss-Laguerre-Radau DVR functions. Therefore the total number of the basis functions with the irECS absorber is only 699. A scaling angle $\eta = 0.2$ is used in this example. The tSURFF method used here is the same as that used in the long-wavelength example. Also, the reference calculations (with no absorber) are performed in the same way as in the long-wavelength regime.

Similar to Figure 4.2, Figure 4.3 displays (a) the vector potential of the laser pulse and (b) the corresponding photoelectron spectra $\frac{dP}{dk}$ (with $k > 0$), which are calculated with the tSURFF method (with and without the time-averaging scheme) and the plane-wave projection approach. Since the long-pulse laser interaction has a well-defined photon energy $\hbar\omega$, we can clearly see discrete ATI peaks in the spectra. For example, the one-photon ionization produces an ATI peak at $(\hbar\omega - I_p = 1.0)$ and the two-photon ionization produces an ATI peak at $(2\hbar\omega - I_p = 2.5)$, etc. Again, one can find that the tSURFF method without the time-averaging approach nicely reproduces the photoelectron spectrum obtained by projecting the final wave functions onto plane waves.

Note that in the short-wavelength example, the discrete ATI peaks are less affected by the Rydberg-state contributions than in the long-wavelength regime. In the short-wavelength regime, if one focuses on only one or two ATI peaks in the low-energy part, the corresponding discussion will not be disturbed by the Rydberg-state contributions. Applying the time-averaging approach in the tSURFF method, however, indeed allows us to suppress the Rydberg-state contributions and improve the calculated ATI spectra, as shown in Figure 4.3(b).

Two-electron tSURFF Method in One Dimension

The two-electron tSURFF example is based on the 1D model helium atom, which is considered in §3.5 [see Eqs. (3.93) and (3.94)]. In this example we use the same discretization scheme as in §3.5 and calculate the joint energy spectra for double ionization. Here the considered laser pulse has the same form of Eq. (4.31), but has a higher frequency $\omega = 4.0$, which allows single-photon double ionization (SPDI).

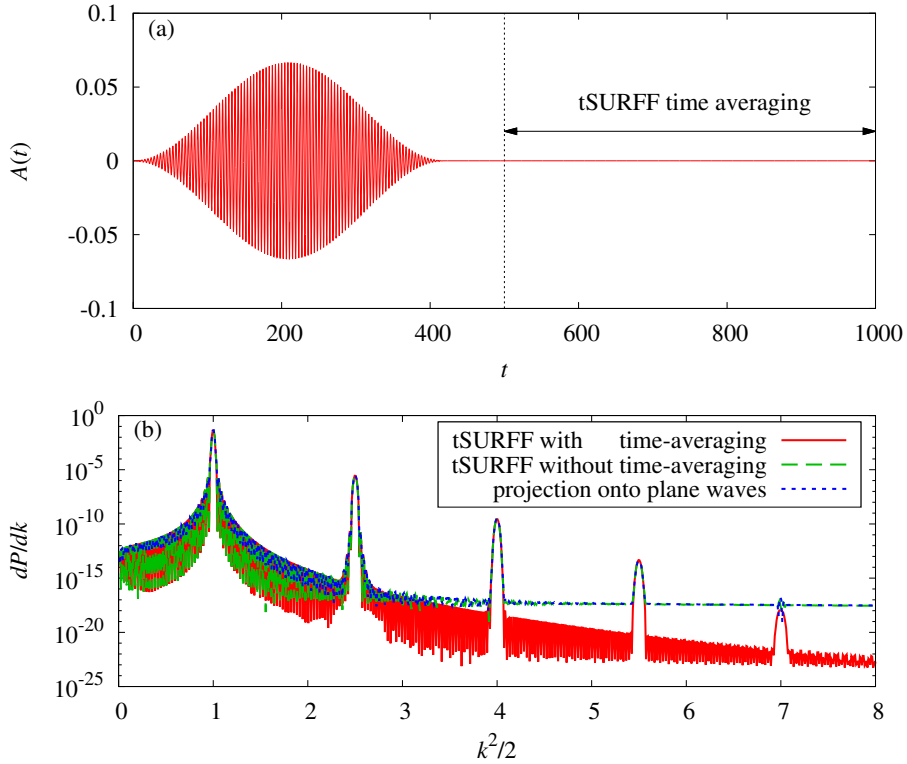


Figure 4.3: (a) The vector potential of the laser pulse, defined by Eq. (4.31). (b) The photoelectron spectra (with $k > 0$), calculated with the tSURFF method and the plane-wave projection approach.

This example has three-fold aims: (1) to confirm that the SPDI process can be simulated within the 1D model; (2) to demonstrate that the tSURFF method can be applied to extract the correlated photoelectron spectra; (3) to show that time-averaging approach can improve the calculated spectra by suppressing the Rydberg-state contributions.

In this two-electron example, we propagate the TDSE and the 1D version of Eq. (4.22) with a small time-step size $\Delta t = 0.002$, and the time-averaging approach is applied for $500 \leq t \leq 1000$. We present the joint energy photoelectron spectra $\frac{dP}{dk_1 dk_2}$ calculated with the tSURFF method in Figure 4.4. From the joint energy spectra, we first observe the SPDI energy sharing structure $(k_1^2 + k_2^2)/2 \approx 1.1$, implying that the 1D two-electron model can indeed describe the SPDI phenomenon, where the electron correlation plays an important role. In addition, the TPDI energy sharing structure $(k_1^2 + k_2^2)/2 \approx 5.1$ can also be clearly seen from the spectra. Note

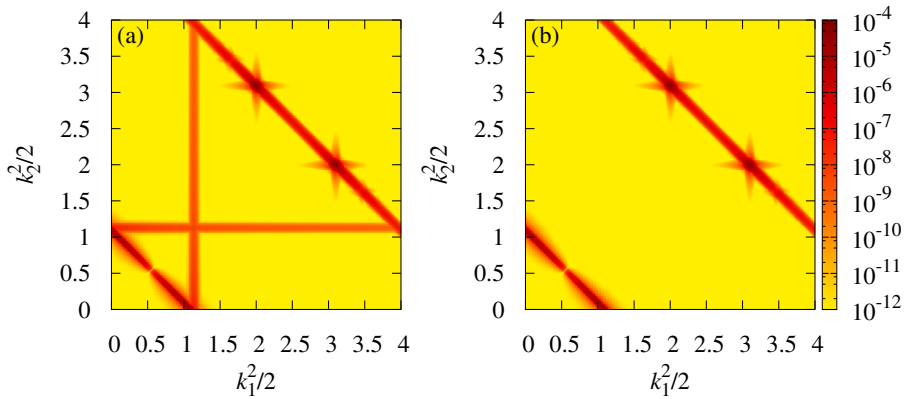


Figure 4.4: (a) The joint energy photoelectron spectrum $\frac{dP}{dk_1 dk_2}$, calculated by the tSURFF method without the time-averaging approach. (b) $\frac{dP}{dk_1 dk_2}$ calculated by the tSURFF method with the time-averaging approach [the 1D version of Eq. (4.29)].

that the maxima correspond to the sequential TPDI processes while the diagonal line characterizes the non-sequential mechanism.

If the tSURFF method is applied without the time-averaging approach, some artifacts will appear in the correlated photoelectron spectra, i.e., the lines parallel to the energy axis in Figure 4.4(a). Such artificial spectral structures originate from the Rydberg-state contributions, which can be effectively suppressed by the time-averaging approach, as shown in Figure 4.4(b).

Ionization of Helium in the XUV Regime

In this chapter we will give an overview of our published papers [91, 92], which discussed the strong-field ionization of model helium in the extreme-ultraviolet (XUV) regime. Copies of these two papers are provided in **Part Two** of this thesis (Paper I and Paper II).

5.1 Motivation

The studies on the strong-field ionization in the short-wavelength regime are to some extent motivated by the development of new light sources. Nowadays, intense XUV laser pulses with femtosecond and attosecond durations can be produced from high-order harmonics [178, 179] or free-electron lasers [180, 181]. The ultrashort laser pulses provide the opportunity of monitoring ultrafast dynamics on their natural time scales [2, 182]. Besides, the laser fields with unprecedented high intensity may induced new phenomena.

As introduced in Chapter 1, the intense high-frequency laser pulses may lead to strong-field ionization in the stabilization regime. In view of the fact that the studies on stabilization of multi-electron systems are still scarce, we reconsidered the stabilization of two-electron atoms in Paper I [91]. We asked a question: if the high-frequency stabilization condition ($\hbar\omega > I_p$) is only fulfilled for the lowest single ionization channel, will stabilization happen or not? As mention in §1.2, this question would, to some degree, provide clarification of the stabilization concept for multi-electron systems, which have multiple continua. In addition to studying the total, single and double ionization probabilities as a function of the field strength, we also took a detailed view of the probabilities into specific ionization channels, which are seldom investigated in the research of stabilization. We expected that the channel-resolved ionization probabilities could provide some insight of the strong-field dynamics in the XUV regime.

In Paper II [92] we considered a similar laser-frequency regime, but focused on different aspects. Instead of investigating the field-strength dependence of the channel-resolved ionization probabilities, we analyzed the channel-resolved pho-

photoelectron energy spectra for some specific laser parameters. Regarding the double ionization of helium, the considered laser frequency allows the non-sequential TPDI but not the sequential TPDI. In the strong-field scenario, however, the sequential double ionization is still possible via multi-photon processes involving three or more photons. These sequential pathways can compete with the non-sequential mechanism and enrich the dynamics. Some features of different mechanisms may be reflected in the photoelectron energy spectra (both the joint energy spectra for double ionization and the channel-resolved spectra for single ionization). Therefore we aimed to study the sequential and non-sequential mechanisms by analyzing the photoelectron energy spectra.

5.2 Theory and Main Findings

Our theoretical research is based on the 1D model of helium. As discussed in §2.4, the 1D model allows us to carry out *ab initio* calculations in a wide range of laser parameters. This advantage is particularly beneficial for the numerical simulations of stabilization, since a number of calculations need to be performed at different laser field strengths. We numerically solved the TDSE within the dipole approximation: the wave function was discretized by the FEDVR basis set and the time evolution was performed by the Arnoldi-Lanczos propagator. As introduced in Chapter 4, the photoelectron energy spectra were extracted by applying the tSURFF method (combined with the CAP technique), and then the channel-resolved ionization probabilities were obtained by integrating the corresponding spectra.

Regarding the stabilization question proposed in §5.1, one of the important findings is that there is no obvious stabilization against total ionization happening for the considered laser frequency, but stabilization can occur for a higher laser frequency that is larger than all the ionization potentials. In fact the same conclusion was already drawn by earlier studies (also based on the 1D model calculations) in Ref. [88]. In addition to reminding the readers of this conclusion, our research further investigated how the channel-resolved probabilities vary with the laser field strength. By dividing the total ionization probability into single and double ionization contributions, we discovered the reason for no obvious stabilization observed at the considered laser frequency, i.e., multi-photon double ionization substantially contributes to the total ionization probability for super-intense fields (see Fig. 2 in Paper I). The double ionization contribution can even suppress the single ionization probability at high field strengths, leading to a decreasing trend in the single ionization probability with increasing field strength.

In terms of the channel-resolved probabilities, our calculations confirmed that the ground-state He^+ channel dominates the single ionization at low field strengths.

Also, we found that the probabilities of some excited-state He^+ channels will peak at specific field strengths (see Fig. 3 in Paper I). In view of the fact that these excited-states are odd-wave-function states (in the 1D model), we speculated that this finding could be related to some transitions between the ground state and the excited states dressed by the laser fields. So we resorted to the (lowest-order) HFFT in the KH frame for a view of the dressed energy levels. We found that in the dressed energy picture, there exist some specific field strengths corresponding to one-photon resonances between the ground state and some excited states, and these field strengths agree with the observed peak positions of the excited-state channels (see Fig. 4 in Paper I). Therefore we proposed a sequential “ionization-excitation” mechanism for explaining the observation: the He atom is first singly ionized into the ground-state He^+ channel, and later the He^+ ion is excited to another state when the field strength is able to cause a resonance transition between the dressed ionic states. A time-dependent view of the channel-resolved ionization probabilities to some extent confirmed our proposed mechanism. For a field strength that corresponds to the peak position of an excited-state He^+ channel, we observed in the time domain that the population in the ground-state He^+ channel decreases around the peak of the laser pulse envelope (see Fig. 5 in Paper I). This actually reflects the resonant excitation of the He^+ ion in the dressed energy picture.

Turning to the studies on the photoelectron energy spectra in the XUV regime, we first identified the energy sharing features in the perturbative limit. With the final energy of the two electrons denoted by \mathcal{E}_1 , \mathcal{E}_2 and the ground-state energy of the He atom denoted by E_g , the non-sequential \mathcal{K} -photon double ionization fulfills

$$\mathcal{E}_1 + \mathcal{E}_2 = \mathcal{K}\hbar\omega + E_g, \quad (5.1)$$

which will display as diagonal lines in the joint energy spectra. The sequential multi-photon double ionization can happen via different ionic channels. With the energy of the n -th state He^+ ion denoted by E_n^+ , the sequential \mathcal{K} -photon double ionization (via the n -th ionic channel) fulfills

$$(\mathcal{K} = \mathcal{K}_1 + \mathcal{K}_2) \begin{cases} \mathcal{E}_1 = \mathcal{K}_1\hbar\omega - E_n^+ + E_g, \\ \mathcal{E}_2 = \mathcal{K}_2\hbar\omega + E_n^+, \end{cases} \quad (5.2)$$

which will correspond to some local maxima along the non-sequential diagonal lines in the joint energy spectra.

The two-electron energy sharing relations Eqs. (5.1) and (5.2), which are based on simple energy conservation, however, do not take into account any laser-induced energy shift. In the strong-field regime, a few theoretical studies have shown that the AC Stark effects can lead to new features in the photoelectron energy spectra, such as interference structures [183–186]. The interference structures reported in

the SAE scenario, are explained as the dynamic interference between the photoelectron emitted during the rising and falling edges of the XUV laser pulse [185]. The theoretical research on the dynamic interference effects was recently extended to single ionization of helium for intermediate laser intensities ($\sim 10^{14}$ W/cm²) [187]. As argued in Ref. [186], the observation of interference structures in the photoelectron energy spectra may not be easy and some quantitative conditions should be fulfilled. The spectral peak shifts, nevertheless, are clear signatures of the AC Stark effects and easy to observe in the strong-field regime. Within the 1D model of helium, we investigated the photoelectron energy spectra for high laser intensities ($\sim 10^{16}$ W/cm²) and found that the sequential multi-photon double ionization shows pronounced peak-width spreading in the joint energy spectra (see Fig. 3 in Paper II). Meanwhile, the positions of the non-sequential diagonal lines in the joint energy spectra are not significantly affected. Therefore we considered the peak-width spreading features for the sequential mechanism as signatures of the AC Stark effects in the He⁺ ion.

In order to clearly see sharp spectral peaks, the considered laser pulse in Paper II was chosen to contain 200 cycles in its full width at half maximum. In such a long-pulse case, we would like to apply the Floquet approach for the description of the laser-induced energy shifts (see Sec. III C in Paper II for a brief introduction to the Floquet formalism). Note that diagonalization of the Floquet Hamiltonian allows us to extract the AC Stark shifts, in both the perturbative and non-perturbative regime. For the selected field strengths, we diagonalized the Floquet Hamiltonian of the He⁺ ion^[i], and found that the extracted AC Stark shifts in the ion can successfully explain the peak-width spreading in the spectra. We also performed calculations for some different laser frequencies, and found that the signs of the AC Stark shifts are frequency-dependent and state-specific (see Fig. 6 in Paper II). In the strong-field regime, the Floquet theory indeed offers a way to predict the AC Stark shifts for a long-pulse case.

In terms of the TPDI, only the non-sequential mechanism is allowed by the considered laser frequency. Then we would like to study how important the multi-photon sequential mechanism is, in the strong-field regime. Aiming at answering this question, we investigated the non-sequential TPDI probability as a function of the field strength and compared it with the total double ionization probability. The corresponding analysis is based on two facts: (1) for the \mathcal{K} -photon double ionization in which both the sequential and non-sequential mechanisms are allowed, the sequential mechanism will typically dominate; (2) for the non-sequential mechanism (and also the sequential mechanism), the \mathcal{K} -photon contribution (if allowed) will

^[i]A complex scaling technique was used for easy identification of the bound and continuum states from the quasi-stationary energies, since the complex-scaled continuum states will show prominent decay rates that appear as the imaginary part of the quasi-stationary energies.

much larger than the $(\mathcal{K} + 1)$ -photon contribution. We found that the non-sequential TPDI mechanism dominates the double ionization only at low field strengths (see Fig. 4 in Paper II). As the field strength increases, the portion of the non-sequential TPDI probability in the total double ionization decreases dramatically, which implies that the sequential multi-photon mechanism substantially contributes to the double ionization in the strong-field regime. This finding is actually a result of the competition between the different multi-photon processes, and the same conclusion can qualitatively be predicted by simple rate equations (see the comparison between Fig. 4 and Fig. 5 in Paper II).

5.3 Concluding Remarks

In summary, our studies on the strong-field ionization of model helium in the XUV regime considered several laser frequencies that allow the non-sequential TPDI but not the sequential TPDI. We first found that no obvious stabilization against total ionization will occur in the considered frequency regime, as a result of large multi-photon double ionization probability in the strong-field regime. This indicates that for multi-electron systems, the high-frequency stabilization condition ($\hbar\omega > I_p$) should not be understood with respect to only single ionization (from inner or outer shells). Recently it was reported that for the simplest molecular system H_2^+ , highly non-resonant dissociation can dominate over ionization in the stabilization regime [188]. In connection with the dissociation mechanism proposed in Ref. [188], our research implies that the phenomenon may not be observed for multi-electron molecules, if the laser frequency is not high enough to overcome all the ionization potentials.

The laser-induced energy-level shifting is a common topic in both Paper I and Paper II. On the one hand, the field-strength dependence of the energy shifts can cause resonant transitions between the ionic states in dressed energy picture, and such dynamics are reflected in the channel-resolved ionization probabilities. On the other hand, we can read the energy shifts of different ionic states from the joint energy spectra for double ionization, since the peak structures (corresponding to the sequential mechanism) show pronounced width spreading in the strong-field regime. In the long-pulse limit, the Floquet theory can well describe the laser-induced energy shifts, i.e., the AC Stark effects, in the strong-field regime. Also, a high-frequency version of the Floquet theory in the KH frame, the lowest-order HFFT can provide rough estimates of the energy shifts.

Since no obvious stabilization against total ionization happens in the considered frequency regime, there exists some competition between different mechanisms. In the strong-field scenario, the double ionization will contribute a majority of the

total ionization probability, and the sequential multi-photon double ionization will dominate over the non-sequential mechanism.

In view of the recent development in free-electron laser (FEL) technology [189–191], experimental studies in the strong-field XUV regime are expected to be feasible in the near future.

Ionization of Helium in the NIR Regime

In this chapter we will give an overview of our published paper [93], in which the strong-field ionization of model helium in the near-infrared (NIR) regime was discussed. A copy of this paper is provided in **Part Two** of this thesis (Paper III).

6.1 Motivation

In fact, the studies in the NIR regime have dominated the strong-field physics for a long time, since the table-top titanium-sapphire laser operating at ~ 800 nm is the mainstream workhorse for the strong-field experiments. As introduced in §1.1, the dynamics in the long-wavelength regime can usually be understood from a quasi-static perspective, which leads to well-established concepts such as the three-step model [32].

Recent development of ultrafast laser sources with longer wavelengths, e.g., in the mid-infrared (MIR)^[i] regime, opens new possibilities for the strong-field physics [192]. The strong-field physics in the long-wavelength regime is considered to have promising advantages in several aspects: (1) it can provide better understanding in the quasi-static picture and the related concepts [34, 193]; (2) it offers an approach to create high-energy photons and ultrashort laser pulses [194, 195]; (3) it can produce high-energy (rescattered) electrons for imaging ultrafast molecular dynamics, with femtosecond and sub-Ångström resolution [196–198].

Meanwhile, the long-wavelength laser interactions make the corresponding *ab initio* calculations quite difficult, proposing challenges to the theoretical studies in the long-wavelength regime. As mentioned in §2.4, it is indeed a formidable task to simulate multi-electron dynamics based on the TDSE in the long-wavelength regime. Therefore it is natural to ask a question: what theoretical methods other than the full TDSE simulations are useful for investigating the long-wavelength laser interactions with multi-electron systems? In order to discuss this question, we considered the 1D model of helium as a practical testbed for examining some

^[i]There are different schemes for the infrared sub-division. Here we follow the ISO 20473 scheme, which defines the NIR as wavelengths from 780 to 3000 nm and the MIR as wavelengths from 3000 to 50000 nm, respectively.

theoretical approaches. Within the 1D two-active-electron model, we are able to perform the corresponding TDSE calculations in the long-wavelength regime. Regarding the strong-field phenomena, we would like to focus on the high-order ATI processes and compute the channel-resolved photoelectron spectra as references for comparison.

6.2 Theory and Main Findings

The numerical methods used in the NIR regime are basically similar to those used in the XUV regime, i.e., we discretized the wave function with the FEDVR basis set, performed the time evolution with the Arnoldi-Lanczos propagator, and extracted the photoelectron energy spectra with the tSURFF method. But the employed absorbing boundary conditions are different for the XUV and the NIR frequency regimes: instead of the CAP added to the time-dependent Hamiltonian, we used the irECS technique for the NIR simulations (see §3.4 for details of the irECS method and implementation, and Figure 3.4 for an example of the irECS performance). In Paper III, we considered the laser wavelengths of 800 nm, 1600 nm and 2400 nm, and restricted to only two-cycle pulses for shortening the simulation time.

As mentioned in §1.1, many strong-field phenomena are described within the SAE picture. In fact, the SAE model has already been applied in modeling multi-electron systems irradiated by intense laser fields (see, e.g., Refs. [199–201]). The validity of the SAE approximation in multi-electron systems, however, still remains not fully studied. As discussed in §2.4, so far the full-dimensional TDSE simulations in the long-wavelength (> 800 nm) regime can only be performed within the SAE approximation, which means that there is no rigorous verification available. Nevertheless, we could investigate the validity of the SAE approximation within the 1D model, by means of a straightforward comparison of the corresponding *ab initio* calculation results.

Within the SAE approximation, one needs to find an effective potential for the active electron that responds to the laser fields. For the ground-state He atom, we can find the effective potential in a self-consistent way by making the Hartree-Fock ansatz (see Sec. II B in Paper III or Ref. [202] for details). This approach assumes that the bound electron remains “frozen” (inactive) during the SAE dynamics, and produces an ionization potential I_p slightly smaller than that for single ionization of the two-active-electron model.

In terms of the calculated observables, the ATI spectra for the SAE model should be compared with the ATI spectra for single ionization of the two-active-electron model. We extracted the ATI spectra in different He⁺ channels and found that the total single ionization can be approximately represented by the single ionization

in the ground-state He^+ channel. For a laser intensity of $8 \times 10^{13} \text{ W/cm}^2$, there exists a large disagreement between the SAE and the ground-state He^+ channel ATI spectra for the wavelength of 800 nm, and the disagreement becomes smaller as the wavelength increases to 1600 nm and 2400 nm (see Fig. 1 in Paper III). Thus we concluded that the SAE approximation performs better at longer wavelengths for a fixed laser intensity.

Actually the above conclusion is only one perspective on the validity of the SAE approximation. In addition, we examined the SAE approximation from a different perspective by varying the intensity with the wavelength, keeping the ponderomotive potential U_p and the Keldysh parameter γ fixed. For a large U_p (and a small γ , in the tunneling ionization regime), we found good agreement between the SAE and the ground-state He^+ channel spectra, especially for the high-energy part near the ATI cutoff (see Fig. 2 in Paper III). This implies that the SAE approximation is applicable for describing the high-order ATI spectra, as long as the ponderomotive energy is large and the Keldysh parameter is small, i.e., in the tunneling ionization regime.

Besides, we found that the channel-resolved ATI spectra have different cutoffs. Although the spectral intensities in the excited-state He^+ channels are generally much lower than that in the ground-state He^+ channel, the different spectral cutoffs are indeed signatures of two-electron dynamics, which cannot be described within the SAE approximation. Then we resorted to another commonly-used theoretical approach: the SFA. As a theoretical method that does not rely on the TDSE simulations, the SFA and its modified versions have been extensively used for studying both one-electron [203–207] and two-electron [208–213] dynamics. In contrast to the extensive applications for double ionization, we applied the SFA for the channel-resolved single ionization.

Following the basic idea of the IMST [63], we formulated the two-electron SFA including rescattering processes (see Sec. II C in Paper III for details). The IMST can provide a systematic analysis of the transition amplitude from an initial state to a final state. In our case, the initial state is the ground state of the He model denoted by $\Psi_g(x_1, x_2, t)$, and the final state is the single-continuum state approximated by a (symmetrized) product of the Volkov state and the bound ionic state^[iii]

$$\Psi_{k_F, n}(x_1, x_2, t) = \frac{1}{\sqrt{2}} \left[\chi_{k_F}(x_1, t) \psi_n(x_2, t) + \chi_{k_F}(x_2, t) \psi_n(x_1, t) \right], \quad (6.1)$$

which means that the freed electron has the final momentum k_F and the He^+ ion is in its n -th state. Since we focused on the cutoffs of the high-order ATI spectra, we

^[iii]Here the electron exchange symmetry is explicitly considered.

restricted to the rescattering terms of the form

$$T_{m \rightarrow n} = - \int_{t_1}^{+\infty} dt_2 \int_{-\infty}^{+\infty} dt_1 \int_{-\infty}^{+\infty} dk_I \langle \Psi_{k_F, n}(t_2) | V_R | \Psi_{k_I, m}(t_2) \rangle \\ \times \langle \Psi_{k_I, m}(t_1) | V_I(t_1) | \Psi_g(t_1) \rangle, \quad (6.2)$$

where $\Psi_{k_I, m}(x_1, x_2, t)$ corresponds to an intermediate single-continuum state, $V_I(t_1)$ is the time-dependent laser interaction and V_R is the time-independent rescattering potential. With the ground-state He energy denoted by E_g and the n -th (m -th) He⁺ energy denoted by E_n^+ (E_m^+), we can introduce the two-electron Volkov phase^[iii]

$$S_{m \rightarrow n} = \int_0^{t_2} dt \frac{[k_F + A(t)]^2}{2} - \int_{t_1}^{t_2} dt \frac{[k_I + A(t)]^2}{2} + (E_n^+ - E_m^+) t_2 + (E_m^+ - E_g) t_1, \quad (6.3)$$

and the corresponding form factor

$$W_{m \rightarrow n} = \left[\langle \Psi_{k_F, n}(t) | V_R | \Psi_{k_I, m}(t) \rangle \langle \Psi_{k_I, m}(t) | V_I(t_1) | \Psi_g(t) \rangle \right] \Big|_{t=0}. \quad (6.4)$$

Then the transition amplitude Eq. (6.2) can be rewritten as

$$T_{m \rightarrow n} = - \int_{t_1}^{+\infty} dt_2 \int_{-\infty}^{+\infty} dt_1 \int_{-\infty}^{+\infty} dk_I [W_{m \rightarrow n} \exp(iS_{m \rightarrow n})], \quad (6.5)$$

and can be evaluated with the saddle-point method (SPM) [203–206].

The corresponding saddle-point equations are

$$k_I(t_2 - t_1) + \int_{t_1}^{t_2} dt A(t) = 0, \quad (6.6)$$

$$\frac{[k_I + A(t_1)]^2}{2} + (E_m^+ - E_g) = 0, \quad (6.7)$$

$$\frac{[k_F + A(t_2)]^2}{2} - \frac{[k_I + A(t_2)]^2}{2} + (E_n^+ - E_m^+) = 0, \quad (6.8)$$

which determine the intermediate momentum k_I , and describe the energy conservation relations at the ionization time t_1 and the rescattering time t_2 . The saddle-point solutions are complex-valued and they come in pairs [203–206]. Note that for the multi-dimensional integral Eq. (6.5), it is not trivial to rigorously analyze all the saddle-point solutions. For our purpose of investigating the high-order ATI cutoffs, fortunately, we only need to find the solution pairs that determine the cutoffs.

^[iii]We suppose that the laser-pulse interaction starts from time $t = 0$.

In fact, according to the SPM, the ATI cutoffs are solely determined by the phase $S_{m \rightarrow n}$: at a cutoff k_F , the complex-valued phase $S_{m \rightarrow n}$ has the same real part for the pair of saddle-point solutions [204].

In terms of the energy exchange between the freed electron and the ion, the rescattering processes in the two-active-electron model can be classified into two types: elastic ($\mathbf{n} = \mathbf{m}$) and inelastic ($\mathbf{n} \neq \mathbf{m}$). In practice, we considered the fact that the single-ionization into the \mathbf{m} -th channel is exponentially sensitive to the corresponding ionization potential ($E_m^+ - E_g$). Therefore the ground-state He^+ channel ($\mathbf{m} = 1$) is the most probable for the tunneling step, which allows us to analyze the channel-resolved ATI cutoffs with the terms $T_{1 \rightarrow \mathbf{n}}$. By applying the SPM analysis, we found that the different cutoff positions of the channel-resolved ATI spectra can be well explained by the elastic and inelastic rescattering mechanisms (see Fig. 3 and Fig. 4 in Paper III for the saddle-point solutions and the corresponding spectral cutoffs). Note that the ATI cutoff-energy differences are not the same as the energy differences between the ionic states, since the vector potential $A(t)$ is involved in the energy conservation at the rescattering time [Eq. (6.8)].

6.3 Concluding Remarks

In the NIR regime, we used the 1D model helium as a testbed for examining two commonly-used theoretical tools: the SAE model and the SFA analysis. The high-order ATI spectra in different single ionization channels, which were extracted from the two-electron TDSE simulations, served as references for comparison.

The SAE approximation was found to be applicable for describing the high-order ATI spectra in the tunneling ionization regime, which is characterized by a large ponderomotive energy and a small Keldysh parameter. Since the SAE model has been usually applied in modeling the strong-field phenomena, it is important to examine its validity by means of *ab initio* calculations. For example, the LIED technique for ultrafast imaging, as mentioned in §1.1, is actually based on the SAE picture. Our examination of the SAE approximation, although within the 1D model, to some extent validates the SAE model used in the theoretical analysis of the LIED technique, especially in the long-wavelength regime.

The high-order ATI spectra corresponding to the excited-state He^+ channels show different cutoffs, which are signatures of two-electron dynamics beyond the SAE picture. The mechanisms for the channel-resolved ATI cutoffs were studied with the two-electron SFA including rescattering. By performing the SPM analysis of the SFA rescattering terms, we related the channel-resolved ATI cutoffs to the elastic and inelastic rescattering processes. Therefore the two-electron SFA and the SPM analysis are useful for qualitative studies of the strong-field ionization in the

long-wavelength regime.

As mentioned in §1.1, there have been some theoretical efforts to improve the SFA approach by including Coulomb corrections (see, e.g., Refs. [19, 20, 22, 23, 25–27]). So we expect that the improved SFA approach could probably provide more insights into the strong-field dynamics.

Summary and Outlook

This thesis primarily discusses some theoretical research on the strong-field ionization of two-electron model atoms, which is a typical example of multi-electron dynamics. The investigated processes include single ionization with different ionic states and double ionization.

The theoretical studies basically rely on numerical simulations of the TDSE. The general TDSE approach for describing the strong-field laser interactions with multi-electron atoms was discussed in Chapter 2. Also, in Chapter 2 we reviewed some applications of reduced-dimensional models for the theoretical research on strong-field phenomena. In the two-active-electron case, the full-dimensional TDSE simulations are computationally demanding, especially for long-wavelength laser interactions. So we chose to work within the 1D models, which can still provide some insights into the two-electron problems in the strong-field regime.

In pursuit of accurate and efficient TDSE simulations, we implemented some well-performed numerical methods. The applied numerical schemes, including the FEDVR discretization, the Arnoldi-Lanczos time propagator, and several absorbers (CAP/ECS/irECS), were detailed in Chapter 3. For the investigations of the strong-field ionization, continuum observables are of interest. In our work, the tSURFF method was applied to extract the photoelectron spectra from the TDSE calculations. We gave a systematic description of the tSURFF method for both one-electron and two-electron cases in Chapter 4. It should be emphasized that the tSURFF method combined with efficient absorbers (e.g., the irECS technique) allows us to extract the continuum information with a small simulation volume, which is the key advantage of our computational methods.

By using the above-mentioned efficient numerical methods, we are able to study the strong-field ionization of two-electron model atoms in a wide range of laser parameters, ranging from the XUV regime to the NIR regime. With these studies we published three papers, which were attached in **Part Two** of this thesis. We gave an overview of our work in the XUV regime and the NIR regime in Chapter 5 and Chapter 6, respectively. All these studies were to some extent motivated by recent development in laser technology, which enables the production of intense laser pulses with wide-range frequencies (from terahertz to X-ray).

In the studies on strong-field ionization of model helium in the XUV regime, we first revisited the concept of high-frequency stabilization for two-electron atoms. For the considered photon energy that is only higher than the lowest single ionization potential, no evident stabilization effect was observed, because double ionization contributes a majority of total ionization probability at high laser intensities. More information about the strong-field dynamics was provided by a detailed view of the channel-resolved ionization probabilities. For intense laser interactions, the field-dressed energy-level shifting is an important effect. From the field-strength dependence of the channel-resolved ionization probabilities, we identified some resonant transitions between the ionic states in dressed energy picture. Also, the energy shifts of different ionic states can be read from the joint energy spectra for double ionization, since the sequential peak structures show pronounced width spreading. For the description of the laser-induced energy shifts in the strong-field regime, we applied the Floquet theory (and also the high-frequency version HFFT in the KH frame) in our analysis. The Floquet theory can indeed predict non-perturbative field-dressed energy shifts for long-pulse laser interactions.

Turning to the studies on strong-field ionization of model helium in the NIR regime, we first examined the SAE approximation for the high-order ATI of the 1D two-electron model. For the long-wavelength laser interactions, it is rather difficult to examine the validity of the SAE model by performing full-dimensional TDSE calculations of a multi-electron system for comparison. With the 1D two-electron model and the efficient numerical methods, however, we could investigate the SAE performance by means of *ab initio* calculations in the long-wavelength regime. We found that the SAE approximation is applicable for describing the high-order ATI spectra in the tunneling regime, which is characterized by a large ponderomotive energy and a small Keldysh parameter. This finding to some extent validates the commonly-used SAE model for the theoretical analysis of strong-field phenomena, especially in the long-wavelength regime. We also found that the high-order ATI spectra in the excited-state ionic channels show different cutoffs, which are clear signatures of two-electron dynamics beyond the SAE picture. By performing the SPM analysis of the two-electron SFA rescattering terms, we related the channel-resolved ATI cutoffs to the elastic and inelastic rescattering processes. Therefore the SFA and the SPM are indeed useful for qualitative studies of strong-field ionization (including the two-electron dynamics).

In fact, the coupling between different single ionization channels is a common research interest of our studies in both the XUV and the NIR regimes. In the XUV regime, the different single ionization channels are mainly coupled by the laser fields (photons). For example, one-photon resonant transitions between the field-dressed ionic states may occur. In the NIR regime, where the rescattering picture is valid, the coupling between different ionic states can also be induced by the electron

via inelastic rescattering processes. In both cases, the coupling features are of non-perturbative nature, i.e., strong-field phenomena.

One possible extension of our work is to investigate the 1D two-electron model irradiated by a combination of the XUV and the NIR laser pulses. Such a pump-probe scheme may allow us to learn more about ultrafast electron dynamics, e.g., in the attosecond time scale. There might also be some new phenomena for such two-color laser interactions. Recently a theoretical paper [148] reported an inelastic rescattering process in single ionization of helium: the XUV pulse induces single ionization in the excited ionic channel; then the freed electron is driven back by the NIR pulse, rescatters and de-excites the ion to the ground state. In Ref. [148], a large simulation volume was used for calculating the momentum distribution of the freed electron. We expect that this inelastic rescattering mechanism can be demonstrated by applying the tSURFF method to extract the channel-resolved photoelectron spectra, which will require much less computational cost.

To study the correlated electron dynamics in general multi-electron systems, one may resort to some time-dependent many-electron approaches that are developed on the basis of the Slater determinant (see, e.g., Ref. [214] for a review). Several examples are the multi-configuration time-dependent Hartree-Fock (MCTDHF) method [162, 163, 215, 216], the time-dependent configuration-interaction singles (TDCIS) method [217, 218], the time-dependent restricted-active-space self-consistent-field (TD-RASSCF) method [164, 165, 219], and the time-dependent generalized-active-space configuration-interaction (TD-GASCI) method [166, 167]. For such many-electron approaches, the performance can possibly be improved by implementing accurate and efficient numerical schemes such as the tSURFF method and the irECS absorber. Actually, the tSURFF was implemented in the TDCIS method [218] and was found to perform quite well with a good absorber. A former member of our group, Lun Yue, made a preliminary demonstration that the tSURFF can possibly be applied in the TD-GASCI approach (for single ionization). Attempts to implement the tSURFF method and the irECS absorber in the above-mentioned many-electron schemes, in my opinion, will be meaningful work for the future.

PART TWO
PUBLICATIONS

Paper I. Physical Review A 93, 043412 (2016)

Title:

**Ionization of helium by intense XUV laser pulses:
Numerical simulations on channel-resolved probabilities**

Authors: Chuan Yu and Lars Bojer Madsen

DOI: <https://doi.org/10.1103/PhysRevA.93.043412>

Reprinted with permission from the American Physical Society.
Copyright (2016) by the American Physical Society.

My contribution to this publication includes (1) implementation of the theoretical calculations and (2) preparation of the manuscript (with figures).

PHYSICAL REVIEW A 93, 043412 (2016)

Ionization of helium by intense XUV laser pulses: Numerical simulations on channel-resolved probabilities

Chuan Yu and Lars Bojer Madsen

Department of Physics and Astronomy, Aarhus University, DK-8000 Aarhus C, Denmark

(Received 8 March 2016; published 14 April 2016)

Ionization of a helium atom by intense extreme ultraviolet laser pulses is investigated in a frequency regime where the high-frequency stabilization condition is only fulfilled for the lowest single ionization channel. Multiphoton double ionization substantially contributes to the total ionization probability for superintense fields. As a result, no obvious stabilization against total ionization occurs. A detailed view of probabilities into different single ionization channels as a function of the field strength is presented. We find that the probabilities into some ionic channels peak at field strengths corresponding to one-photon resonances between field-dressed ionic states in the high-frequency Floquet theory. Thus we propose a sequential “ionization-excitation” mechanism in the dressed energy picture: first, one-photon absorption causes single ionization, leaving the ion in its dressed ground state; second, the ion is excited to a new state via one-photon absorption at the field strength where the resonance condition in the dressed ionic system is fulfilled. To reveal the sequential mechanism in the time domain, we also take a time-dependent view on the channel-resolved probabilities, observing the decrease of the ground-state ionic channel probability during the laser pulse when the field strength is such that a resonance condition exists between the dressed states in the ion.

DOI: [10.1103/PhysRevA.93.043412](https://doi.org/10.1103/PhysRevA.93.043412)

I. INTRODUCTION

Strong-field ionization of atoms has been the subject of extensive theoretical and experimental investigations over decades. Developments of new light sources and focusing techniques have enabled the production of laser pulses with unprecedented high intensity. Nowadays, extreme-ultraviolet (XUV) laser pulses with femto- or subfemtosecond durations can be generated from high-order harmonics [1,2] or free electron lasers [3,4]. Such ultrashort laser pulses provide the opportunity of monitoring matter on ultrafast time scales [5–7]. Besides, new dynamics and phenomena may be induced by the extremely intense fields.

Stabilization, i.e., a decreasing trend of ionization yield with increasing laser intensity, is one of the well-known nonperturbative phenomena in strong-field ionization. It was theoretically discovered for high-frequency laser fields [8,9] and some experimental observations were reported for Rydberg atoms [10–14]. One reason for choosing Rydberg atoms as experimental targets is that the high-frequency condition can be more easily fulfilled for Rydberg atoms than for ground-state atoms. To observe stabilization, the high-frequency condition requires a single photon to have sufficient energy to ionize the atom, which for intense laser fields is defined as the stabilization regime [10]. There have been a number of theoretical studies on stabilization of one-electron systems (see review articles [15,16]). Comparatively, studies on stabilization of multielectron systems are still rare, and the research targets are mainly restricted to two-electron systems. For example, research on two-electron atoms in strong fields with the high-frequency Floquet theory (HFFT) concluded that stabilization occurs for two-electron atoms as well [17]. With a one-dimensional (1D) model of helium, the effect of electron correlation in stabilization was investigated in Ref. [18]. *Ab initio* calculations of three-dimensional (3D) helium in superintense XUV fields were reported in Refs. [19,20] and stabilization of the two-electron atom was observed in the numerical experiments.

Recently a theoretical study [21], focusing on laser-induced dynamics of the simplest molecule H_2^+ in the XUV regime, reported that highly nonresonant dissociation can dominate over ionization when stabilization occurs. Reference [21] also briefly discussed the possible extension of the mechanism to other molecules. In contrast to single-electron systems like H_2^+ , the existence of electron correlation in multielectron systems increases the complexity of laser-induced dynamics and causes great interest in revealing its roles in strong-field phenomena [22–24]. In the stabilization regime, theoretical studies for two-electron atoms have indicated that electron correlation can suppress the stabilization effect [18–20]. This conclusion is reached by comparing the total ionization (TI) probabilities obtained from calculations including electron correlation with those obtained from independent-electron model calculations. For a two-electron system, TI means the sum of single ionization (SI) and double ionization (DI), and SI contains contributions from many ionic channels, i.e., the ion can be left in the ground state or some excited states. As a consequence, a two-electron system has multiple ionization energies, i.e., it has SI thresholds in different ionic channels and a DI threshold. One may consider a photon energy that is only larger than the lowest ionization energy. In this case only one channel is in the stabilization regime, while multiphoton ionization into other channels is possible. The frequency regime considered in this work is illustrated in Fig. 1 with some energy levels of He. The physics discussed is similar to that for multielectron molecular systems, e.g., H_2 . Previous studies of stabilization in two-electron atoms [18–20] focused on TI, SI, and DI probabilities. To our knowledge, there has been no detailed view on ionization probabilities of different ionic channels under such strong-field conditions. In this work we take a look at the probabilities of reaching different ionic channels when a helium atom is ionized by an intense XUV laser pulse, and show that channel-resolved probabilities provide more information about strong-field ionization. On the basis of the field-dressed energy levels in the HFFT [15,25],

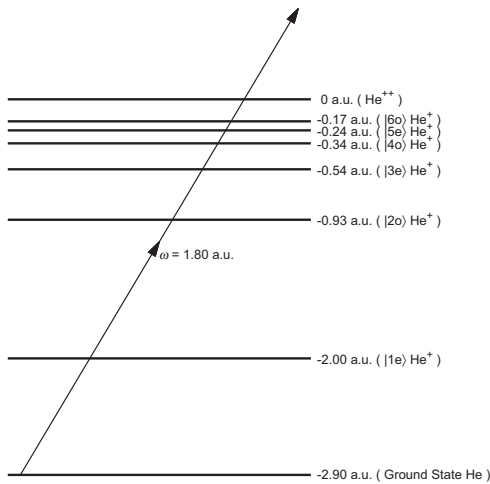


FIG. 1. Laser frequency regime considered in this work, illustrated with some energy levels of a 1D model of helium (see the text in Sec. II). The stabilization condition is fulfilled for the ground-state ionic channel labeled as $|1e\rangle \text{He}^+$, but not for the rest of the channels.

we identify an “ionization-excitation” sequential mechanism in the considered frequency regime.

This paper is organized as follows. In Sec. II we introduce the theoretical and numerical methods used in this work. In Sec. III we present and discuss the results of the calculations. Finally we give concluding remarks in Sec. IV. Atomic units are used throughout.

II. THEORETICAL MODEL AND METHODS

We consider a 1D model of helium in the presence of a linearly polarized laser pulse, in which the two electrons are allowed to move along the direction of the laser polarization. This 1D model reduces computational difficulty, and allows us to perform calculations for a wide range of laser parameters, which is essential for the questions addressed in this work. We numerically solve the time-dependent Schrödinger equation (TDSE)

$$i\partial_t\Psi(x_1, x_2, t) = \hat{H}(t)\Psi(x_1, x_2, t), \quad (1)$$

with the Hamiltonian

$$\hat{H}(t) = \sum_{j=1}^2 \left[\frac{\hat{p}_j^2}{2} + A(t)\hat{p}_j + V_{\text{en}}(x_j) \right] + V_{\text{ee}}(x_1, x_2). \quad (2)$$

Here x_j and $\hat{p}_j = -i\partial_{x_j}$ ($j = 1, 2$) are the electron coordinates and momenta, respectively, and

$$V_{\text{en}}(x_j) = \frac{-2}{\sqrt{x_j^2 + a_{\text{en}}}} \quad (j = 1, 2), \quad (3)$$

$$V_{\text{ee}}(x_1, x_2) = \frac{1}{\sqrt{(x_1 - x_2)^2 + a_{\text{ee}}}} \quad (4)$$

are the electron-nuclei interaction and the electron-electron interaction, where a_{en} and a_{ee} are softening parameters used to avoid the Coulomb singularity. The laser interaction is described in velocity gauge by the vector potential $A(t)$ within dipole approximation, and a time-dependent energy shift from the $A^2(t)$ term in the Hamiltonian has been unitarily transformed away. In our calculations, a vector potential with a Gaussian envelope is used:

$$A(t) = \frac{F_0}{\omega} \exp\left(-4 \ln 2 \frac{t^2}{\tau^2}\right) \sin(\omega t), \quad (5)$$

where F_0 is the maximum field strength related to the peak intensity by $I = F_0^2$, ω is the angular frequency, and τ is the full width at half maximum (FWHM) of the envelope. The pulse duration is described by the number of cycles within τ , $N_c = \omega\tau/(2\pi)$.

We express the Hamiltonian and the wave function in a finite-element discrete variable representation (FEDVR) [26,27] basis set, and solve the TDSE with the Arnoldi-Lanczos time propagator [28,29]. The initial wave function is obtained by imaginary time propagation [30]. By choosing softening parameters $a_{\text{en}} = 0.50$ and $a_{\text{ee}} = 0.33$, we obtain the He ground-state energy -2.90 and He^+ ionic ground-state energy -2.00 , which are both good approximations to the values for the 3D systems.

The time-dependent surface flux (t-SURFF) method [31,32] allows one to extract photoelectron spectra (PES) by monitoring electron flux through some surfaces (see also Ref. [33] for an extension of the t-SURFF method to the molecular case and Refs. [34,35] for other recent applications). So the PES is calculated with good accuracy, and at the same time the outgoing flux is absorbed to avoid unphysical reflections at the boundaries of the simulation box. The advantage of the t-SURFF method is that we can obtain the PES with a relatively small simulation box. In our work, a complex absorbing potential (CAP) [36]

$$V_{\text{CAP}}(x_1, x_2) = -i[f_{\text{CAP}}(x_1) + f_{\text{CAP}}(x_2)] \quad (6)$$

is added to the Hamiltonian in real time propagation, where $f_{\text{CAP}}(x)$ is a function of the form

$$f_{\text{CAP}}(x) = \begin{cases} 1 - \cos\left[\frac{\pi(|x| - r_c)}{2(r_{\text{max}} - r_c)}\right], & r_c < |x| < r_{\text{max}}, \\ 0, & |x| \leq r_c. \end{cases} \quad (7)$$

We set up a simulation box $r_{\text{max}} = 120$ with 120 equal-size finite elements and 9 DVR basis functions in each element. The t-SURFF surfaces are placed at $|x_1|, |x_2| = 60$ and the CAP radius is $r_c = 65$. In real time propagation, we use a time step of $\Delta t = 0.005$. The convergence is checked with computations using a larger box ($r_{\text{max}} = 150$ with 150 finite elements, the t-SURFF surfaces placed at $|x_1|, |x_2| = 80$, and the CAP radius $r_c = 85$).

For SI, the PES $S_{\text{SI},c}(E_1)$ describes the probability in which one electron is freed with energy E_1 and the ion is in state c (SI channel c). The eigenstates of He^+ , which are essential for calculating $S_{\text{SI},c}(E_1)$, are obtained by diagonalizing the ionic Hamiltonian in the FEDVR basis. For DI, the PES $S_{\text{DI}}(E_1, E_2)$ describes the probability in which two electrons are freed with energy E_1 and E_2 . A detailed discussion of the t-SURFF method used for calculating $S_{\text{SI},c}(E_1)$ and $S_{\text{DI}}(E_1, E_2)$ can be

found in Ref. [32]. With the PES $S_{\text{SI},c}(E_1)$ and $S_{\text{DI}}(E_1, E_2)$, the probabilities for SI channel c and DI are readily obtained,

$$P_{\text{SI},c} = \int S_{\text{SI},c}(E_1) dE_1, \quad (8)$$

$$P_{\text{DI}} = \iint S_{\text{DI}}(E_1, E_2) dE_1 dE_2. \quad (9)$$

Since the outgoing flux is absorbed by the CAP, we describe the total ionization probability as

$$P_{\text{TI}} = 1 - \iint_{|x_1|, |x_2| \leq 60} |\Psi(x_1, x_2, t \rightarrow \infty)|^2 dx_1 dx_2, \quad (10)$$

where the integral is restricted to the inner region defined by the t-SURFF surfaces. The inner region should be much larger than the amplitude of the electron quiver motion, which is essential for the theoretical methods used in this work. Notice that the largest quiver radius $\alpha_0 = F_0/\omega^2$ in our calculations is ≈ 3 , which is much smaller than the extent of the inner region.

Due to the 1D model used here, a given electronic state wave function can be classified as even or odd. For the ion He^+ , we use the notations $|1e\rangle, |2o\rangle, |3e\rangle, |4o\rangle, \dots$, for the ground state and the excited states. These notations are also used later for dressed energy levels [see Eq. (15) in Sec. III]. The eigenstates of the dressed He^+ are also obtained by diagonalizing the corresponding Hamiltonian in the FEDVR basis.

III. RESULTS AND DISCUSSION

Figure 2 shows SI, DI, and TI probabilities versus field strength F_0 , for fixed $\omega = 1.80$ and $N_c = 20$. The TI and DI probabilities are calculated with Eqs. (10) and (9), respectively; and then the SI probability is obtained by $P_{\text{SI}} = P_{\text{TI}} - P_{\text{DI}}$. In the considered frequency regime, only the $|1e\rangle$ He^+ channel is open by one-photon absorption, while two-photon absorption can open all the SI channels and the DI channel, as shown in

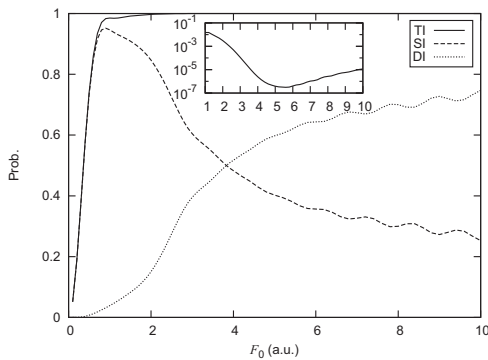


FIG. 2. SI (dashed line), DI (dotted line), and TI (solid line) probabilities of ground-state helium vs field strength F_0 , for a 20-cycle pulse with $\omega = 1.80$. Inset: log-scale plot of bound probability $(1 - P_{\text{TI}})$ for field strengths $1.0 \leq F_0 \leq 10.0$, with its minimum corresponding to the maximum TI probability.

Fig. 1. The behavior of these probabilities can be roughly classified into three regimes. First, for low field strengths ($F_0 < 1.0$), P_{TI} increases dramatically with F_0 and the main contribution is from SI. At $F_0 = 1.0$, P_{TI} is quite high (> 0.9). Second, with increasing field strength $1.0 < F_0 < 5.5$, DI starts to contribute and P_{SI} decreases. There is also a small increase in P_{TI} (see the inset of Fig. 2). Third, for very strong fields ($F_0 > 5.5$), both SI and DI probabilities vary slowly with F_0 and show a small oscillating behavior. The oscillating behavior in the ionization probability was reported and discussed for one-electron models [37,38], and is not the focus of the present work. From the inset of Fig. 2, one finds a slight decreasing trend in P_{TI} in this very high field-strength regime.

Considering the laser frequency $\omega = 1.80$, there exists a decreasing trend in the SI probability with increasing field strength. However, the DI probability increases with increasing field strength, indicating that the atom is not actually stabilized. In extremely intense fields, one finds that multiphoton DI contributes substantially, leading to very high TI probabilities. This means that the coexistence of one-photon ionization of the lowest channel, which is in the stabilization regime, and multiphoton ionization into other channels results in no obvious stabilization against TI. So the mechanism of dissociation proposed in Ref. [21] may not be observed for multielectron molecules in the laser frequency regime considered here. In Ref. [18], it was also concluded that stabilization would not be achieved in such an intermediate frequency regime and that the slight decreasing trend in the TI probability should not be seen as real stabilization. Our results, however, can provide more information about the ionization in different channels (see also the later discussion). In addition, we have performed calculations for 20-cycle laser pulses with frequency $\omega = 4.00$, which is above the DI threshold. Our results for $\omega = 4.00$ (not shown) are similar to those obtained from numerical simulations of 3D He [19], i.e., stabilization against TI is clearly observed. This conclusion agrees with Ref. [18] as well. It implies that the mechanism of dissociation proposed in Ref. [21] may be observed for multielectron molecules, if the laser frequency is high enough to cause substantial stabilization in all the ionization channels.

In Fig. 3(a) we take a detailed view on the lowest eight SI channels contributing to the dashed curve in Fig. 2. For comparison, we perform calculations for a 20-cycle pulse with a lower frequency $\omega = 1.70$, and present the results in Fig. 3(b). As seen from Figs. 3(a) and 3(b), the lowest eight SI channels comprise the majority of the SI probability ($> 67\%$ over the considered field strength range) and show some representative behaviors. In both Figs. 3(a) and 3(b), we find that all the even-wave-function channels, except the $|1e\rangle$ He^+ channel, contribute little to the SI probability over the considered field strength range. For low field strengths, the $|1e\rangle$ He^+ channel dominates the SI probability (compare $P_{\text{SI},|1e\rangle}$ with P_{SI} in Fig. 3). In Fig. 3(a), $P_{\text{SI},|1e\rangle}$ increases with the field strength up to $F_0 = 0.5$; after that it shows some oscillations and an overall decreasing trend. In Fig. 3(a), one can also find interesting peaks of $P_{\text{SI},|6o\rangle}$ and $P_{\text{SI},|8o\rangle}$ at $F_0 = 1.1$ and $F_0 = 1.8$, respectively. For $\omega = 1.70$, similar peaks of $P_{\text{SI},|4o\rangle}$, $P_{\text{SI},|6o\rangle}$, and $P_{\text{SI},|8o\rangle}$ appear in Fig. 3(b). There is a common feature that these channels are odd-wave-function

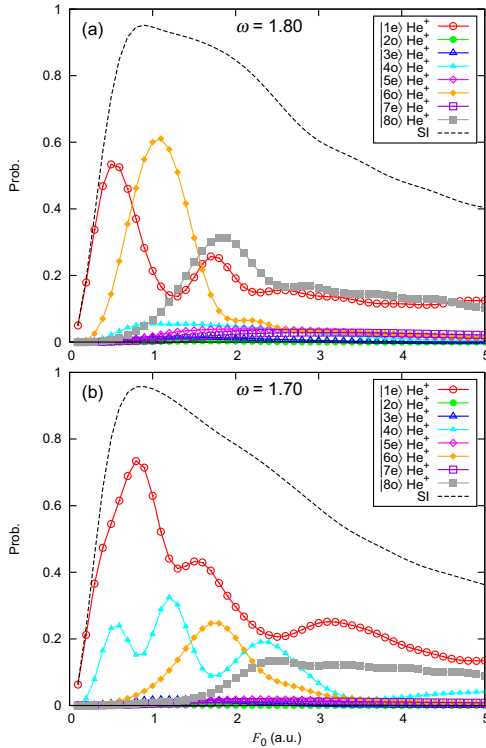


FIG. 3. (a) Probabilities of the lowest eight SI channels (solid lines in different colors) vs field strength F_0 , for a 20-cycle pulse with $\omega = 1.80$. The SI probability vs F_0 is plotted with dashed line (the same as Fig. 2). (b) Results for a 20-cycle pulse with $\omega = 1.70$.

ionic states. Also, the probability of a higher ionic channel peaks at a larger field strength. To understand these notable peaks, we resort to the Kramer-Henneberger (KH) frame [39] and dressed energy levels on the basis of the lowest-order HFFT [25].

By applying a space translation $\alpha(t) = \int^t A(t') dt'$ to the electron coordinates x_1 and x_2 in Eqs. (1) and (2), the TDSE and the Hamiltonian in the KH frame are obtained,

$$i\partial_t \Phi_{\text{KH}}(x_1, x_2, t) = \hat{H}_{\text{KH}}(t) \Phi_{\text{KH}}(x_1, x_2, t), \quad (11)$$

$$\hat{H}_{\text{KH}}(t) = \sum_{j=1}^2 \left[\frac{\hat{p}_j^2}{2} + V_{\text{en}}[x_j + \alpha(t)] \right] + V_{\text{ec}}(x_1, x_2). \quad (12)$$

The use of the KH frame is essential for the formulation of the HFFT. Note that in our calculations, we do not perform real time propagation of the TDSE in the KH frame, so there is no absorbing boundary such as Eq. (6) used in the KH frame.

In the long-pulse limit, with $\alpha_0 = F_0/\omega^2$, the quiver motion can be simply expressed as $\alpha(t) = \alpha_0 \cos(\omega t)$. We then

perform a Fourier expansion of the oscillating potential V_{en} ,

$$V_{\text{en}}[x_j + \alpha_0 \cos(\omega t)] = \sum_n V_n(\alpha_0, x_j) \exp(-in\omega t) \quad (j = 1, 2). \quad (13)$$

The zeroth components $V_0(\alpha_0, x_1)$ and $V_0(\alpha_0, x_2)$, together with $V_{\text{ec}}(x_1, x_2)$, represent the time-averaged potential in the presence of high-frequency laser fields, which is called the dressed potential in the HFFT [15,25]. Considering a laser pulse, we see α_0 as a time-dependent quantity varying with the pulse envelope and assume that the dressed energy levels follow the pulse envelope (see the discussion below).

To the lowest order, the HFFT gives the structure equation [15,25],

$$\left\{ \sum_{j=1}^2 \left[\frac{\hat{p}_j^2}{2} + V_0(\alpha_0, x_j) \right] + V_{\text{ec}}(x_1, x_2) \right\} \Phi(x_1, x_2) = W(\alpha_0) \Phi(x_1, x_2). \quad (14)$$

Similarly, the structure equation for the He⁺ ion reads

$$\left[\frac{\hat{p}^2}{2} + V_0(\alpha_0, x) \right] \Phi_c(x) = W_c(\alpha_0) \Phi_c(x). \quad (15)$$

We solve Eqs. (14) and (15), and plot some selected dressed energy levels in Figs. 4(a) and 4(b) for the two frequencies $\omega = 1.80$ and $\omega = 1.70$.

With increasing field strength, the rise of the ground-state He energy and the $|1e\rangle$ He⁺ energy can be clearly observed in Fig. 4, while the energy shifts of higher ionic states are less pronounced. With one photon energy, the dressed $|1e\rangle$ He⁺ state can be coupled with dressed odd-wave-function ionic states at resonance for some specific field strengths. Here we also consider the spectral width of the laser pulses, as the dotted curves in Fig. 4 indicate.

On the basis of these dressed energy levels, we propose a sequential ‘‘ionization-excitation’’ mechanism to understand the notable peaks in probabilities of some odd-wave-function ionic channels in Fig. 3. We take the peak of $P_{\text{SI},|6o\rangle}$ at $F_0 = 1.1$ in Fig. 3(a) as an illustrative example. First, the ground-state He atom is ionized into the $|1e\rangle$ He⁺ channel, which is the dominant process for low field strengths. For $\omega = 1.80$, there exists a resonance condition between the $|1e\rangle$ He⁺ and $|6o\rangle$ He⁺ states on the dressed energy levels, around the field strength $F_0 = 1.1$. Such a resonance allows the dressed $|1e\rangle$ He⁺ to be efficiently excited to the dressed $|6o\rangle$ He⁺ with one-photon absorption mediated to the lowest order by the $n = \pm 1$ terms in Eq. (13). With the assumption that the system can adiabatically follow the dressed energy levels, the resonant excitation from the dressed $|1e\rangle$ He⁺ to the dressed $|6o\rangle$ He⁺ can explain the decrease of $P_{\text{SI},|1e\rangle}$ and the increase of $P_{\text{SI},|6o\rangle}$. It can be seen from Fig. 3(a) that $P_{\text{SI},|6o\rangle}$ is much higher than $P_{\text{SI},|1e\rangle}$ at the field strength $F_0 = 1.1$. A view of $P_{\text{SI},|1e\rangle}$ and $P_{\text{SI},|6o\rangle}$ in the time domain will be discussed later in this paper. Similarly, the sequential ionization-excitation mechanism can also explain the peak of $P_{\text{SI},|8o\rangle}$ at $F_0 = 1.8$ in Fig. 3(a). The field strength corresponding to the $P_{\text{SI},|8o\rangle}$ peak is larger than that corresponding to the $P_{\text{SI},|6o\rangle}$ peak, since the resonance condition between the dressed $|1e\rangle$ He⁺ and $|8o\rangle$ He⁺ states appears at a larger field strength F_0 .

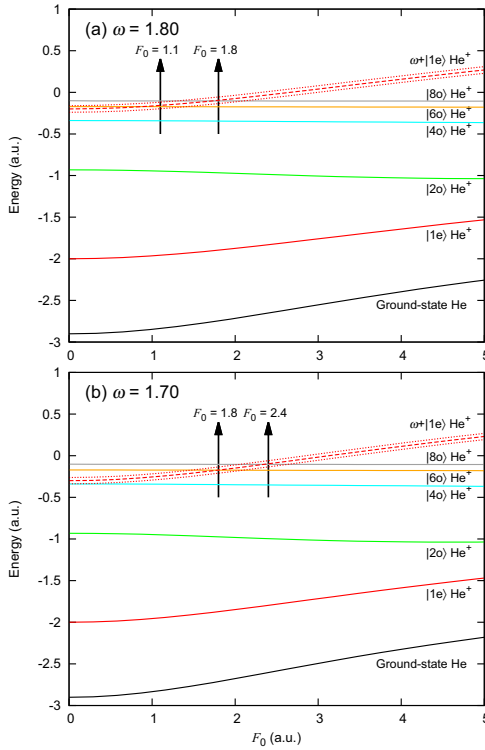


FIG. 4. Dressed energy levels vs field strength F_0 for laser frequencies (a) $\omega = 1.80$ and (b) $\omega = 1.70$. The solid curves, from bottom to top, correspond to ground-state He (black line), $|1e\rangle$ He $^+$ (red line), $|2o\rangle$ He $^+$ (green line), $|4o\rangle$ He $^+$ (cyan line), $|6o\rangle$ He $^+$ (orange line), and $|8o\rangle$ He $^+$ (gray line). The dashed red and dotted red curves are $W_{|1e\rangle} + \omega$ and $W_{|1e\rangle} + \omega \pm \Delta\omega$, respectively. Here $\Delta\omega$ is the FWHM in frequency domain for a 20-cycle pulse, and $W_{|1e\rangle}$ is the dressed ionic ground-state energy [see Eq. (15)]. The arrows indicate the field strengths corresponding to the peaks of $P_{\text{SI},|6o\rangle}$ and $P_{\text{SI},|8o\rangle}$ in Fig. 3.

Turning attention to Fig. 4(b), for $\omega = 1.70$, one finds that the resonance conditions between the dressed $|1e\rangle$ He $^+$ and $|6o\rangle$ He $^+$ states and between the dressed $|1e\rangle$ He $^+$ and $|8o\rangle$ He $^+$ states agree well with the $P_{\text{SI},|6o\rangle}$ peak and the $P_{\text{SI},|8o\rangle}$ peak in Fig. 3(b). Although we cannot completely explain the complicated behavior of $P_{\text{SI},|4o\rangle}$ in Fig. 3(b), the large yields of $|4o\rangle$ He $^+$ at low field strengths are reasonable since the one-photon excitation from the $|1e\rangle$ He $^+$ state to the $|4o\rangle$ He $^+$ state exists at low field strengths, as Fig. 4(b) indicates.

In the above discussion, the sequential ionization-excitation mechanism based on the dressed energy levels should be understood as the main contribution to some specific SI channels. In the dressed energy picture, all the possible transitions between the dressed states occur together with the

adiabatic following of the dressed states. In fact, the sequential ionization-excitation mechanism proposed here is only part of the complicated dynamics, and it becomes prominent for some specific laser parameters.

We perform an additional investigation about this sequential mechanism by taking a time-dependent view on the channel-resolved probabilities at two selected field strengths showing representative behaviors, as Fig. 5 displays. All the time sampling points t_s in Fig. 5 correspond to $A(t_s) = 0$. To obtain the channel-resolved probabilities at each time sampling point t_s , we turn off the laser interaction from t_s by simply replacing $A(t)$ with $\theta(t_s - t)[A(t) - A(t_s)]$ in the time-dependent Hamiltonian [40], and carry out real time propagation with the t-SURFF method as mentioned in Sec. II. For a field strength of $F_0 = 0.5$, both $P_{\text{SI},|1e\rangle}$ and $P_{\text{SI},|6o\rangle}$ increase with time during the pulse, and $P_{\text{SI},|1e\rangle}$ is much larger. This field strength $F_0 = 0.5$ corresponds to the peak of $P_{\text{SI},|1e\rangle}$ in Fig. 3(a). For a field strength of $F_0 = 1.1$, $P_{\text{SI},|1e\rangle}$ grows with time in the beginning, then it starts to decrease around the center of the pulse. Meanwhile, $P_{\text{SI},|6o\rangle}$ shows a dramatic increase with time during the pulse. This field strength $F_0 = 1.1$ corresponds to the peak of $P_{\text{SI},|6o\rangle}$ in Fig. 3(a). The decrease of $P_{\text{SI},|1e\rangle}$ around the center of the pulse reflects the excitation from the $|1e\rangle$ He $^+$ state to the $|6o\rangle$ He $^+$ state in the dressed energy picture.

In closing this section, we mention that strong-field phenomena induced by near-infrared (NIR) laser pulses in multielectron systems have attracted considerable interest over decades [22–24]. In the NIR regime, both ionization and excitation are usually multiphoton processes, so there is hardly any one-photon resonance condition between the involved states. Unlike in the XUV regime where the coupling between only a few states can be easily identified with one-photon resonance conditions, in the NIR regime many states may be coupled with each other via multiphoton processes, resulting in more complicated dynamics.

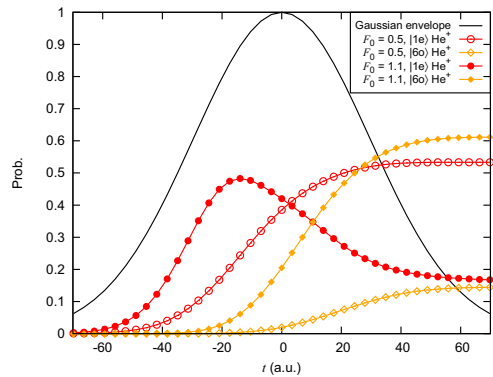


FIG. 5. Time-dependent view of $P_{\text{SI},|1e\rangle}$ (red lines) and $P_{\text{SI},|6o\rangle}$ (orange lines) for a 20-cycle pulse with frequency $\omega = 1.80$, at two different field strengths $F_0 = 0.5$ and $F_0 = 1.1$. The Gaussian envelope (with maximum set to 1) is also plotted with solid black line.

IV. CONCLUSION

In this paper, we studied the ionization of He by intense XUV laser pulses by performing numerical simulations. We considered a frequency regime where the lowest SI channel is expected to be stabilized and ionization into other channels requires absorption of two or more photons, as illustrated in Fig. 1. We found that there is no obvious stabilization against TI in this frequency regime, due to large yields of multiphoton DI for superintense fields. We took a detailed view of probabilities into different SI channels as a function of the field strength, observing interesting peaks of probabilities into some odd-wave-function ionic states. To our knowledge, such research on channel-resolved ionization probabilities has not been reported previously. We showed that it can decode more information about strong-field ionization of multielectron systems. From the dressed energy levels based on the lowest order HFFT, we found one-photon resonance conditions between the dressed ionic ground state and excited

states at the field strengths corresponding to those peaks. Thus we proposed a sequential ionization-excitation mechanism in the dressed energy picture: after the atom is singly ionized into the lowest ionic channel, the ion is further excited to another state at the field strength where the resonance condition between the dressed ionic states is fulfilled. Finally, a time-dependent view of the channel-resolved probabilities was also presented to further reveal the proposed sequential mechanism.

ACKNOWLEDGMENTS

This work was supported by the European Research Council StG (Project No. 277767-TDMET), and the VKR center of excellence, QUSCOPE. The numerical results presented in this work were performed at the Centre for Scientific Computing, Aarhus.

-
- [1] G. Sansone, L. Poletto, and M. Nisoli, High-energy attosecond light sources, *Nat. Photon.* **5**, 655 (2011).
 - [2] M. Chini, K. Zhao, and Z. Chang, The generation, characterization and applications of broadband isolated attosecond pulses, *Nat. Photon.* **8**, 178 (2014).
 - [3] W. Ackermann, G. Asova, V. Ayvazyan, A. Azima, N. Baboi, J. Bähr, V. Balandin, B. Beutner, A. Brandt, A. Bolzmann *et al.*, Operation of a free-electron laser from the extreme ultraviolet to the water window, *Nat. Photon.* **1**, 336 (2007).
 - [4] B. W. McNeil and N. R. Thompson, X-ray free-electron lasers, *Nat. Photon.* **4**, 814 (2010).
 - [5] M. Hentschel, R. Kienberger, C. Spielmann, G. Reider, N. Milosevic, T. Brabec, P. Corkum, U. Heinzmann, M. Drescher, and F. Krausz, Attosecond metrology, *Nature (London)* **414**, 509 (2001).
 - [6] F. Krausz and M. I. Stockman, Attosecond metrology: From electron capture to future signal processing, *Nat. Photon.* **8**, 205 (2014).
 - [7] F. Krausz and M. Ivanov, Attosecond physics, *Rev. Mod. Phys.* **81**, 163 (2009).
 - [8] M. Fedorov and A. Movsesian, Field-induced effects of narrowing of photoelectron spectra and stabilisation of Rydberg atoms, *J. Phys. B* **21**, L155 (1988).
 - [9] M. Pont and M. Gavrilu, Stabilization of Atomic Hydrogen in Superintense, High-frequency Laser Fields of Circular Polarization, *Phys. Rev. Lett.* **65**, 2362 (1990).
 - [10] M. P. de Boer, J. H. Hoogenraad, R. B. Vrijen, L. D. Noordam, and H. G. Muller, Indications of High-intensity Adiabatic Stabilization in Neon, *Phys. Rev. Lett.* **71**, 3263 (1993).
 - [11] R. R. Jones, D. W. Schumacher, and P. H. Bucksbaum, Population trapping in Kr and Xe in intense laser fields, *Phys. Rev. A* **47**, R49 (1993).
 - [12] M. P. de Boer, J. H. Hoogenraad, R. B. Vrijen, R. C. Constantinescu, L. D. Noordam, and H. G. Muller, Adiabatic stabilization against photoionization: An experimental study, *Phys. Rev. A* **50**, 4085 (1994).
 - [13] J. H. Hoogenraad, R. B. Vrijen, and L. D. Noordam, Ionization suppression of Rydberg atoms by short laser pulses, *Phys. Rev. A* **50**, 4133 (1994).
 - [14] N. J. van Druten, R. C. Constantinescu, J. M. Schins, H. Nieuwenhuize, and H. G. Muller, Adiabatic stabilization: Observation of the surviving population, *Phys. Rev. A* **55**, 622 (1997).
 - [15] M. Gavrilu, Atomic stabilization in superintense laser fields, *J. Phys. B* **35**, R147 (2002).
 - [16] A. M. Popov, O. V. Tikhonova, and E. A. Volkova, Strong-field atomic stabilization: Numerical simulation and analytical modelling, *J. Phys. B* **36**, R125 (2003).
 - [17] M. Gavrilu and J. Shertzer, Two-electron atoms in superintense radiation fields: Dichotomy and stabilization, *Phys. Rev. A* **53**, 3431 (1996).
 - [18] D. Bauer and F. Ceccherini, Electron correlation versus stabilization: A two-electron model atom in an intense laser pulse, *Phys. Rev. A* **60**, 2301 (1999).
 - [19] T. Birkeland, R. Nepstad, and M. Førre, Stabilization of Helium in Intense XUV Laser Fields, *Phys. Rev. Lett.* **104**, 163002 (2010).
 - [20] S. A. Sørngård, S. Askeland, R. Nepstad, and M. Førre, Multiphoton ionization and stabilization of helium in superintense XUV fields, *Phys. Rev. A* **83**, 033414 (2011).
 - [21] L. Yue and L. B. Madsen, Characterization of Molecular Breakup by Very Intense Femtosecond XUV Laser Pulses, *Phys. Rev. Lett.* **115**, 033001 (2015).
 - [22] W. Becker and H. Rottke, Many-electron strong-field physics, *Contemp. Phys.* **49**, 199 (2008).
 - [23] C. F. de Morisson Faria and X. Liu, Electron electron correlation in strong laser fields, *J. Mod. Opt.* **58**, 1076 (2011).
 - [24] W. Becker, X. Liu, P. J. Ho, and J. H. Eberly, Theories of photoelectron correlation in laser-driven multiple atomic ionization, *Rev. Mod. Phys.* **84**, 1011 (2012).
 - [25] M. Gavrilu, *Atoms in Intense Laser Fields* (Academic Press, San Diego, 1992).

IONIZATION OF HELIUM BY INTENSE XUV LASER ...

PHYSICAL REVIEW A 93, 043412 (2016)

- [26] T. N. Rescigno and C. W. McCurdy, Numerical grid methods for quantum-mechanical scattering problems, *Phys. Rev. A* **62**, 032706 (2000).
- [27] B. I. Schneider, L. A. Collins, and S. X. Hu, Parallel solver for the time-dependent linear and nonlinear Schrödinger equation, *Phys. Rev. E* **73**, 036708 (2006).
- [28] T. J. Park and J. C. Light, Unitary quantum time evolution by iterative Lanczos reduction, *J. Chem. Phys.* **85**, 5870 (1986).
- [29] X. Guan, O. Zatsarinny, K. Bartschat, B. I. Schneider, J. Feist, and C. J. Noble, General approach to few-cycle intense laser interactions with complex atoms, *Phys. Rev. A* **76**, 053411 (2007).
- [30] R. Kosloff and H. Tal-Ezer, A direct relaxation method for calculating eigenfunctions and eigenvalues of the Schrödinger equation on a grid, *Chem. Phys. Lett.* **127**, 223 (1986).
- [31] L. Tao and A. Scrinzi, Photo-electron momentum spectra from minimal volumes: the time-dependent surface flux method, *New J. Phys.* **14**, 013021 (2012).
- [32] A. Scrinzi, t-SURFF: Fully differential two-electron photo-emission spectra, *New J. Phys.* **14**, 085008 (2012).
- [33] L. Yue and L. B. Madsen, Dissociation and dissociative ionization of H_2^+ using the time-dependent surface flux method, *Phys. Rev. A* **88**, 063420 (2013).
- [34] A. Karamatskou, S. Pabst, Y.-J. Chen, and R. Santra, Calculation of photoelectron spectra within the time-dependent configuration-interaction singles scheme, *Phys. Rev. A* **89**, 033415 (2014).
- [35] A. Zielinski, V. P. Majety, and A. Scrinzi, Double photoelectron momentum spectra of helium at infrared wavelength, *Phys. Rev. A* **93**, 023406 (2016).
- [36] J. Muga, J. Palao, B. Navarro, and I. Egusquiza, Complex absorbing potentials, *Phys. Rep.* **395**, 357 (2004).
- [37] Q. Su, B. P. Irving, and J. H. Eberly, Ionization modulation in dynamic stabilization, *Laser Phys.* **7**, 568 (1997).
- [38] M. Dörr and R. M. Potvliege, Adiabatic stabilization in photodetachment by ultrashort pulses, *J. Phys. B* **33**, L233 (2000).
- [39] W. C. Henneberger, Perturbation Method for Atoms in Intense Light Beams, *Phys. Rev. Lett.* **21**, 838 (1968).
- [40] L. B. Madsen and D. Dimitrovski, Time-resolved subcycle dynamics: Importance of physical fields and gauge invariance, *Phys. Rev. A* **78**, 023403 (2008).

Paper II. Physical Review A 94, 053424 (2016)

Title:

**Sequential and nonsequential double ionization of helium
by intense XUV laser pulses:
Revealing ac Stark shifts from joint energy spectra**

Authors: Chuan Yu and Lars Bojer Madsen

DOI: <https://doi.org/10.1103/PhysRevA.94.053424>

Reprinted with permission from the American Physical Society.
Copyright (2016) by the American Physical Society.

My contribution to this publication includes (1) implementation of the theoretical calculations and (2) preparation of the manuscript (with figures).

PHYSICAL REVIEW A 94, 053424 (2016)

Sequential and nonsequential double ionization of helium by intense XUV laser pulses: Revealing ac Stark shifts from joint energy spectra

Chuan Yu and Lars Bojer Madsen

Department of Physics and Astronomy, Aarhus University, DK-8000 Aarhus C, Denmark

(Received 3 August 2016; published 29 November 2016)

Double ionization of a model helium system by intense extreme ultraviolet laser pulses is investigated by solving the time-dependent Schrödinger equation and extracting the photoelectron spectra. Considering a frequency regime where the nonsequential two-photon double ionization is expected to dominate the double ionization process according to the perturbation theory, we identify the sequential and nonsequential mechanisms from the joint energy spectra of two electrons in the strong-field regime. In the nonperturbative regime, we find that sequential multiphoton double ionization shows remarkable peaks in the joint energy spectra and these peaks spread their widths with increasing laser field strength, which is caused by the ac Stark effect. Thus in the strong-field regime, the ac Stark shifts of different ionic states can be observed from the sequential multiphoton features in the joint energy spectra and the signs of the ac Stark shifts can be controlled by the laser frequency. We also find that the nonsequential mechanism dominates double ionization only at low field strengths while the sequential multiphoton mechanism contributes substantially at high field strengths, in accordance with estimates from rate equations.

DOI: [10.1103/PhysRevA.94.053424](https://doi.org/10.1103/PhysRevA.94.053424)

I. INTRODUCTION

Double ionization (DI) of multielectron systems has been of great interest in atomic and molecular physics over decades. Recent developments of extreme-ultraviolet (XUV) and x-ray laser sources [1–3] provide possibilities for experimental investigations on DI with one- or multiphoton absorption. Specifically, two-photon DI has received considerable attention in both experimental [4–9] and theoretical [10–18] studies.

Helium is the fundamental system for illustrating the dynamics in DI. Two-photon DI of He is classified into two categories: sequential and nonsequential. In the sequential mechanism, one photon ionizes the ground state He into He^+ (step 1) and then the other photon ionizes He^+ to He^{++} (step 2). This sequential process is possible and dominant if the photon energy is larger than the ionization potential of He^+ . In the nonsequential mechanism, the ground state He is directly ionized into He^{++} by absorbing two photons simultaneously. Many theoretical studies focused on these two mechanisms, and perturbation theory was often used in their analyses [10,11,14–17].

In the nonperturbative regime, the strong-field laser-matter interaction can induce above threshold ionization (ATI) structures in photoelectron energy spectra (PES). DI joint energy spectra (JES) and joint momentum distributions have been extensively studied and they can provide information to decipher the DI mechanisms [19–24]. Also for molecular systems, there have been both theoretical and experimental studies on electron-nuclear JES, for understanding the correlated electron-nuclear dynamics and energy sharing [25–27]. ATI structures in DI JES (or joint momentum distributions) have been observed in both theoretical calculations [24,28] and recent experiments [29,30]. In this work we consider a strong-field regime in which a helium atom can be doubly ionized by multiphoton absorption, i.e., ATI structures are expected to appear in the JES. Considering a photon energy that is larger than half the DI threshold of He but smaller than the ionization potential of He^+ , one would assert that

DI is dominated by the nonsequential two-photon process in the perturbation regime. In the considered strong-field regime, however, the sequential DI mechanism is still possible via multiphoton processes involving three or more photons and these ionization pathways can compete with the nonsequential two-photon DI mechanism and enrich the dynamics. The laser frequency and multiphoton DI mechanisms are illustrated in Fig. 1. As an example, we consider in Fig. 1, in addition to the nonsequential two-photon DI process, a few selected three-photon processes: the ground-state He can be ionized into the ground-state He^+ by absorbing one photon and then He^+ is ionized into He^{++} by absorbing two photons; He can also be ionized into the first-excited-state He^+ by absorbing two photons and then He^+ is ionized into He^{++} by absorbing one photon. Briefly speaking, there exist sequential three-photon DI via different ionic channels and nonsequential three-photon DI.

In this paper, we identify the sequential and nonsequential DI mechanisms from the JES of two electrons in the strong-field regime. As we will show below, the sequential DI pathways via different ionic channels can provide information of the ac Stark shifts in different ionic states. Recently some theoretical studies that focused on the PES of a single electron found that the ac Stark effect can result in multipeak structures in the PES [31–34]. In particular, Ref. [34] discussed multipeak structures in the single ionization (SI) PES of He by ignoring the DI for intermediate laser intensities, in which the ac Stark energy shifts are relatively small. In our work, the effect of ac Stark shifts on the DI PES is investigated in the nonperturbative strong-field XUV regime. In the JES, the effect of ac Stark shifts appears as pronounced spectral features in the sequential multiphoton DI processes. In addition, the contribution of the nonsequential two-photon DI mechanism to the total DI probability is studied for different laser field strengths.

This paper is organized as follows. In Sec. II we introduce the theoretical and numerical methods used in this work. In Sec. III we present and discuss the results of the calculations.

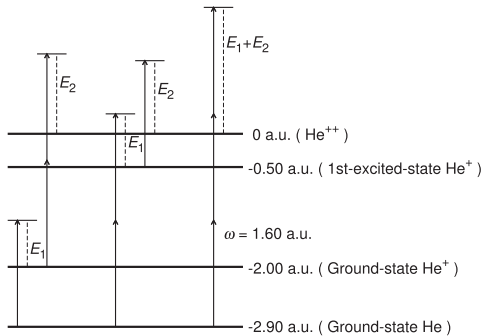


FIG. 1. The laser frequency considered in this work, illustrated with some energy levels of He and He⁺. Nonsequential two-photon DI is allowed, while sequential two-photon DI is forbidden. Three of the three-photon DI mechanisms, i.e., the sequential three-photon DI via two different ionic channels and the nonsequential three-photon DI, are presented as examples.

Finally we give concluding remarks in Sec. IV. Atomic units are used throughout unless otherwise stated.

II. THEORETICAL MODEL AND METHODS

We consider a one-dimensional (1D) model of helium in the presence of a linearly polarized laser pulse, in which the two electrons are allowed to move along the direction of the laser polarization. This 1D model reduces computational difficulty, and allows us to perform calculations for long-pulse interactions in the strong-field regime. We solve the time-dependent Schrödinger equation (TDSE)

$$i\partial_t\Psi(x_1,x_2,t) = H(t)\Psi(x_1,x_2,t), \quad (1)$$

with the Hamiltonian

$$H(t) = \sum_{j=1}^2 \left[\frac{p_j^2}{2} + A(t)p_j + V_{\text{en}}(x_j) \right] + V_{\text{ee}}(x_1,x_2). \quad (2)$$

Here x_j and $p_j = -i\partial_{x_j}$ ($j = 1, 2$) are the electron coordinate and momentum operators, respectively;

$$V_{\text{en}}(x_j) = \frac{-Z_{\text{en}}}{\sqrt{x_j^2 + a_{\text{en}}}} \quad (j = 1, 2), \quad (3)$$

$$V_{\text{ee}}(x_1,x_2) = \frac{Z_{\text{ee}}}{\sqrt{(x_1 - x_2)^2 + a_{\text{ee}}}} \quad (4)$$

are the electron-nuclei interaction and the electron-electron interaction, where $a_{\text{en}}, a_{\text{ee}}$ are softening parameters used to smoothen the Coulomb singularity and $Z_{\text{en}}, Z_{\text{ee}}$ are introduced to adjust the softened Coulomb interaction strengths in this 1D model. By choosing $Z_{\text{en}} = 1.1225$, $Z_{\text{ee}} = 0.4725$, $a_{\text{en}} = 0.0917$, and $a_{\text{ee}} = 0.0225$, we obtain the He ground-state energy -2.90 , He⁺ ground-state energy -2.00 , and first-excited-state energy -0.50 , which are in good agreement with the values for the 3D system.

In the TDSE, the laser interaction is described in velocity gauge by the vector potential $A(t)$ within the dipole approximation, and a time-dependent energy shift from the $A^2(t)$ term in the Hamiltonian has been unitarily transformed away. In our calculations, a vector potential with a Gaussian envelope is used:

$$A(t) = \frac{F_0}{\omega} \exp\left(-4\ln 2 \frac{t^2}{\tau^2}\right) \sin(\omega t), \quad (5)$$

where F_0 is the maximum field strength related to the peak intensity by $I = F_0^2/(8\pi\alpha)$, ω is the angular frequency, and τ is the full width at half maximum (FWHM) of the envelope. The pulse duration is described by the number of cycles within τ , $N_c = \omega\tau/(2\pi)$.

The numerical methods used to solve the TDSE and extract the PES are as in Ref. [35]. It is worth mentioning that the time-dependent surface flux (t-SURFF) method [36,37] allows us to extract the PES with a relatively small simulation box, which is advantageous in strong-field computations (see also Ref. [38] for an extension of the t-SURFF method to the molecular case and Refs. [39,40] for other recent applications). Following Ref. [35], we denote by $S_{\text{DI},c}(E_1)$ and $S_{\text{DI}}(E_1, E_2)$ the SI PES with the ion left in channel c and the DI JES, respectively. For the ion He⁺, we use the notations $|1e\rangle, |2o\rangle, |3e\rangle, |4o\rangle, \dots$, for the ground and excited states, since a given electronic state wave function can be classified as even (e) or odd (o) in the 1D model.

When numerically solving the TDSE, we set up a simulation box $r_{\text{max}} = 120$, which is discretized with 120 equal-size finite elements and nine Gauss-Lobatto basis functions in each element. To avoid unphysical reflections at the boundaries of the simulation box, a complex absorbing potential (CAP) [41]

$$V_{\text{CAP}}(x_1,x_2) = -i[f_{\text{CAP}}(x_1) + f_{\text{CAP}}(x_2)] \quad (6)$$

is added to the Hamiltonian in real time propagation, where $f_{\text{CAP}}(x)$ is a function of the form

$$f_{\text{CAP}}(x) = \begin{cases} 0, & |x| \leq r_c \\ 1 - \cos\left[\frac{\pi(|x| - r_c)}{2(r_{\text{max}} - r_c)}\right], & r_c < |x| < r_{\text{max}} \end{cases}. \quad (7)$$

The t-SURFF surfaces are placed at $|x_1|, |x_2| = 55$ and the CAP radius is $r_c = 60$, which are slightly different from those used in Ref. [35]. We also perform simulations with the t-SURFF surfaces placed at $|x_1|, |x_2| = 60$ and the CAP radius $r_c = 65$ (the same as in Ref. [35]), and confirm that the results are not significantly changed. A time step of $\Delta t = 0.005$ is used in real time propagation, which is the same as in Ref. [35].

As mentioned in the Introduction, the sequential DI process can be seen as consisting of two steps. Step 2 purely involves one-electron dynamics, and can therefore be analyzed by solving the TDSE for He⁺,

$$i\partial_t\Psi_1(x,t) = H_1(t)\Psi_1(x,t), \quad (8)$$

with the one-electron Hamiltonian

$$H_1(t) = \left[\frac{p^2}{2} + A(t)p + V_{\text{en}}(x) \right]. \quad (9)$$

We choose the ground state or any other bound eigenstate as the initial state in the ion when solving the one-electron TDSE, corresponding to step 2 of the sequential DI via

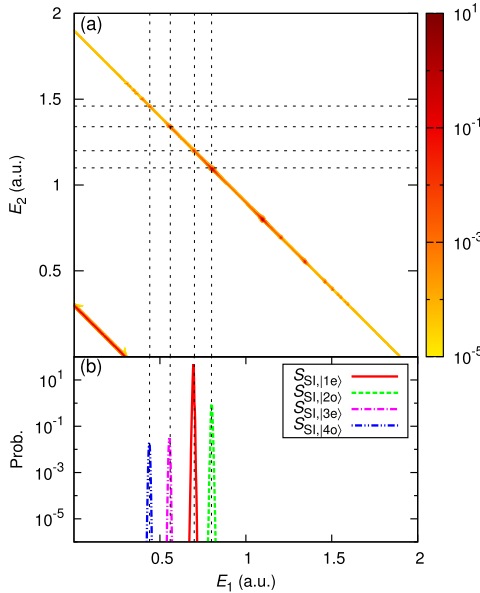


FIG. 2. (a) The DI JES $S_{\text{DI}}(E_1, E_2)$ for a laser pulse with $F_0 = 0.1$, $\omega = 1.60$, $N_c = 200$. (b) The SI PES in the lowest four ionic channels $S_{\text{SI},1e}$, $S_{\text{SI},2o}$, $S_{\text{SI},3e}$, $S_{\text{SI},4o}$, for the same laser pulse. Based on energy conservation, the crossings of the black dotted lines along $E_1 + E_2 = 3\omega - I_p^{\text{DI}}$ in (a) indicate some expected electron energy pairs (E_1, E_2) in the sequential three-photon DI process while the black dotted lines in (b) indicate some expected PES peaks in SI. The maximum in the DI JES is $S_{\text{DI}}(E_1 = 0.801, E_2 = 1.097) = S_{\text{DI}}(E_1 = 1.097, E_2 = 0.801) = 1.57$.

different ionic channels. In our later discussion, the PES out of different He^+ states will be used as an analysis of step 2 in the sequential DI process.

III. RESULTS AND DISCUSSION

A. JES in the perturbative limit

Figure 2 shows (a) the DI JES and (b) the SI PES in the lowest four ionic channels, for a laser pulse with $F_0 = 0.1$, $\omega = 1.60$, $N_c = 200$. There exists an $E_1 \leftrightarrow E_2$ exchange symmetry in the DI JES. When discussing the sequential process in this section, for convenience, we use E_1 for the first electron freed in step 1 and E_2 for the second electron freed in step 2. Without considering ac Stark effects, the nonsequential N -photon ($N \geq 2$) DI channel fulfills

$$E_1 + E_2 = N\omega - I_p^{\text{DI}}, \quad (10)$$

where I_p^{DI} is the ionization potential for DI. For the considered laser frequency, the sequential three-photon DI can be classified into two types, depending on the ionic channels involved. As mentioned in Sec. I (Fig. 1), the sequential three-photon DI via the ground-state ionic channel fulfills $E_1 = \omega - I_p^{\text{DI}} + I_p^{(1)}$

and $E_2 = 2\omega - I_p^{(1)}$, where $I_p^{(1)}$ is the ionization potential of the ground-state He^+ . The sequential three-photon DI via any other ionic channel fulfills $E_1 = 2\omega - I_p^{\text{DI}} + I_p^{(k)}$ and $E_2 = \omega - I_p^{(k)}$, where $I_p^{(k)}$ ($k \geq 2$) is the ionization potential of the excited-state He^+ . More generally, for the sequential N -photon DI via the k th ionic channel we have

$$E_1 = N_1\omega - I_p^{\text{DI}} + I_p^{(k)}, \quad (11)$$

$$E_2 = N_2\omega - I_p^{(k)}, \quad (12)$$

where N_1 and N_2 are integers that ensure $E_1 > 0$, $E_2 > 0$ and $N_1 + N_2 = N$.

We see from Fig. 2(a) that the nonsequential two-photon DI signal displayed by the diagonal line in the lower left part is dominant in the JES for this field strength (quantitative evidence will be shown later in Fig. 4). Local maxima can be found along the nonsequential three-photon DI energy lines, which are signatures of the sequential processes (see also Refs. [23,24,40]). In the sequential DI, the ejection of the first electron (step 1) can be seen as a SI process. Thus we expect the energy of the first electron in the sequential DI process to agree with the SI PES peak in the corresponding ionic channel. This is verified by comparing Fig. 2(b) with Fig. 2(a). Indeed, the PES peaks agree well with the expected values, which validates our calculations and indicates that ac Stark effects are negligible for this field strength.

We note that for the considered laser frequency $\omega = 1.60$, the sequential three-photon DI processes via different ionic channels manifest distinct peaks in the JES, allowing us to distinguish easily the sequential pathways via different ionic channels. All the sequential three-photon DI peaks fulfill $E_1 < E_2$, i.e., the second electron has more energy than the first. This also facilitates our analyses of the sequential three-photon DI processes, i.e., we may focus on the sequential three-photon DI peaks in the $E_1 < E_2$ half of the JES, since the similar peaks in the other half of the JES are just the results of the $E_1 \leftrightarrow E_2$ exchange symmetry.

B. JES in the strong-field regime

Keeping $\omega = 1.60$ and $N_c = 200$ fixed, we now consider numerical simulations for higher field strengths. In Fig. 3 we present the DI JES and the SI PES in the lowest four ionic channels as in Fig. 2, together with the PES out of the $|1e\rangle$ and $|2o\rangle$ He^+ states, for field strengths $F_0 = 0.5$ and $F_0 = 1.0$. We find from Figs. 3(a) and 3(d) that the three-photon sequential processes, i.e., the peaks on the diagonal line $E_1 + E_2 = 3\omega - I_p^{\text{DI}}$, dominate the DI for the intense field strengths. Also, these peaks due to sequential processes spread their widths with increasing field strength. In more details, for the sequential three-photon DI via the $|1e\rangle$ ionic channel, E_1 can be smaller than $\omega - I_p^{\text{DI}} + I_p^{(1)} = 0.70$ while E_2 can be larger than $2\omega - I_p^{(1)} = 1.20$; for the sequential three-photon DI via the $|2o\rangle$ ionic channel, E_1 can be larger than $2\omega - I_p^{\text{DI}} + I_p^{(2)} = 0.80$ while E_2 can be smaller than $\omega - I_p^{(2)} = 1.10$. On the other hand, the nonsequential features in the JES are not significantly affected, except an overall increase of the DI yield compared with Fig. 2.

These increased widths of the sequential DI peaks in the JES reflect the ac Stark shifts in different ionic channels. In

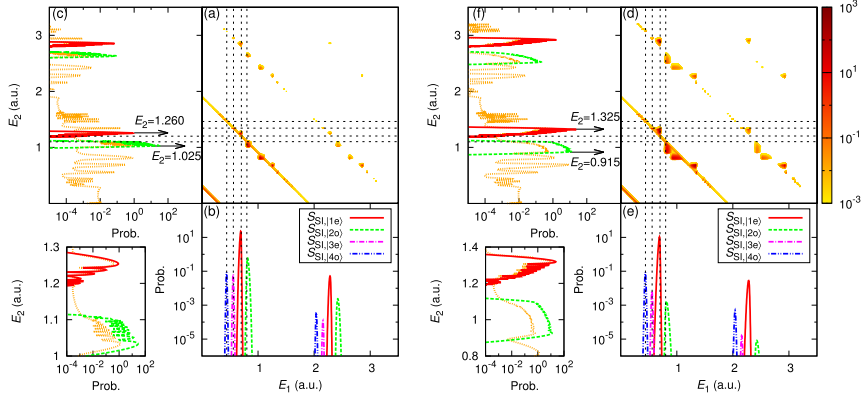


FIG. 3. (a),(b) Same as Fig. 2, the DI JES and the channel-resolved SI PES, but for a field strength $F_0 = 0.5$. (c) The PES of the ground state (red solid line) and first-excited state (green dashed line) of He^+ , together with the DI JES integrated along E_1 , $\int S_{\text{DI}}(E_1, E_2) dE_1$ (orange dotted line). (d)–(f) Same as (a)–(c), but for $F_0 = 1.0$. Arrows in (c) and (f) indicate the PES peak positions. For better visualization, zoom-ins of the selected peaks in (c) and (f) are presented in separate panels below (c) and (f). The maxima in the DI JES are (a) $S_{\text{DI}}(E_1 = 0.813, E_2 = 1.033) = S_{\text{DI}}(E_1 = 1.033, E_2 = 0.813) = 3.96 \times 10^1$ and (d) $S_{\text{DI}}(E_1 = 0.691, E_2 = 1.319) = S_{\text{DI}}(E_1 = 1.319, E_2 = 0.691) = 4.64 \times 10^2$, respectively.

the sequential DI, as mentioned above, step 1 can be seen as a SI process (from He to He^+) while step 2 can be seen as a one-electron problem (from He^+ to He^{++}). So the SI PES of He and the PES of He^+ are presented as side panels in Fig. 3 to illustrate separately the ac Stark effects in step 1 and step 2 in the sequential DI. We see from Figs. 3(b) and 3(e) that the SI PES in the $|1e\rangle$ and $|2o\rangle$ ionic channels show peak shifts and broadenings, which agree with the energy of the first electron (step 1) in the DI JES. Then we see from Figs. 3(c) and 3(f) that the PES out of the $|1e\rangle$ and $|2o\rangle$ He^+ states also show peak shifts and broadenings, which agree well with the energy of the second electron (step 2) in the DI JES. Note that these two types of energy shifts are not necessarily the same in magnitude, which will be discussed later.

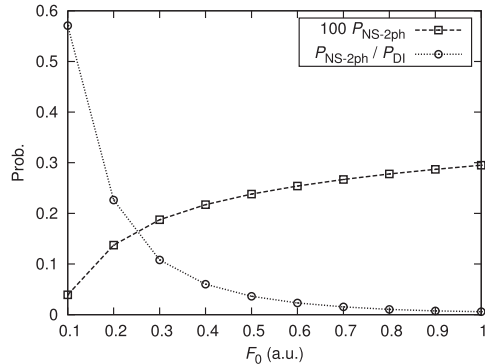


FIG. 4. The nonsequential two-photon DI probability $P_{\text{NS-2ph}}$ (multiplied by a factor of 100) and the ratio $P_{\text{NS-2ph}}/P_{\text{DI}}$ [see Eqs. (21) and (22)] vs field strength F_0 , for fixed $\omega = 1.60$ and $N_c = 200$.

It is worth mentioning that although the one-electron PES of He^+ in different bound states can be quite helpful for understanding spectral features of the sequential DI, the wave packet in He^+ is much more complex, i.e., many states are populated with different amplitudes and phases, which may be important in shaping the DI spectra. In Figs. 3(c) and 3(f), we also compare the PES of the ground-state and first-excited-state He^+ with the DI JES integrated along E_1 , $\int S_{\text{DI}}(E_1, E_2) dE_1$. In the PES of He^+ , the weights of different states are not taken into account. Thus the comparison shows different intensities in the spectral peaks. Also, the multiplex structures of $\int S_{\text{DI}}(E_1, E_2) dE_1$ indicate the complexity of the DI spectra, which originates from the contributions of many different channels. For the selected peaks, however, the comparison shows that the PES of He^+ gives a good description of the peak shifts in step 2 of the sequential DI. Therefore in our discussion it is valid to analyze the ac Stark shifts in step 2 of the sequential DI by looking at the one-electron PES of He^+ .

The peak shifts in the SI PES were reported in Ref. [34] for intermediate laser intensities. The SI PES peak shifts observed in our work agree qualitatively with Ref. [34], i.e., the peaks of $S_{\text{SI},|1e\rangle}$ and $S_{\text{SI},|2o\rangle}$ are shifted to lower and higher energy, respectively. In the strong-field regime, the ac Stark effect is more pronounced and it can also be observed from the DI JES. Also, we would like to mention that compared with the ac Stark effects observed from the PES of a one-electron system (in its ground state) [31,32], the peak shifts observed from the DI JES can help us to reveal the ac Stark effects of different ionic states in a two-electron system (He), as step 1 in the sequential DI process serves to prepare the ion (He^+) in different states.

C. ac Stark shifts in the Floquet formalism

For a better understanding of the ac Stark shifts, we consider the Floquet theory which applies to monochromatic laser fields in the long-pulse limit (remember that we consider $N_c = 200$).

For completeness, we briefly introduce the Floquet formalism by considering a general atomic system in the presence of a monochromatic laser field within the dipole approximation (see, e.g., Ref. [42] for a review). The Hamiltonian of the system $H(t)$ contains a time-independent part H_0 and a time-dependent laser-interaction term $H_I(t)$,

$$H(t) = H_0 + H_I(t), \quad (13)$$

which is periodical in time. The Floquet ansatz assumes the wave function $\Psi_{\mathcal{E}}(t)$ to have the form

$$\Psi_{\mathcal{E}}(t) = \exp(-i\mathcal{E}t) \sum_{n=-\infty}^{+\infty} [\exp(-in\omega t)\Phi_{n,\mathcal{E}}], \quad (14)$$

where \mathcal{E} is the quasienergy of the state. We then expand the time-dependent part of the Hamiltonian in a Fourier series,

$$H_I(t) = \sum_{n=-\infty}^{+\infty} (H_I)_n \exp(-in\omega t), \quad (15)$$

and derive an infinite system of time-independent coupled equations from the TDSE,

$$(H_0 - n\omega)\Phi_{n,\mathcal{E}} + \sum_{k=-\infty}^{+\infty} (H_I)_{n-k}\Phi_{k,\mathcal{E}} = \mathcal{E}\Phi_{n,\mathcal{E}}. \quad (16)$$

For convenience, we write Eq. (16) in a matrix form

$$\underline{H}\underline{\Phi} = \underline{\mathcal{E}}\underline{\Phi}, \quad (17)$$

where $\underline{\Phi}$ is the Floquet vector composed of $\Phi_{n,\mathcal{E}}$, \underline{H} is the Floquet Hamiltonian and $\underline{\mathcal{E}}$ is a diagonal matrix of quasienergies.

In both velocity and length gauges, the Fourier expansion Eq. (15) is simply on the form

$$H_I(t) = H_+ \exp(-i\omega t) + H_- \exp(+i\omega t). \quad (18)$$

Accordingly, Eq. (16) is simplified to

$$(H_0 - n\omega)\Phi_{n,\mathcal{E}} + H_+ \Phi_{n-1,\mathcal{E}} + H_- \Phi_{n+1,\mathcal{E}} = \mathcal{E}\Phi_{n,\mathcal{E}}, \quad (19)$$

i.e., the Floquet Hamiltonian is formally a tridiagonal block matrix of infinite size.

Any quasienergy \mathcal{E} can be written in the form $\mathcal{E} = \mathcal{E}_0 + \Delta + n\omega$, where \mathcal{E}_0 is the corresponding field-free eigenenergy and Δ is the ac Stark shift. In the field-free limit, $\Delta = 0$, i.e., the quasienergy is exactly the field-free eigenenergy (we can take $n = 0$ in this case). In general, diagonalization of the Floquet Hamiltonian can extract the ac Stark effect, in both the perturbative and nonperturbative regime.

As an extension of the above Floquet theory, the complex-scaled non-Hermitian Floquet Hamiltonian method has been extensively used in the nonperturbative regime [42]. With the complex scaling transformation [e.g., in the 1D model, $x \rightarrow x \exp(i\theta)$], the quasienergy is therefore complex,

$$\mathcal{E} = \mathcal{E}_0 + \Delta + n\omega - i\Gamma/2, \quad (20)$$

where Γ is a real value describing the decay rate of the state. The complex-scaled Floquet Hamiltonian method makes it easier to identify the bound and continuum states from the complex quasienergies, since the continuum states will show prominent decay rates.

It is worth mentioning that the quasienergy is gauge dependent. For example, transforming away the $A^2(t)$ term in the velocity-gauge Hamiltonian causes the quasienergy to be downshifted by the ponderomotive potential $U_p = F_0^2/4\omega^2$ ($\times N_e$, the number of electrons) [43]. However, the energy difference between any two states, which is the observable of interest, is gauge invariant. Strictly speaking, it is therefore only meaningful to talk about the shifts of energy differences between the states instead of the shifts of the states individually.

With the above formalism in place, we are now ready to relate it to our He results. To extract the ac Stark effect in the Floquet formalism, one should construct the Floquet Hamiltonian matrix in a Hilbert space including all the involved states. In the sequential DI, two-electron states are involved in the ionization from He to He⁺ while one-electron states are involved in the ionization from He⁺ to He⁺⁺. Thus we see that the ac Stark effects in step 1 and step 2 are different on the basis of the Floquet formalism, since the corresponding Floquet Hamiltonian matrices should be constructed in different Hilbert spaces.

For the considered laser frequency $\omega = 1.60$, we apply the complex-scaled Floquet Hamiltonian method for He⁺ at two field strengths $F_0 = 0.5$ and $F_0 = 1.0$, to find the ac-Stark-shifted ionization potential of different ionic states and to compare those with the PES peak shifts seen in Figs. 3(c) and 3(f). In our numerical simulations, the Floquet Hamiltonian is truncated to a matrix of finite size, i.e., we consider $n = 0, \pm 1, \dots, \pm 10$ in Eq. (19). The convergence is checked by extending the range of n in Eq. (19), which means taking more multiphoton processes into consideration. The results computed with two complex scaling parameters $\theta = 0.1$ and $\theta = 0.2$ are the same to an acceptable accuracy, which also confirms the convergence. The ac Stark shift of the $|1e\rangle$ He⁺ ionization potential $I_p^{(1)}$ is found to be -0.059 for $F_0 = 0.5$ and -0.125 for $F_0 = 1.0$, while the ac Stark shift of the $|2o\rangle$ He⁺ ionization potential $I_p^{(2)}$ is found to be $+0.074$ for $F_0 = 0.5$ and $+0.185$ for $F_0 = 1.0$. By simple energy conservation, any ionization potential shift will lead to the corresponding PES peak shift with an opposite sign. As seen from Figs. 3(c) and 3(f), the PES peak shift of $|1e\rangle$ He⁺ is $1.260 - 1.20 = +0.060$ for $F_0 = 0.5$ and $1.325 - 1.20 = +0.125$ for $F_0 = 1.0$, while the PES peak shift of $|2o\rangle$ He⁺ is $1.025 - 1.10 = -0.075$ for $F_0 = 0.5$ and $0.915 - 1.10 = -0.185$ for $F_0 = 1.0$, which agree well with results obtained in the Floquet formalism. Thus for the considered long-pulse interaction, the ac Stark effects in step 2 of DI is shown to be perfectly described by the Floquet theory for He⁺. The investigation of the ac Stark effects in step 1 of DI requires, however, constructing the Floquet Hamiltonian in the two-electron Hilbert space of both bound and continuum states, which is a formidable task for numerical simulations due to the huge size of the Floquet Hamiltonian matrix.

D. Nonsequential two-photon DI

Since the two-photon DI process contains the nonsequential mechanism only, an integral of the DI JES along the diagonal line $E_1 + E_2 = 2\omega - I_p^{\text{DI}}$ in the JES describes the nonsequential two-photon DI probability. For laser pulses with

fixed $\omega = 1.60$, $N_c = 200$, but different field strengths, we estimate this nonsequential two-photon DI probability $P_{\text{NS-2ph}}$ by computing the integral along the diagonal line $E_1 + E_2 = 2\omega - I_p^{\text{DI}}$ within a finite energy range (much smaller than the laser frequency but much larger than the FWHM in the frequency domain for the considered laser pulse),

$$P_{\text{NS-2ph}} = \iint_{|E_1+E_2-2\omega+I_p^{\text{DI}}|<0.1\omega} S_{\text{DI}}(E_1, E_2) dE_1 dE_2, \quad (21)$$

and compare it with the total DI probability

$$P_{\text{DI}} = \iint S_{\text{DI}}(E_1, E_2) dE_1 dE_2, \quad (22)$$

by taking the ratio $P_{\text{NS-2ph}}/P_{\text{DI}}$. The results are presented in Fig. 4. The nonsequential two-photon DI process is found to dominate the DI at low-field strength (e.g., $F_0 = 0.1$) and the ratio $P_{\text{NS-2ph}}/P_{\text{DI}}$ decreases dramatically with increasing field strength F_0 . This indicates that the multiphoton DI processes, especially the sequential mechanism [see the JES in Figs. 3(a) and 3(d)], contributes more and more to the DI yield with increasing field strength.

This finding can be qualitatively described by rate equations, which have been successfully applied to study multiphoton multielectron ionization by strong XUV lasers [44–47]. For the considered laser parameters, we may consider only some representative processes: the nonsequential two-photon DI, the sequential three-photon DI via the ground-state and first-excited-state ionic channels. Then the rate equations for the populations of the ground-state He (N_0), the ground-state He⁺ ($N_{\text{SI}}^{(1)}$), the first-excited-state He⁺ ($N_{\text{SI}}^{(2)}$), the He⁺⁺ produced by the nonsequential two-photon DI ($N_{\text{DI-2ph}}$), and the He⁺⁺ produced by the sequential three-photon DI ($N_{\text{DI-3ph}}$) are

$$\partial_t N_0 = [-R_{\text{DI-2ph}} - R_{\text{SI-1ph}}^{(1)} - R_{\text{SI-2ph}}^{(2)}] N_0, \quad (23)$$

$$\partial_t N_{\text{SI}}^{(1)} = R_{\text{SI-1ph}}^{(1)} N_0 - R_{\text{2ph}}^{(1)} N_{\text{SI}}^{(1)}, \quad (24)$$

$$\partial_t N_{\text{SI}}^{(2)} = R_{\text{SI-2ph}}^{(2)} N_0 - R_{\text{1ph}}^{(2)} N_{\text{SI}}^{(2)}, \quad (25)$$

$$\partial_t N_{\text{DI-2ph}} = R_{\text{DI-2ph}} N_0, \quad (26)$$

$$\partial_t N_{\text{DI-3ph}} = R_{\text{2ph}}^{(1)} N_{\text{SI}}^{(1)} + R_{\text{1ph}}^{(2)} N_{\text{SI}}^{(2)}, \quad (27)$$

where $R_{\text{DI-2ph}}$ is the rate of the nonsequential two-photon DI, $R_{\text{SI-}k\text{ph}}^{(j)}$ is the rate of the k -photon SI from He to the j th-state He⁺, $R_{k\text{ph}}^{(j)}$ is the rate of the k -photon ionization from the j th-state He⁺ to He⁺⁺. In general, a rate in a k -photon ionization process $R_{k\text{ph}}$ can be written as $R_{k\text{ph}} = \sigma_{k\text{ph}}(I/\omega)^k$, where $\sigma_{k\text{ph}}$ is the corresponding cross section and (I/ω) is the photon flux (in atomic units). Here we assume that the laser intensity I follows the pulse envelope, therefore all the rates are time dependent [48].

Instead of calculating the cross sections in our model, we may qualitatively consider their orders of magnitude in the rate equations. For example, in the numerical simulations of Eqs. (23)–(27) for laser pulses with fixed $\omega = 1.60$ and $N_c = 200$, we use $\sigma_{\text{1ph}} = 3.6 \times 10^{-2}$ (corresponding to 10^{-18} cm²) for all the one-photon processes and $\sigma_{\text{2ph}} = 5.3 \times 10^{-4}$ (corresponding to 10^{-53} cm⁴ s) for all the two-photon processes

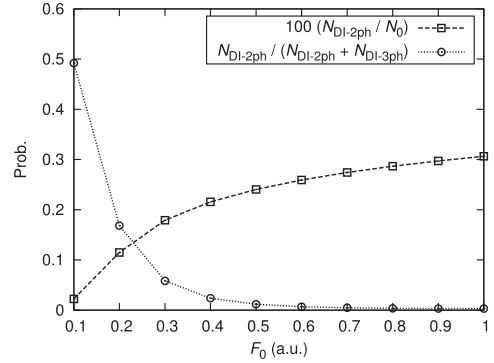


FIG. 5. The nonsequential two-photon DI probability $N_{\text{DI-2ph}}/N_0$ (multiplied by a factor of 100) and the ratio $N_{\text{DI-2ph}}/(N_{\text{DI-2ph}} + N_{\text{DI-3ph}})$ based on the rate equations [see Eqs. (23)–(27)] vs field strength F_0 , for fixed $\omega = 1.60$ and $N_c = 200$.

[47–51]. With the initial condition that only the ground state He is populated in the beginning, we numerically solve Eqs. (23)–(27) for different laser field strengths, and obtain the nonsequential two-photon DI probability $N_{\text{DI-2ph}}/N_0$ and the ratio $N_{\text{DI-2ph}}/(N_{\text{DI-2ph}} + N_{\text{DI-3ph}})$. As plotted in Fig. 5, the results based on the rate equations qualitatively agree with the results obtained from the TDSE (Fig. 4). Note that we use the rate equations for qualitative analyses, describing the competition between the sequential and nonsequential DI processes. Varying the chosen values of the cross sections can affect the calculated solutions of rate equations. For typical orders of magnitude of the cross sections, however, the qualitative conclusion remains unchanged, i.e., the sequential three-photon DI contributes much more than the nonsequential two-photon DI at high laser intensities.

E. JES at other laser frequencies

In Fig. 3, the ac Stark effects are mainly observed in the sequential DI via the $|1e\rangle$ and $|2o\rangle$ ionic channels, and the laser frequency ($\omega = 1.60$) is close to the resonance between the $|1e\rangle$ and $|2o\rangle$ He⁺ ($I_p^{(1)} - I_p^{(2)} = 1.50$). In closing this section, we briefly demonstrate the ac Stark effects in other ionic channels for different laser frequencies. To this end, we perform calculations at fixed field strength $F_0 = 1.0$ for laser frequencies $\omega = 1.80$ and $\omega = 1.90$, which are close to the resonance between $|1e\rangle$ and $|4o\rangle$ He⁺ in our 1D model ($I_p^{(1)} - I_p^{(4)} = 1.86$). The results are presented in Fig. 6.

In addition to the sequential DI via the $|1e\rangle$ and $|2o\rangle$ ionic channels, the sequential DI via the $|4o\rangle$ ionic channel is observed to be affected by the ac Stark shifts. Here we focus on the ac Stark effect in the He⁺ $|4o\rangle$ channel. Comparing the computed spectra with the expected energy values without considering the ac Stark effects (the horizontal black dotted lines in Fig. 6), we find that the ac Stark shift of the $|4o\rangle$ He⁺ ionization potential causes an increase of E_2 for $\omega = 1.80$ but a decrease of E_2 for $\omega = 1.90$. As mentioned in the above discussion, the ac Stark effects in step 1 and step 2 in the

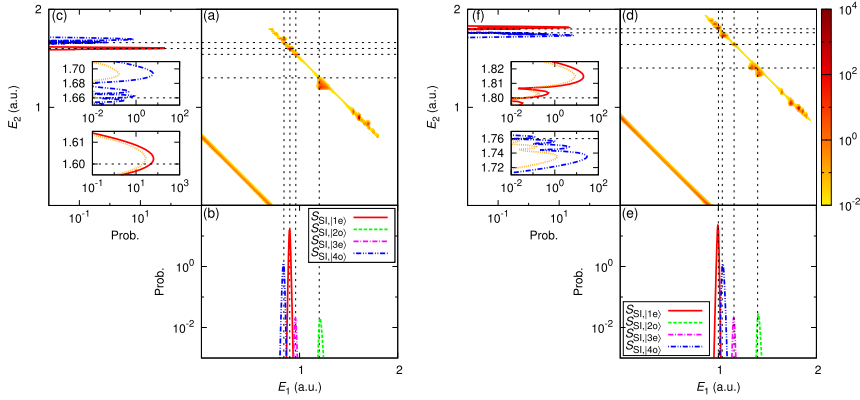


FIG. 6. Similar to Fig. 3, for fixed $F_0 = 1.0$ and $N_c = 200$. The laser frequencies are (a)–(c) $\omega = 1.80$ and (d)–(f) $\omega = 1.90$. Instead of the PES of the $|2o\rangle$ He^+ in Figs. 3(c) and 3(f), here the PES of the $|4o\rangle$ He^+ (blue dot-dot-dashed line) is plotted in (c) and (f). Insets in (c) and (f): zoom-ins of the PES peaks, for clear observation of the peak shifts. The DI JES integrated along E_1 , $\int S_{\text{DI}}(E_1, E_2) dE_1$ (orange dotted line) are also plotted in the insets in (c) and (f) for comparison. The maxima in the DI JES are (a) $S_{\text{DI}}(E_1 = 0.899, E_2 = 1.603) = S_{\text{DI}}(E_1 = 1.603, E_2 = 0.899) = 1.94 \times 10^3$ and (d) $S_{\text{DI}}(E_1 = 0.995, E_2 = 1.815) = S_{\text{DI}}(E_1 = 1.815, E_2 = 0.995) = 5.65 \times 10^2$, respectively.

sequential DI can be separately illustrated with the SI PES of He and the PES of He^+ , which is also the case in Fig. 6. We compare the PES of He^+ in the selected states with the DI JES integrated along E_1 , $\int S_{\text{DI}}(E_1, E_2) dE_1$ in the insets in Figs. 6(c) and 6(f). Similar to Fig. 3, the peak shifts in the one-electron spectra of He^+ are found to agree well with those in step 2 of the sequential DI.

Again, by diagonalizing the complex-scaled Floquet Hamiltonian of He^+ for $\omega = 1.80$ and $\omega = 1.90$ (at fixed $F_0 = 1.0$), we find that the ac Stark shift of the $|1e\rangle$ He^+ ionization potential $I_p^{(1)}$ is -0.003 for $\omega = 1.80$ and -0.016 for $\omega = 1.90$ while the ac Stark shift of the $|4o\rangle$ He^+ ionization potential $I_p^{(4)}$ is -0.037 for $\omega = 1.80$ and $+0.028$ for $\omega = 1.90$, which are in good agreement with the PES peak shifts observed from the insets in Figs. 6(c) and 6(f). The ac Stark shift of $I_p^{(4)}$ has opposite signs for $\omega = 1.80$ and $\omega = 1.90$, and therefore the direction of the ac Stark shift can to some extent be controlled by the laser frequency.

IV. CONCLUSION AND OUTLOOK

We studied the DI of He by intense XUV laser pulses by solving the TDSE and extracting the PES. We considered a frequency regime where the nonsequential two-photon DI is expected to dominate over the DI process according to perturbation theory, and performed calculations in the nonperturbative regime. In multiphoton DI, the sequential and nonsequential mechanisms can be identified from the JES of two electrons. We found that the sequential multiphoton DI shows remarkable peaks in the JES and these peaks spread their widths with increasing laser field strength due to the ac Stark effects. We also found that the ac Stark shifts in the sequential channels obtained from solving the two-electron TDSE could

be explained by considering the Stark shifts in the ion. In the strong-field regime, the ac Stark effects of many different ionic states can therefore be observed directly from the sequential multiphoton features via different ionic channels in the JES and the ac Stark shifts can be controlled by the laser frequency. The nonsequential mechanism was found to dominate the DI only at low-field strengths while the sequential multiphoton mechanism can contribute substantially at high-field strengths, which agree with qualitative estimates from rate equations. We propose shifts of peaks in the JES as described here, as clear experimental signatures of nonperturbative dynamics induced by intense XUV laser pulses.

In closing, we would like to briefly discuss the feasibility of experiments for the considered laser parameters. Recent advances in free-electron laser (FEL) technology has made experimental research on strong-field ionization in the XUV regime possible. The FEL radiation with a broad photon energy range and extremely high intensities has opened a different avenue of atomic and molecular physics [52]. For example, with the free-electron laser in Hamburg (FLASH) [2], the production of femtosecond XUV laser pulses with intensities greater than 10^{17} W/cm² has been reported [53]. We are therefore convinced that the photon energies, pulse durations, and peak intensities considered in this paper are experimentally available with state-of-the-art high-power lasers.

ACKNOWLEDGMENTS

This work was supported by the European Research Council StG (Project No. 277767-TDMET), and the VKR center of excellence, QUSCOPE. The numerical results presented in this work were obtained at the Centre for Scientific Computing, Aarhus.

- [1] T. Sekikawa, A. Kosuge, T. Kanai, and S. Watanabe, Nonlinear optics in the extreme ultraviolet, *Nature (London)* **432**, 605 (2004).
- [2] W. Ackermann, G. Asova, V. Ayvazyan, A. Azima, N. Baboi, J. Bähr, V. Balandin, B. Beutner, A. Brandt, A. Bolzmann *et al.*, Operation of a free-electron laser from the extreme ultraviolet to the water window, *Nat. Photon.* **1**, 336 (2007).
- [3] B. W. McNeil and N. R. Thompson, X-ray free-electron lasers, *Nat. Photon.* **4**, 814 (2010).
- [4] Y. Nabekawa, H. Hasegawa, E. J. Takahashi, and K. Midorikawa, Production of Doubly Charged Helium Ions by Two-Photon Absorption of an Intense sub-10-fs Soft x-ray Pulse at 42 eV Photon Energy, *Phys. Rev. Lett.* **94**, 043001 (2005).
- [5] H. Hasegawa, E. J. Takahashi, Y. Nabekawa, K. L. Ishikawa, and K. Midorikawa, Multiphoton ionization of He by using intense high-order harmonics in the soft-x-ray region, *Phys. Rev. A* **71**, 023407 (2005).
- [6] R. Moshhammer, Y. H. Jiang, L. Foucar, A. Rudenko, T. Ergler, C. D. Schröter, S. Lüdemann, K. Zrost, D. Fischer, J. Titze, T. Jahnke, M. Schöffler, T. Weber, R. Dörner, T. J. M. Zouros, A. Dorn, T. Ferger, K. U. Kühnel, S. Düsterer, R. Treusch, P. Radcliffe, E. Plönjes, and J. Ullrich, Few-Photon Multiple Ionization of Ne and Ar by Strong Free-Electron-Laser Pulses, *Phys. Rev. Lett.* **98**, 203001 (2007).
- [7] A. A. Sorokin, M. Wellhöfer, S. V. Bobashev, K. Tiedtke, and M. Richter, X-ray-laser interaction with matter and the role of multiphoton ionization: Free-electron-laser studies on neon and helium, *Phys. Rev. A* **75**, 051402 (2007).
- [8] A. Rudenko, L. Foucar, M. Kurka, T. Ergler, K. U. Kühnel, Y. H. Jiang, A. Voitkiv, B. Najjari, A. Kheifets, S. Lüdemann, T. Havermeier, M. Smolarski, S. Schössler, K. Cole, M. Schöffler, R. Dörner, S. Düsterer, W. Li, B. Keitel, R. Treusch, M. Gensch, C. D. Schröter, R. Moshhammer, and J. Ullrich, Recoil-ion Momentum Distributions for Two-Photon Double Ionization of He and Ne by 44 eV Free-Electron Laser Radiation, *Phys. Rev. Lett.* **101**, 073003 (2008).
- [9] P. Antoine, E. Fomouou, B. Piroux, T. Shimizu, H. Hasegawa, Y. Nabekawa, and K. Midorikawa, Two-photon double ionization of helium: An experimental lower bound of the total cross section, *Phys. Rev. A* **78**, 023415 (2008).
- [10] J. Feist, S. Nagele, R. Pazourek, E. Persson, B. I. Schneider, L. A. Collins, and J. Burgdörfer, Nonsequential two-photon double ionization of helium, *Phys. Rev. A* **77**, 043420 (2008).
- [11] I. A. Ivanov and A. S. Kheifets, Angular anisotropy parameters for sequential two-photon double ionization of helium, *Phys. Rev. A* **79**, 023409 (2009).
- [12] J. Feist, S. Nagele, R. Pazourek, E. Persson, B. I. Schneider, L. A. Collins, and J. Burgdörfer, Probing Electron Correlation via Attosecond xuv Pulses in the Two-Photon Double Ionization of Helium, *Phys. Rev. Lett.* **103**, 063002 (2009).
- [13] Z. Zhang, L.-Y. Peng, M.-H. Xu, A. F. Starace, T. Morishita, and Q. Gong, Two-photon double ionization of helium: Evolution of the joint angular distribution with photon energy and two-electron energy sharing, *Phys. Rev. A* **84**, 043409 (2011).
- [14] R. Pazourek, J. Feist, S. Nagele, E. Persson, B. I. Schneider, L. A. Collins, and J. Burgdörfer, Universal features in sequential and nonsequential two-photon double ionization of helium, *Phys. Rev. A* **83**, 053418 (2011).
- [15] S. Selstø, X. Raynaud, A. S. Simonsen, and M. Førre, Distinction between sequential and direct ionization in two-photon double ionization of helium, *Phys. Rev. A* **90**, 053412 (2014).
- [16] F. L. Yip, A. Palacios, F. Martín, T. N. Rescigno, and C. W. McCurdy, Two-photon double ionization of atomic beryllium with ultrashort laser pulses, *Phys. Rev. A* **92**, 053404 (2015).
- [17] W.-C. Jiang, J.-Y. Shan, Q. Gong, and L.-Y. Peng, Virtual Sequential Picture for Nonsequential Two-Photon Double Ionization of Helium, *Phys. Rev. Lett.* **115**, 153002 (2015).
- [18] A. Liu and U. Thumm, Criterion for Distinguishing Sequential from Nonsequential Contributions to the Double Ionization of Helium in Ultrashort Extreme-Ultraviolet Pulses, *Phys. Rev. Lett.* **115**, 183002 (2015).
- [19] J. S. Parker, B. J. S. Doherty, K. T. Taylor, K. D. Schultz, C. I. Blaga, and L. F. DiMauro, High-Energy Cutoff in the Spectrum of Strong-Field Nonsequential Double Ionization, *Phys. Rev. Lett.* **96**, 133001 (2006).
- [20] A. Staudte, C. Ruiz, M. Schöffler, S. Schössler, D. Zeidler, T. Weber, M. Meckel, D. M. Villeneuve, P. B. Corkum, A. Becker, and R. Dörner, Binary and Recoil Collisions in Strong Field Double Ionization of Helium, *Phys. Rev. Lett.* **99**, 263002 (2007).
- [21] A. Rudenko, V. L. B. de Jesus, T. Ergler, K. Zrost, B. Feuerstein, C. D. Schröter, R. Moshhammer, and J. Ullrich, Correlated Two-Electron Momentum Spectra for Strong-Field Nonsequential Double Ionization of He at 800 nm, *Phys. Rev. Lett.* **99**, 263003 (2007).
- [22] D. F. Ye, X. Liu, and J. Liu, Classical Trajectory Diagnosis of a Fingerlike Pattern in the Correlated Electron Momentum Distribution in Strong Field Double Ionization of Helium, *Phys. Rev. Lett.* **101**, 233003 (2008).
- [23] Z. Zhang, L.-Y. Peng, Q. Gong, and T. Morishita, Momentum space analysis of multiphoton double ionization of helium by intense attosecond xuv pulses, *Opt. Express* **18**, 8976 (2010).
- [24] J. S. Parker, L. R. Moore, K. J. Meharg, D. Dundas, and K. T. Taylor, Double-electron above threshold ionization of helium, *J. Phys. B* **34**, L69 (2001).
- [25] C. B. Madsen, F. Anis, L. B. Madsen, and B. D. Esry, Multiphoton Above Threshold Effects in Strong-Field Fragmentation, *Phys. Rev. Lett.* **109**, 163003 (2012).
- [26] R. E. F. Silva, F. Catoire, P. Rivière, H. Bachau, and F. Martín, Correlated Electron and Nuclear Dynamics in Strong Field Photoionization of H_2^+ , *Phys. Rev. Lett.* **110**, 113001 (2013).
- [27] J. Wu, M. Kunitski, M. Pitzer, F. Trinter, L. P. H. Schmidt, T. Jahnke, M. Magrakvelidze, C. B. Madsen, L. B. Madsen, U. Thumm, and R. Dörner, Electron-Nuclear Energy Sharing in Above-Threshold Multiphoton Dissociative Ionization of H_2 , *Phys. Rev. Lett.* **111**, 023002 (2013).
- [28] M. Lein, E. K. U. Gross, and V. Engel, Discrete peaks in above-threshold double-ionization spectra, *Phys. Rev. A* **64**, 023406 (2001).
- [29] K. Henrichs, M. Waitz, F. Trinter, H. Kim, A. Menssen, H. Gassert, H. Sann, T. Jahnke, J. Wu, M. Pitzer, M. Richter, M. S. Schöffler, M. Kunitski, and R. Dörner, Observation of Electron Energy Discretization in Strong Field Double Ionization, *Phys. Rev. Lett.* **111**, 113003 (2013).

- [30] X. Gong, Q. Song, Q. Ji, K. Lin, H. Pan, J. Ding, H. Zeng, and J. Wu, Channel-Resolved Above-Threshold Double Ionization of Acetylene, *Phys. Rev. Lett.* **114**, 163001 (2015).
- [31] P. V. Demekhin and L. S. Cederbaum, Dynamic Interference of Photoelectrons Produced by High-Frequency Laser Pulses, *Phys. Rev. Lett.* **108**, 253001 (2012).
- [32] P. V. Demekhin and L. S. Cederbaum, ac stark effect in the electronic continuum and its impact on the photoionization of atoms by coherent intense short high-frequency laser pulses, *Phys. Rev. A* **88**, 043414 (2013).
- [33] S. B. Zhang and N. Rohringer, Photoemission spectroscopy with high-intensity short-wavelength lasers, *Phys. Rev. A* **89**, 013407 (2014).
- [34] A. N. Artemyev, A. D. Müller, D. Hochstuhl, L. S. Cederbaum, and P. V. Demekhin, Dynamic interference in the photoionization of He by coherent intense high-frequency laser pulses: Direct propagation of the two-electron wave packets on large spatial grids, *Phys. Rev. A* **93**, 043418 (2016).
- [35] C. Yu and L. B. Madsen, Ionization of helium by intense xuv laser pulses: Numerical simulations on channel-resolved probabilities, *Phys. Rev. A* **93**, 043412 (2016).
- [36] L. Tao and A. Scrinzi, Photo-electron momentum spectra from minimal volumes: The time-dependent surface flux method, *New J. Phys.* **14**, 013021 (2012).
- [37] A. Scrinzi, *t*-SURFF: Fully differential two-electron photoemission spectra, *New J. Phys.* **14**, 085008 (2012).
- [38] L. Yue and L. B. Madsen, Dissociation and dissociative ionization of H_2^+ using the time-dependent surface flux method, *Phys. Rev. A* **88**, 063420 (2013).
- [39] A. Karamatskou, S. Pabst, Y.-J. Chen, and R. Santra, Calculation of photoelectron spectra within the time-dependent configuration-interaction singles scheme, *Phys. Rev. A* **89**, 033415 (2014).
- [40] A. Zielinski, V. P. Majety, and A. Scrinzi, Double photoelectron momentum spectra of helium at infrared wavelength, *Phys. Rev. A* **93**, 023406 (2016).
- [41] J. Muga, J. Palao, B. Navarro, and I. Egusquiza, Complex absorbing potentials, *Phys. Rep.* **395**, 357 (2004).
- [42] S.-I. Chu and D. A. Telnov, Beyond the floquet theorem: Generalized floquet formalisms and quasienergy methods for atomic and molecular multiphoton processes in intense laser fields, *Phys. Rep.* **390**, 1 (2004).
- [43] C. J. Joachain, N. J. Kylstra, and R. M. Potvliege, *Atoms in Intense Laser Fields* (Cambridge University Press, Cambridge, UK, 2012).
- [44] M. G. Makris and P. Lambropoulos, Theoretical interpretation of multiphoton ionization of neon by soft-x-ray intense radiation, *Phys. Rev. A* **77**, 023401 (2008).
- [45] M. G. Makris, P. Lambropoulos, and A. Mihelić, Theory of Multiphoton Multielectron Ionization of Xenon Under Strong 93-eV Radiation, *Phys. Rev. Lett.* **102**, 033002 (2009).
- [46] N. Gerken, S. Klumpp, A. A. Sorokin, K. Tiedtke, M. Richter, V. Bürk, K. Mertens, P. Juranić, and M. Martins, Time-dependent Multiphoton Ionization of Xenon in the Soft-x-ray Regime, *Phys. Rev. Lett.* **112**, 213002 (2014).
- [47] M. Ilchen, T. Mazza, E. T. Karamatskos, D. Markellos, S. Bakhtiarzadeh, A. J. Rafipoor, T. J. Kelly, N. Walsh, J. T. Costello, P. O'Keeffe, N. Gerken, M. Martins, P. Lambropoulos, and M. Meyer, Two-electron processes in multiple ionization under strong soft-x-ray radiation, *Phys. Rev. A* **94**, 013413 (2016).
- [48] P. Lambropoulos and X. Tang, Multiple excitation and ionization of atoms by strong lasers, *J. Opt. Soc. Am. B* **4**, 821 (1987).
- [49] R. Shakeshaft, Two-photon single and double ionization of helium, *Phys. Rev. A* **76**, 063405 (2007).
- [50] D. A. Horner, F. Morales, T. N. Rescigno, F. Martín, and C. W. McCurdy, Two-photon double ionization of helium above and below the threshold for sequential ionization, *Phys. Rev. A* **76**, 030701 (2007).
- [51] A. Palacios, T. N. Rescigno, and C. W. McCurdy, Cross sections for short-pulse single and double ionization of helium, *Phys. Rev. A* **77**, 032716 (2008).
- [52] J. Ullrich, A. Rudenko, and R. Moshhammer, Free-electron lasers: New avenues in molecular physics and photochemistry, *Annu. Rev. Phys. Chem.* **63**, 635 (2012).
- [53] J. Andreasson, B. Iwan, A. Andrejczuk, E. Abreu, M. Bergh, C. Caleman, A. J. Nelson, S. Bajt, J. Chalupsky, H. N. Chapman, R. R. Fäustlin, V. Hajkova, P. A. Heimann, B. Hjärvarsson, L. Juha, D. Klinger, J. Krzywinski, B. Nagler, G. K. Pálsson, W. Singer, M. M. Seibert, R. Sobierajski, S. Toleikis, T. Tschentscher, S. M. Vinko, R. W. Lee, J. Hajdu, and N. Timneanu, Saturated ablation in metal hydrides and acceleration of protons and deuterons to keV energies with a soft-x-ray laser, *Phys. Rev. E* **83**, 016403 (2011).

Paper III. Physical Review A 95, 063407 (2017)

Title:

**Above-threshold ionization of helium in the long-wavelength regime:
Examining the single-active-electron approximation and the two-electron strong-field approximation**

Authors: Chuan Yu and Lars Bojer Madsen

DOI: <https://doi.org/10.1103/PhysRevA.95.063407>

Reprinted with permission from the American Physical Society.
Copyright (2017) by the American Physical Society.

My contribution to this publication includes (1) implementation of the theoretical calculations and (2) preparation of the manuscript (with figures).

PHYSICAL REVIEW A 95, 063407 (2017)

Above-threshold ionization of helium in the long-wavelength regime: Examining the single-active-electron approximation and the two-electron strong-field approximation

Chuan Yu and Lars Bojer Madsen

Department of Physics and Astronomy, Aarhus University, DK-8000 Aarhus C, Denmark

(Received 4 May 2017; published 8 June 2017)

We investigate high-order above-threshold ionization of model helium in the long-wavelength regime up to 2400 nm by solving the two-electron time-dependent Schrödinger equation in one dimension. To bypass the difficulty of solving the multielectron time-dependent Schrödinger equation with the long-wavelength laser interaction, we revisit and examine two typically used theoretical methods: the single-active-electron approximation and the strong-field approximation. For the description of the high-energy rescattered electrons in the ground-state ionic channel, the single-active-electron approximation performs better with increasing ponderomotive energy. Single ionization in the excited-state ionic channels, in general, has much weaker spectral intensity than that in the ground-state ionic channel. The above-threshold-ionization cutoffs in the excited-state ionic channels are clear signatures of two-electron dynamics, which cannot be explained within the single-active-electron approximation. By applying the two-electron strong-field approximation including rescattering and a saddle-point method analysis, we explain the channel-resolved cutoffs, and relate them to elastic and inelastic rescattering processes.

DOI: [10.1103/PhysRevA.95.063407](https://doi.org/10.1103/PhysRevA.95.063407)

I. INTRODUCTION

Above-threshold ionization (ATI) of atoms and molecules, in which more photons than the minimum required for ionization are absorbed from the laser field, is one of the most fundamental phenomena in strong-field physics. Since the first experimental observation of ATI [1], numerous studies have been performed to explore the ATI spectral features (see, e.g., Refs. [2–4] for reviews). When irradiated by an intense laser field, a bound electron may be freed, drift away, and contribute to the low-energy part of the ATI spectrum (typically below $2U_p$, where U_p is the ponderomotive energy). Alternatively it may be driven back to the ion by the laser field and rescatter. The backscattered electrons gain more energy than the direct electrons and contribute to the plateau-like high-energy part of the ATI spectrum, typically ranging from $2U_p$ to $10U_p$. The high-energy region of the ATI spectrum is found to be particularly sensitive to the structure of the target ion, allowing for imaging applications. For example, laser-induced electron diffraction (LIED) [5] is a time-resolved molecular self-imaging technique based on extracting structural information from strong-field-induced rescattering.

Recent development of intense few-cycle light sources with long wavelengths, e.g., in the mid-infrared regime, opens a new avenue of strong-field physics [6]. With long-wavelength laser pulses used in the LIED, one can produce very high energy rescattered electrons for imaging ultrafast molecular dynamics, with femtosecond and subangstrom resolution [7–9]. Although strong-field ionization in the long-wavelength regime is promising in experimental research, the corresponding numerical simulations are very challenging. The difficulties of solving the time-dependent Schrödinger equation (TDSE) in the long-wavelength regime come not only from the involvement of many angular momentum states but also from the large quiver radius that is proportional to the wavelength squared. It is, hence, a formidable task to simulate multielectron dynamics in the long-wavelength regime. So a question arises: what theoretical methods other than full

TDSE calculations are useful for studying the long-wavelength laser interaction with multielectron systems? In this paper, we discuss this question by examining the single-active-electron approximation (SAEA) and the two-electron strong-field approximation (SFA) including rescattering. We focus on the high-energy part of the ATI spectrum, which can be used for high-resolution imaging with the LIED technique.

The SAEA assumes that only one electron is bound by an effective potential and interacts with the laser field. However, the validity of the SAEA in few-electron systems still remains not fully investigated. In the long-wavelength regime, it is particularly difficult to examine the validity of the SAEA, since *ab initio* calculations beyond the SAEA are extremely demanding. To overcome this difficulty, we consider a one-dimensional (1D) model of helium in the presence of linearly polarized infrared laser fields, and the maximum wavelength considered is 2400 nm. For such a long wavelength, single ionization (SI) is dominant. We compute the SI spectra in different ionic channels corresponding to different final states of He^+ , and compare them with the ATI spectra obtained within the SAEA. In the long-wavelength regime, or the strong-field regime with large U_p , the SAEA is found to be applicable for describing the high-order ATI in the lowest ionic channel, which is the dominant SI channel. To some extent, this validates the commonly used single-active-electron model.

In the two-electron TDSE calculations, however, there also exist two-electron effects even in the SI channels, which cannot be described within the SAEA. The channel-resolved ATI spectra, especially those in the excited-state ionic channels, contain clear two-electron features. To investigate the two-electron features and the corresponding physical processes, one needs theoretical methods beyond the SAEA. The SFA, also known as the Keldysh-Faisal-Reiss theory [10–12], and its modified versions have been extensively applied to investigate both one-electron and two-electron dynamics (see, e.g., Refs. [13–25]). To our knowledge, the SFA has not been applied for the description of the channel-resolved high-order ATI spectra. In this paper, we formulate the two-electron

SFA including rescattering for the channel-resolved ATI of helium and apply the saddle-point method (SPM) to analyze the spectral cutoffs. As we will show, the SFA and the SPM enable us to qualitatively explain the channel-resolved ATI cutoffs, and to relate them to elastic and inelastic rescattering processes. In this sense the SFA is a useful tool for qualitative studies of the strong-field ionization in the long-wavelength regime and for gaining physical insight about the relevant processes.

This paper is organized as follows. In Sec. II, we introduce the theoretical models and numerical methods used in the TDSE calculations, and formulate the SAEA and the SFA for our model. In Sec. III we present and discuss the results of the calculations. Finally we give concluding remarks in Sec. IV. Atomic units are used throughout unless stated otherwise.

II. THEORETICAL MODELS AND METHODS

A. TDSE of the 1D helium model

We solve the TDSE of the widely used 1D two-electron model [26–28]

$$i\partial_t\Psi(x_1, x_2, t) = H(t)\Psi(x_1, x_2, t), \quad (1)$$

with the Hamiltonian

$$H(t) = \sum_{j=1}^2 \left\{ \frac{[p_j + A(t)]^2}{2} + V_{\text{en}}(x_j) \right\} + V_{\text{ee}}(x_1, x_2). \quad (2)$$

Here x_j and $p_j = -i\partial_{x_j}$ ($j = 1, 2$) are the electron coordinate and momentum operators, respectively;

$$V_{\text{en}}(x_j) = \frac{-2}{\sqrt{x_j^2 + 1}}, \quad (j = 1, 2), \quad (3)$$

$$V_{\text{ee}}(x_1, x_2) = \frac{1}{\sqrt{(x_1 - x_2)^2 + 1}} \quad (4)$$

are the electron-nucleus and the electron-electron interactions, which are softened to avoid the Coulomb singularity. The laser interaction is described in velocity gauge by the vector potential $A(t)$ within the dipole approximation. In our calculations, a vector potential with the sine-squared envelope is used:

$$A(t) = \begin{cases} -\frac{F_0}{\omega} \sin^2\left(\frac{\omega t}{2N_c}\right) \cos(\omega t), & 0 < t < \frac{2\pi N_c}{\omega}, \\ 0, & \text{else,} \end{cases} \quad (5)$$

where F_0 is the maximum field strength related to the peak intensity I (in units of W/cm^2) by $F_0 = \sqrt{I/(3.509 \times 10^{16})}$, ω is the angular frequency, and N_c is the number of cycles. We consider $N_c = 2$ to shorten the simulation time. For a laser pulse with a wavelength of 2400 nm and a peak intensity of $8 \times 10^{13} \text{ W}/\text{cm}^2$, the electron quiver radius is $\alpha_0 = F_0/\omega^2 \approx 132$, which is the largest quiver radius considered in this work.

When numerically solving the TDSE, we discretize the simulation volume by employing a finite-element discrete variable representation (FEDVR) [29] combined with infinite-range exterior complex scaling (irECS) [30]. The coordinate space is divided into inner and outer regions by a complex scaling radius r_c , which is chosen to be larger than the

quiver radius. For example, we choose $r_c = 150 > \alpha_0$ for the laser parameters $\lambda = 2400 \text{ nm}$ and $I = 8 \times 10^{13} \text{ W}/\text{cm}^2$. The inner region $[-r_c, r_c]$ is discretized by finite elements with a fixed equal size of 2 and 11 Gauss-Lobatto basis functions in each element. The outer regions $(-\infty, -r_c]$ and $[r_c, +\infty)$ are complex scaled with a scaling angle $\theta = 0.3$ and discretized by 100 basis functions (see Refs. [30,31] for details of the irECS method and the basis functions). The number of outer-region basis functions used in our work is larger than that used in Refs. [30,31], where the numerical calculations were performed for 800 nm only. For the long-wavelength regime (e.g., 1600 nm and 2400 nm), we find that more outer-region basis functions are needed for convergence than the typically ~ 40 needed for 800 nm calculations.

We propagate the TDSE with the Arnoldi-Lanczos time propagator [32,33] with a time step of $\Delta t = 0.001$. The initial wave function is obtained by imaginary-time propagation (ITP) [34]. For both the two-electron TDSE and the one-electron TDSE within the SAEA, we extract the ATI spectra (dP/dk , where k is the final momentum of the freed electron) by using the time-dependent surface flux (tSURFF) method [35–37] with the tSURFF surfaces placed at $x = \pm 55$. We emphasize that the irECS method works as an efficient absorber so that the wave function in the inner region remains accurate for applying the tSURFF method. For the TDSE within the SAEA, we perform reference calculations on a large grid without any absorber (a finite simulation box $[-10000, 10000]$ discretized by 10000 equal-size finite elements and 11 Gauss-Lobatto basis functions in each element). The convergence of the irECS method for the SAEA calculations is checked by comparison with the reference results. We apply the one-electron irECS parameters found by this convergence test also for the two-electron TDSE.

B. SAEA for the 1D helium model

Here we briefly introduce the SAEA used in this work (see also Ref. [38]). To find the effective potential, we first make the Hartree-Fock (HF) ansatz for the ground-state He wave function and apply ITP to the equation for the field-free single-electron orbital ψ_0 ,

$$i\partial_t\psi_0(x, t) = H_0(t)\psi_0(x, t), \quad (6)$$

with the Hamiltonian

$$H_0(t) = \frac{p^2}{2} + V_{\text{en}}(x) + \int dx' V_{\text{ee}}(x, x') |\psi_0(x', t)|^2. \quad (7)$$

The SAEA assumes that the inactive electron is “frozen” in the field-free single-electron orbital ψ_0 while the active electron feels the effective potential of the “frozen core”

$$V_{\text{eff}}(x) = V_{\text{en}}(x) + \int dx' V_{\text{ee}}(x, x') |\psi_0(x')|^2, \quad (8)$$

where the time dependence of ψ_0 is dropped since the distribution of the inactive electron $|\psi_0(x', t)|^2$ remains time-invariant. With the laser interaction taken into account, the TDSE for the active electron reads

$$i\partial_t\psi_1(x, t) = H_1(t)\psi_1(x, t), \quad (9)$$

ABOVE-THRESHOLD IONIZATION OF HELIUM IN THE ...

PHYSICAL REVIEW A 95, 063407 (2017)

where the SAEA Hamiltonian is

$$H_i(t) = \frac{[p + A(t)]^2}{2} + V_{\text{eff}}(x). \quad (10)$$

The ionization potential (I_p) obtained within the SAEA is 0.750, which is slightly smaller than I_p for the SI of the two-electron model (0.755), due to the HF ansatz made in the SAEA.

C. Two-electron SFA for the 1D helium model

The way in which we formulate the two-electron SFA including rescattering follows the intense-field many-body S -matrix theory (IMST) [39], which is a systematic method to calculate the transition amplitude from an initial state $\psi_i(t_i)$ to a final state $\psi_f(t_f)$, based on different partitions of the total Hamiltonian. The states $\psi_i(t)$ and $\psi_f(t)$ are solutions to the TDSE with the Hamiltonians $H_i(t)$ and $H_f(t)$, respectively. We have the initial- and final-state partitions of the total Hamiltonian $H(t) = H_i(t) + V_i(t) = H_f(t) + V_f(t)$. Instead of using Green's functions as in Ref. [39], we formulate the theory with time-evolution operators $U(t, t')$, $U_i(t, t')$, and $U_f(t, t')$, corresponding to $H(t)$, $H_i(t)$, and $H_f(t)$, respectively. The time-evolution operators solve the TDSEs

$$i \partial_t U(t, t') = H(t)U(t, t'), \quad (11)$$

$$i \partial_t U_i(t, t') = H_i(t)U_i(t, t'), \quad (12)$$

$$i \partial_t U_f(t, t') = H_f(t)U_f(t, t'), \quad (13)$$

and the total time-evolution operator $U(t, t')$ can be related to $U_i(t, t')$ and $U_f(t, t')$ by

$$U(t, t') = U_i(t, t') - i \int_{t'}^t dt_1 U(t, t_1) V_i(t_1) U_i(t_1, t'), \quad (14)$$

$$U(t, t') = U_f(t, t') - i \int_{t'}^t dt_1 U_f(t, t_1) V_f(t_1) U(t_1, t'). \quad (15)$$

Substituting Eq. (15) into Eq. (14) leads to

$$\begin{aligned} U(t, t') &= U_i(t, t') - i \int_{t'}^t dt_1 U_f(t, t_1) V_i(t_1) U_i(t_1, t') \\ &\quad - \int_{t'}^t dt_1 \int_{t_1}^t dt_2 U_f(t, t_2) V_f(t_2) U(t_2, t_1) \\ &\quad \times V_i(t_1) U_i(t_1, t'). \end{aligned} \quad (16)$$

By evolving the system from $\psi_i(t_i)$ and applying Eq. (16), we can evaluate the probability amplitude of finding the system in $\psi_f(t_f)$ as

$$\begin{aligned} &\langle \psi_f(t_f) | U(t_f, t_i) | \psi_i(t_i) \rangle \\ &= \langle \psi_f(t_f) | \psi_i(t_f) \rangle - i \int_{t_i}^{t_f} dt_1 \langle \psi_f(t_f) | V_i(t_1) | \psi_i(t_i) \rangle \\ &\quad - \int_{t_i}^{t_f} dt_1 \int_{t_1}^{t_f} dt_2 \langle \psi_f(t_f) | V_f(t_2) U(t_2, t_1) V_i(t_1) | \psi_i(t_i) \rangle, \end{aligned} \quad (17)$$

which is equivalent to the IMST expression [39].

In this work, the He ground state (denoted by $|g; t\rangle$ for time t) is considered as the initial state, so the initial-state partition of the total Hamiltonian is

$$H_i = \sum_{j=1}^2 \left[\frac{p_j^2}{2} + V_{\text{en}}(x_j) \right] + V_{\text{ec}}(x_1, x_2), \quad (18)$$

$$V_i = A(t)[p_1 + p_2 + A(t)]. \quad (19)$$

For the channel-resolved SI, we consider the single-continuum state as the final state. In the SFA, exact continuum states are approximated by Volkov states, so we use the product of the Volkov state and the bound ionic state for the channel-specific single-continuum state. Reserving the index 1 for the freed electron, we have the final-state partition of the total Hamiltonian

$$H_f = \frac{[p_1 + A(t)]^2}{2} + \frac{p_2^2}{2} + V_{\text{en}}(x_2), \quad (20)$$

$$V_f = A(t)[p_2 + A(t)/2] + V_{\text{en}}(x_1) + V_{\text{ec}}(x_1, x_2). \quad (21)$$

Now we introduce the notation $|k, n; t\rangle$ for the approximated single-continuum state (the product of the Volkov state and the bound ionic state) at time t , meaning that the freed electron has the canonical momentum k and the ion He^+ is in its n th state. Thus the time-evolution operator $U_f(t, t')$ can be expressed as

$$U_f(t, t') = \sum_n \int_{-\infty}^{+\infty} dk |k, n; t\rangle \langle k, n; t'|. \quad (22)$$

By approximating $\langle k, n; t | g; t' \rangle \approx 0$ and $U(t_2, t_1) \approx U_f(t_2, t_1)$ in Eq. (17), we obtain the two-electron SFA transition amplitude from the initial state $|g; t = -\infty\rangle$ to the final state $|k_f, n; t = +\infty\rangle$:

$$\begin{aligned} &T_{\text{SFA}}(k_f, n) \\ &= -i \int_{-\infty}^{+\infty} dt_1 \langle k_f, n; t_1 | V_i(t_1) | g; t_1 \rangle \\ &\quad - \sum_m \int_{-\infty}^{+\infty} dt_1 \int_{t_1}^{+\infty} dt_2 \int_{-\infty}^{+\infty} dk_i \langle k_f, n; t_2 | V_f(t_2) | k_i, m; t_2 \rangle \\ &\quad \times \langle k_i, m; t_1 | V_i(t_1) | g; t_1 \rangle. \end{aligned} \quad (23)$$

The spectral intensity is proportional to $|T_{\text{SFA}}(k_f, n)|^2$. For two-electron systems, the SFA has been extensively used in the studies of double ionization (see, e.g., Refs. [14, 17, 22–25]). In this work, we formulate the two-electron SFA [Eq. (23)] for the channel-resolved SI.

The physical meaning of Eq. (23) is clear: the first term describes the direct SI into the n th ionic channel via the laser interaction while the second term (sum) describes two-step processes leading to SI, including the rescattering. In the two-step processes, the first step, similar to the direct SI, is the SI (with intermediate momentum k_i) into the m th ionic channel induced by the laser interaction. The second step can be understood by investigating the three terms in Eq. (21): remember that the freed electron is denoted by the index 1, the first interaction $A(t_2)[p_2 + A(t_2)/2]$ can give a nonvanishing contribution only if $k_f = k_i$, describing a transition in the ion induced by the laser interaction; the second interaction $V_{\text{en}}(x_1)$ can give a nonvanishing contribution only if n and m are equal, describing an elastic rescattering of the freed electron via the

electron-nucleus interaction; the third interaction $V_{ec}(x_1, x_2)$ allows for state changes in both the freed and bound electrons, i.e., $k_i \rightarrow k_f$ and $m \rightarrow n$, including both elastic and inelastic rescattering processes via the electron-electron interaction.

Here we focus on the high-energy channel-resolved ATI cutoffs; therefore in the two-electron SFA we only study the terms that can contribute to the production of high-energy electrons, i.e., the terms corresponding to rescattering processes. For the high-energy part of the ATI spectra, Eq. (23) can be approximated by a sum of all the rescattering terms that result in the same final state $|k_f, n; t = +\infty\rangle$:

$$T_{\text{SFA}}^{m,n}(k_f, n) \approx \sum_m T_{\text{res}}^{m,n}(k_f), \quad (24)$$

where $T_{\text{res}}^{m,n}(k_f)$ is a unified notation for both the elastic ($m = n$) and inelastic ($m \neq n$) rescattering terms:

$$T_{\text{res}}^{m,n}(k_f) = - \int_{-\infty}^{+\infty} dt_1 \int_{t_1}^{+\infty} dt_2 \int_{-\infty}^{+\infty} dk_i \langle k_f, n; t_2 | V_{\text{res}} | k_i, m; t_2 \rangle \times \langle k_i, m; t_1 | V_i(t_1) | g; t_1 \rangle. \quad (25)$$

In Eq. (25) the notation V_{res} is used for both the elastic ($m = n$) and inelastic ($m \neq n$) rescattering interactions, which are time-independent:

$$V_{\text{res}}^{m,n} = \delta_{m,n} V_{\text{en}}(x_1) + V_{ec}(x_1, x_2). \quad (26)$$

With the He ground-state energy denoted by E_g and the n th (m th) ionic energy denoted by E_n (E_m), we introduce the two-electron Volkov phase

$$S_{k_f}^{m,n}(k_i, t_1, t_2) = \int_0^{t_2} dt \frac{[k_f + A(t)]^2}{2} - \int_{t_1}^{t_2} dt \frac{[k_i + A(t)]^2}{2} + (E_n - E_m)t_2 + (E_m - E_g)t_1, \quad (27)$$

and the form factor

$$W_{k_f}^{m,n}(k_i, t_1) = \langle k_f, n; 0 | V_{\text{res}}^{m,n} | k_i, m; 0 \rangle \times \langle k_i, m; 0 | V_i(t_1) | g; 0 \rangle. \quad (28)$$

Then Eq. (25) can be rewritten as

$$T_{\text{res}}^{m,n}(k_f) = - \int_{-\infty}^{+\infty} dt_1 \int_{t_1}^{+\infty} dt_2 \int_{-\infty}^{+\infty} dk_i \{ W_{k_f}^{m,n}(k_i, t_1) \times \exp[i S_{k_f}^{m,n}(k_i, t_1, t_2)] \}. \quad (29)$$

The SPM is applied to approximate the integral in Eq. (29) (see, e.g., Refs. [13,15,19] for discussion of the SFA and the SPM). First, we seek for solutions to the saddle-point equations

$$\frac{\partial S_{k_f}^{m,n}}{\partial k_i} = \frac{\partial S_{k_f}^{m,n}}{\partial t_1} = \frac{\partial S_{k_f}^{m,n}}{\partial t_2} = 0, \quad (30)$$

namely,

$$k_i(t_2 - t_1) + \int_{t_1}^{t_2} dt A(t) = 0, \quad (31)$$

$$\frac{[k_i + A(t_1)]^2}{2} + (E_m - E_g) = 0, \quad (32)$$

$$\frac{[k_f + A(t_2)]^2}{2} - \frac{[k_i + A(t_2)]^2}{2} + (E_n - E_m) = 0. \quad (33)$$

Equation (31) determines the intermediate momentum k_i while Eqs. (32) and (33) describe the energy conservation at the

ionization time t_1 and the rescattering time t_2 . The solutions are complex-valued and they come in pairs. We only consider the physically relevant solutions, with additional conditions $0 < \text{Re}(t_1) < \text{Re}(t_2) < 2\pi N_c/\omega$ and $\text{Im}(t_1) > 0$ imposed. The nonlinear Eqs. (31)–(33) are solved numerically with the Powell hybrid method.

Suppose that there are Q pairs of physically relevant solutions for any final momentum k_f . We introduce an index $s \in \{q+, q-\}$ ($q = 1, \dots, Q$) for the solutions $\{k_i^s, t_1^s, t_2^s\}$, and approximate Eq. (29) according to the SPM

$$T_{\text{res}}^{m,n}(k_f) \sim - \sum_s \{ W_{k_f}^{m,n}(k_i^s, t_1^s) \exp[i S_{k_f}^{m,n}(k_i^s, t_1^s, t_2^s)] \times [\Delta_{k_f}^{m,n}(k_i^s, t_1^s, t_2^s)]^{-1/2} (2\pi i)^{3/2} \}, \quad (34)$$

where $\{k_i^s, t_1^s, t_2^s\}$ are the solutions to Eqs. (31)–(33) and

$$\Delta_{k_f}^{m,n}(k_i, t_1, t_2) = \frac{\partial^2 S_{k_f}^{m,n}}{\partial k_i^2} \frac{\partial^2 S_{k_f}^{m,n}}{\partial t_1^2} \frac{\partial^2 S_{k_f}^{m,n}}{\partial t_2^2}. \quad (35)$$

The ATI cutoff energy is solely determined by the exponential term within the SPM. The SPM fails for electron energies near and beyond the cutoff; i.e., the pair of two solutions approach each other closely near the cutoff and one of them becomes unphysical after the cutoff. The contribution of the unphysical solution diverges as the energy $k_f^2/2 \rightarrow +\infty$ (see, e.g. Refs. [13,15,18]). To solve this problem, one can drop the unphysical solution for energies beyond the cutoff, or use the uniform approximation [15,19]. For a pair of solutions $\{k_i^{q+}, t_1^{q+}, t_2^{q+}\}$ and $\{k_i^{q-}, t_1^{q-}, t_2^{q-}\}$ as a function of the final momentum k_f , a cutoff energy $k_f^2/2$ can be determined by finding the k_f that satisfies the condition

$$\text{Re}[S_{k_f}^{m,n}(k_i^{q+}, t_1^{q+}, t_2^{q+})] = \text{Re}[S_{k_f}^{m,n}(k_i^{q-}, t_1^{q-}, t_2^{q-})]. \quad (36)$$

Here we reserve the index $\{q-\}$ for the unphysical solution after the cutoff. There might be multiple pairs of solutions that give different cutoff energies; however, the observed or numerically obtained ATI cutoff is typically determined by only one pair of solutions. In this work we apply the SFA and the SPM to investigate the channel-resolved ATI cutoffs, and we neglect the form factor $W_{k_f}^{m,n}(k_i^s, t_1^s)$ in Eq. (34), which does not affect the cutoffs. Denoting by $\{k_i^{c+}, t_1^{c+}, t_2^{c+}\}$ and $\{k_i^{c-}, t_1^{c-}, t_2^{c-}\}$ the dominant pair of solutions that determines the cutoff, we evaluate the ATI spectrum within the SPM as

$$|T_{\text{res}}^{m,n}(k_f)|^2 \sim \left| \sum_{s=\{c+,c-\}} \frac{\exp[i S_{k_f}^{m,n}(k_i^s, t_1^s, t_2^s)]}{[\Delta_{k_f}^{m,n}(k_i^s, t_1^s, t_2^s)]^{1/2}} \right|^2, \quad (37)$$

and simply drop the unphysical solution $\{k_i^{c-}, t_1^{c-}, t_2^{c-}\}$ for energies beyond the cutoff. Although the absolute spectral intensity is lost in Eq. (37), the SPM analysis enables us to find well-defined cutoffs in different ionic channels, and to identify the corresponding rescattering processes.

III. RESULTS AND DISCUSSION

A. Two-electron TDSE versus SAEA

We first investigate the validity of the SAEA for a fixed laser intensity of 8×10^{13} W/cm², but at different wavelengths. Figure 1 shows the ATI spectra in the lowest three ionic

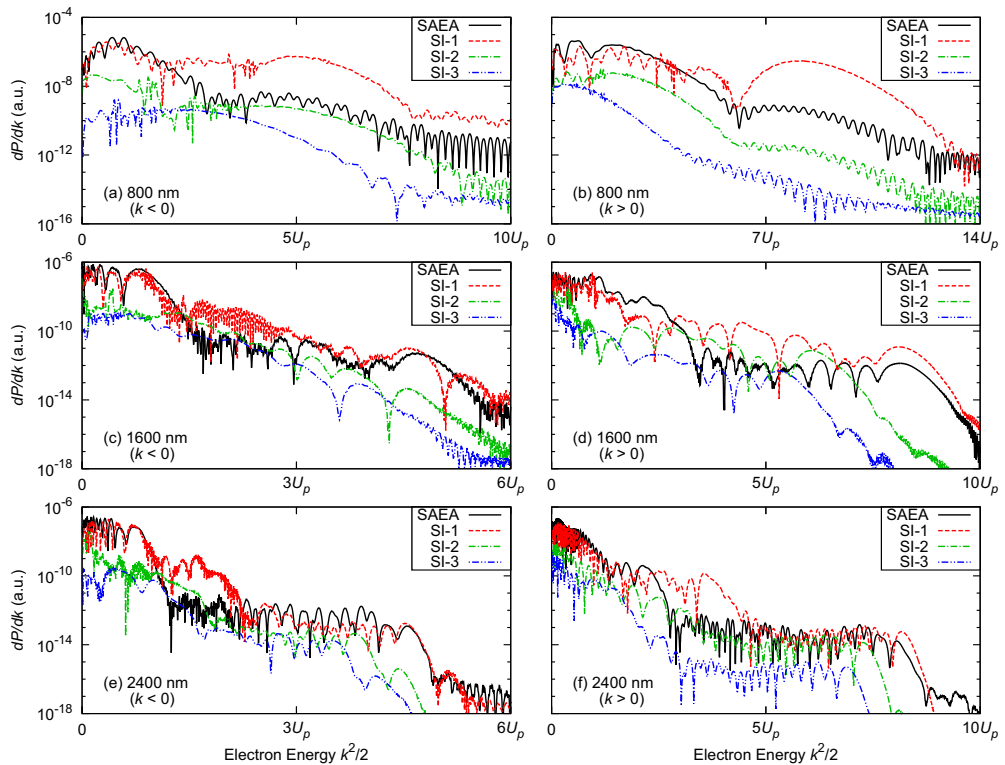


FIG. 1. ATI spectra computed within the SAEA, compared with the SI spectra in the lowest three ionic channels (SI-1, SI-2, and SI-3) extracted from the two-electron TDSE, for two-cycle laser pulses with wavelengths of 800, 1600, and 2400 nm. The peak intensity is fixed at $8 \times 10^{13} \text{ W/cm}^2$.

channels obtained from the two-electron TDSE [Eq. (1)] compared with the ATI spectra obtained from the SAEA TDSE [Eq. (6)], for wavelengths of 800, 1600, and 2400 nm. For the considered two-cycle pulses, there exists obvious asymmetry in the two opposite directions ($k < 0$ and $k > 0$) and the prediction of the typical $10U_p$ cutoff (for long pulses with more than 10 cycles) is not valid.

Figure 1 shows that, in general, the SI in the ground-state ionic channel (SI-1) is dominant while the ATI spectra in the excited-state ionic channels are much weaker. The total SI spectra (not shown) are well represented by the SI-1 spectra. Therefore we focus on the comparison between the SI-1 and SAEA spectra, to study the validity of the SAEA. For the wavelength of 800 nm, it is difficult to clearly identify the ATI plateau and cutoff features. Also in Figs. 1(a) and 1(b) there exists a large disagreement between the SI-1 and SAEA spectra, especially in the high-energy region, where the SI-1 and SAEA spectral intensities differ by around two orders of magnitude. Such disagreement becomes smaller and the plateau and cutoff features become more pronounced, as the wavelength increases to 1600 nm and 2400 nm. For a

wavelength of 2400 nm, the high-energy part of the SAEA spectra is quite similar to that of the SI-1 spectra (and also the total SI spectra). In terms of the high-order ATI spectra corresponding to the back-rescattered electrons, we conclude that the SAEA works better at longer wavelengths for a fixed laser intensity.

A useful quantity for classifying strong-field ionization is the Keldysh parameter $\gamma = \sqrt{I_p/2U_p}$ [10]. For a fixed laser intensity, the ponderomotive energy U_p becomes larger as the wavelength increases, resulting in a smaller Keldysh parameter γ , which means that the ionization dynamics become more tunneling-like. Thus the conclusion drawn from Fig. 1 implies that the SAEA works better for dynamics in the tunneling ionization regime. Now we investigate the validity of the SAEA from a different perspective. We vary the intensity with the wavelength, keeping U_p (and γ) fixed. The ponderomotive energy is fixed at $U_p = 1.58$, which is determined by the laser parameters used in Figs. 1(e) and 1(f). The Keldysh parameter for the 1D model of He is $\gamma = 0.49 < 1$, which is in the tunneling ionization regime. For wavelengths of 800 and 1600 nm, the corresponding intensities are 7.2×10^{14} and

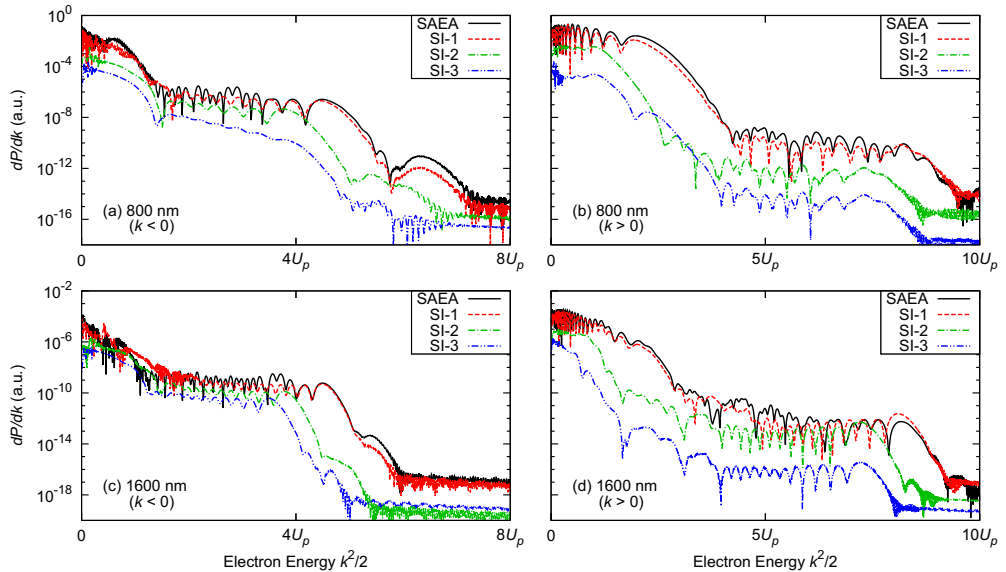


FIG. 2. ATI spectra computed within the SAEA, compared with the SI spectra in the lowest three ionic channels (SI-1, SI-2, and SI-3) extracted from the two-electron TDSE, for two-cycle laser pulses with wavelengths of 800 and 1600 nm. The corresponding peak intensities are 7.2×10^{14} W/cm² (for 800 nm) and 1.8×10^{14} W/cm² (for 1600 nm), keeping $U_p = 1.58$, as in Figs. 1(e) and 1(f).

1.8×10^{14} W/cm², respectively, and the results are presented in Fig. 2. Similarly to Figs. 1(e) and 1(f), Fig. 2 shows good agreement between the SAEA and SI-1 spectra, especially for energies near the cutoff. This means that the SAEA could also be applied to the near-infrared regime (e.g., 800 nm), as long as the ponderomotive energy is large.

The large U_p leads to high-energy rescattering electrons, which can be used for high-resolution imaging of ultrafast dynamics with the LIED technique. Our work indicates that the large U_p also makes the SAEA applicable for the theoretical analysis of the LIED. To achieve large U_p , it is more practical to increase the wavelength than the intensity. The LIED technique based on mid-infrared laser sources has a great advantage that the problematic ionization saturation can be easily avoided for such long wavelengths.

From Figs. 1 and 2, we also find that the SI in different ionic channels have different cutoffs. For example, one can observe in Figs. 1(e) and 1(f) that the cutoff energies for both ($k < 0$) and ($k > 0$) decrease in sequence from SI-1 to SI-3. Although the spectral intensities of the SI in the excited-state ionic channels are generally much lower than that of the SI-1, their cutoffs are indeed signatures of two-electron dynamics, which cannot be described within the SAEA. To study two-electron dynamics in the SI of the helium model, we turn to the application of the two-electron SFA described in Sec. II.

B. Two-electron TDSE versus two-electron SFA

As discussed in Sec. II, we consider rescattering processes to analyze the channel-resolved ATI cutoffs via the transition

probabilities of Eq. (37). For any final state in a specific ionic channel (n), there are many possible intermediate states in different ionic channels (m). To isolate the dominant rescattering process, we use the fact that the first step, i.e., the SI in the m th channel, is exponentially sensitive to the ionization potential ($E_m - E_R$). Among all the rescattering processes, the first-step SI that goes into the ground-state ionic channel ($m = 1$) is the most probable. Therefore we restrict ourselves to $T_{\text{res}}^{1,m}$ terms in the SFA and find the corresponding cutoffs based on the SPM analysis. In the SPM analysis, we only consider the dominant saddle-point solutions in the high-energy region, which correspond to backward rescattering processes. In the following discussion, we only consider the laser parameters used in Figs. 1(e) and 1(f), i.e., $\lambda = 2400$ nm and $I = 8 \times 10^{13}$ W/cm².

In the SPM analysis, the channel-resolved cutoffs are determined by one pair of saddle-point solutions to Eqs. (31)–(33) regarding the elastic and inelastic rescattering processes. To understand the rescattering in the time domain, we first show in Figs. 3(a) and 3(b) the saddle-point solutions of the ionization time t_1 and the rescattering time t_2 used in the evaluation of the elastic rescattering term $T_{\text{res}}^{1,1}$. Note that only the dominant pair of solutions that determines the cutoff is presented here. The real parts of the solutions could be understood as the physical times where the ionization and rescattering occur. By comparing the solutions with the electric field $F(t) = -\partial_t A(t)$, whose variation is also indicated in Figs. 3(a) and 3(b), one finds that the ionization and rescattering events are confined to small regions of time.

ABOVE-THRESHOLD IONIZATION OF HELIUM IN THE ...

PHYSICAL REVIEW A 95, 063407 (2017)

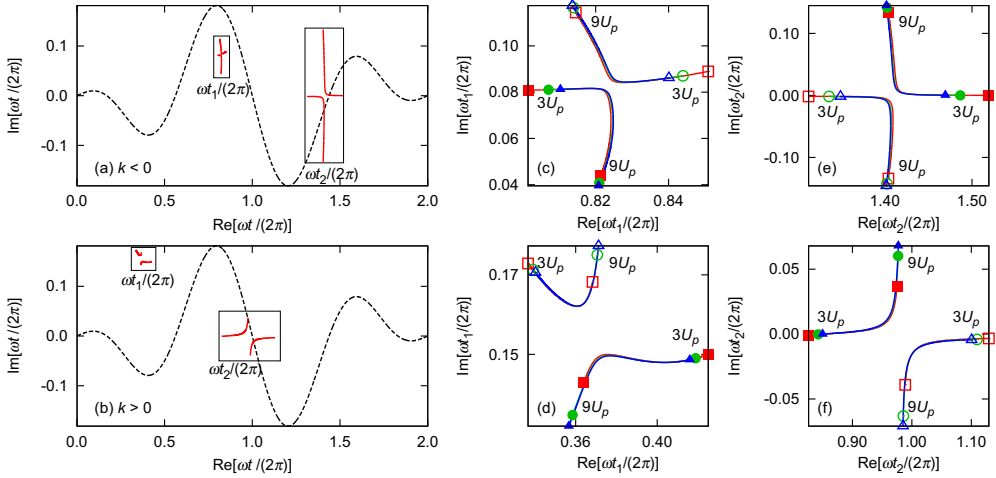


FIG. 3. (a) and (b) Saddle-point solutions of the ionization time t_1 and the rescattering time t_2 (the red solid lines) used to evaluate the elastic rescattering term $T_{\text{res}}^{1,1}$, for the final energy range from $3U_p$ to $9U_p$. The considered laser parameters are the same as in Figs. 1(e) and 1(f). The electric field $F(t) = -\partial_t A(t)$ is presented (in arbitrary units) by the black dashed line. (c)–(f) Zoom-in view of the saddle-point solutions used to evaluate $T_{\text{res}}^{1,1}$ (red lines with square markers), $T_{\text{res}}^{1,2}$ (green lines with circle markers), and $T_{\text{res}}^{1,3}$ (blue lines with triangle markers), for the same final energy range. The line markers indicate the final energies of $3U_p$ and $9U_p$, i.e., the end points of the curves. For energies beyond the cutoff, the solutions labeled by empty markers become unphysical and are dropped in the evaluation of Eq. (37).

To identify the common features of the elastic and inelastic processes and the difference between them, we take a detailed view of the saddle-point solutions for $T_{\text{res}}^{1,1}$, $T_{\text{res}}^{1,2}$, and $T_{\text{res}}^{1,3}$ in Figs. 3(c)–3(f), i.e., for the elastic rescattering in the ground-state ionic channel $T_{\text{res}}^{1,1}$ along with the inelastic rescattering in the excited-state ionic channels $T_{\text{res}}^{1,2}$ and $T_{\text{res}}^{1,3}$. It is observed that the curves of the solutions for different rescattering processes almost coincide. For a specific final energy, however, the solutions for different rescattering processes are different; e.g., the line markers of different types are at different positions. Both the elastic and inelastic rescattering processes considered here have the common feature that the ionization occurs around a peak of the electric field while the rescattering occurs when the electric field is close to zero. It is worth mentioning that the actual ionization dynamics may happen at any time during the laser interaction, which makes the final outcome (e.g., the ATI spectra) complicated to decode. By applying the SPM, however, one can find the dominant processes for explaining parts of the results. Therefore the SPM not only simplifies the evaluation of the integrals in the SFA, but also provides physical insight into the dynamics.

In Fig. 4 we present the SPM analysis of the ATI cutoffs in the lowest three ionic channels. The cutoffs obtained from the SPM analysis are indicated by the dotted vertical lines, and the energies are given in the caption. For the ground-state ionic channel ($n = 1$), the elastic rescattering term $T_{\text{res}}^{1,1}$ gives exact cutoff positions for both the ($k < 0$) and ($k > 0$) cases. The elastic rescattering terms $T_{\text{res}}^{1,2}$ and $T_{\text{res}}^{1,3}$ give exact cutoff positions for the excited-state ionic channels ($n = 2$) and

($n = 3$), respectively. In terms of the channel-resolved ATI cutoffs, the good agreement between the SPM and the TDSE results implies that the SFA could be a useful qualitative tool for the strong-field ionization in the long-wavelength regime. In the inelastic rescattering, part of the kinetic energy of the freed electron is consumed for the excitation of the ionic state, resulting in a smaller final kinetic energy than that in the elastic rescattering. For the considered 1D model, the energies of the lowest three ionic states are $E_1 = -1.483$, $E_2 = -0.772$, and $E_3 = -0.465$. The energy difference between the ionic ground state and the first excited state is, hence, $E_2 - E_1 = 0.711$. Naively one might expect that this difference should correspond to the difference in the cutoff energies for the SI-1 and SI-2 channels. However, the differences in cutoffs between the SI-1 and SI-2 channels are 1.13 and 1.42 in Figs. 4(a) and 4(b), respectively. In both cases these cutoff differences are very different from the energy difference in the ionic states, and this discrepancy comes from the fact that the vector potential at the rescattering time enters the cutoff analysis [see Eq. (33)]. Similar analysis can be performed for the other cutoffs, and the conclusions are the same.

In closing this section, we briefly mention that although the SFA has been widely applied, it is still a theoretical method under investigation and modification. It is well known that the SFA has drawbacks such as the loss of gauge invariance and the neglect of Coulomb effects, which has stimulated many studies aiming at improving the SFA (see, e.g., recent publications [40–42]). For our purpose of qualitatively determining the channel-resolved ATI cutoffs, the presented two-electron SFA and SPM analyses are demonstrated to be sufficient. To

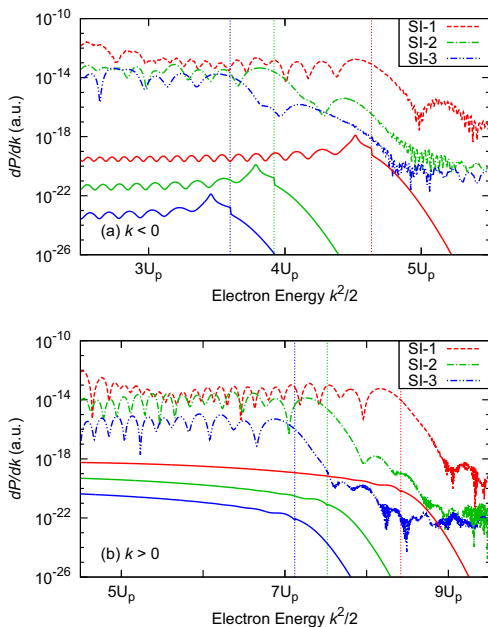


FIG. 4. Channel-resolved ATI cutoffs analyzed with the SFA and the SPM, for the same laser parameters as in Figs. 1(e) and 1(f). The solid lines, from top to bottom, are the channel-resolved high-energy ATI spectra obtained from $T_{\text{res}}^{1,1}$, $T_{\text{res}}^{1,2}$, and $T_{\text{res}}^{1,3}$, respectively. The vertical dotted lines, from right to left, indicate the corresponding cutoffs obtained from the SPM analysis, i.e., the cutoff energies of 7.33, 6.20, 5.69 in (a) and 13.31, 11.89, 11.26 in (b). For better visualization, the solid curves are vertically shifted so that they are clearly separated. The SI spectra in the lowest three ionic channels (SI-1, SI-2, and SI-3) extracted from the two-electron TDSE are also presented for comparison.

understand all the spectral features, however, one needs an improved version of the SFA for multielectron systems.

IV. COCLUSION AND OUTLOOK

We studied the channel-resolved ATI of He in the long-wavelength regime by solving the two-electron TDSE in one dimension, and examined the SAEA and the SFA including rescattering for the two-electron model. For the description of the high-energy rescattered electrons in the ground-state ionic channel, the SAEA was found to perform better with increasing U_p . This finding to some extent validates the SAEA, which is, e.g., commonly used in the theoretical analysis of LIED. The SI in the excited-state ionic channels generally shows much weaker spectral intensity than that in the ground-state ionic channel. The channel-resolved ATI cutoffs are clear signatures of two-electron dynamics, which are beyond the applicability of the SAEA. Regarding the channel-resolved ATI cutoffs at the wavelength of 2400 nm, we investigated the elastic and inelastic rescattering processes by applying the SFA and the SPM, and found good agreement of the cutoff positions between the SPM and the TDSE results. Therefore the two-electron SFA including elastic and inelastic rescattering is proven to be a useful tool for qualitative studies of the strong-field ionization in the long-wavelength regime. Since the full TDSE calculations of multielectron systems are very challenging for long-wavelength laser interactions, it is mandatory to seek good theoretical methods that require fewer computational resources. The two-electron 1D model is a practical reference for developing and examining multielectron theories in the long-wavelength regime.

ACKNOWLEDGMENTS

This work was supported by the VKR center of excellence, QUSCOPE. The numerical results were obtained at the Centre for Scientific Computing, Aarhus.

- [1] P. Agostini, F. Fabre, G. Mainfray, G. Petite, and N. K. Rahman, Free-Free Transitions Following Six-Photon Ionization of Xenon Atoms, *Phys. Rev. Lett.* **42**, 1127 (1979).
- [2] J. Eberly, J. Javanainen, and K. Rzażewski, Above-threshold ionization, *Phys. Rep.* **204**, 331 (1991).
- [3] W. Becker, F. Grasbon, R. Kopold, D. B. Milošević, G. Paulus, and H. Walther, Above-threshold ionization: From classical features to quantum effects, *Adv. At. Mol. Opt. Phys.* **48**, 35 (2002).
- [4] D. B. Milošević, G. G. Paulus, D. Bauer, and W. Becker, Above-threshold ionization by few-cycle pulses, *J. Phys. B* **39**, R203 (2006).
- [5] T. Zuo, A. Bandrauk, and P. Corkum, Laser-induced electron diffraction: A new tool for probing ultrafast molecular dynamics, *Chem. Phys. Lett.* **259**, 313 (1996).
- [6] B. Wolter, M. G. Pullen, M. Baudisch, M. Sclafani, M. Hemmer, A. Senfleben, C. D. Schröter, J. Ullrich, R. Moshhammer, and J. Biegert, Strong-Field Physics with Mid-IR Fields, *Phys. Rev. X* **5**, 021034 (2015).
- [7] C. I. Blaga, J. Xu, A. D. DiChiara, E. Sistrunk, K. Zhang, P. Agostini, T. A. Miller, L. F. DiMauro, and C. Lin, Imaging ultrafast molecular dynamics with laser-induced electron diffraction, *Nature (London)* **483**, 194 (2012).
- [8] M. G. Pullen, B. Wolter, A.-T. Le, M. Baudisch, M. Hemmer, A. Senfleben, C. D. Schröter, J. Ullrich, R. Moshhammer, C.-D. Lin *et al.*, Imaging an aligned polyatomic molecule with laser-induced electron diffraction, *Nat. Commun.* **6**, 7262 (2015).
- [9] B. Wolter, M. G. Pullen, A.-T. Le, M. Baudisch, K. Doblhoff-Dier, A. Senfleben, M. Hemmer, C. D. Schröter, J. Ullrich, T. Pfeifer, R. Moshhammer, S. Gräfe, O. Vendrell, C. D. Lin, and J. Biegert, Ultrafast electron diffraction imaging of bond breaking in di-ionized acetylene, *Science* **354**, 308 (2016).

ABOVE-THRESHOLD IONIZATION OF HELIUM IN THE ...

PHYSICAL REVIEW A 95, 063407 (2017)

- [10] L. V. Keldysh, Ionization in the field of a strong electromagnetic wave, *Zh. Eksp. Teor. Fiz.* **47**, 1945 (1964) [*Sov. Phys. JETP* **20**, 1307 (1965)].
- [11] F. H. M. Faisal, Multiple absorption of laser photons by atoms, *J. Phys. B* **6**, L89 (1973).
- [12] H. R. Reiss, Effect of an intense electromagnetic field on a weakly bound system, *Phys. Rev. A* **22**, 1786 (1980).
- [13] R. Kopold, W. Becker, and M. Kleber, Quantum path analysis of high-order above-threshold ionization, *Opt. Commun.* **179**, 39 (2000).
- [14] R. Kopold, W. Becker, H. Rottke, and W. Sandner, Routes to Nonsequential Double Ionization, *Phys. Rev. Lett.* **85**, 3781 (2000).
- [15] C. Figueira de Morisson Faria, H. Schomerus, and W. Becker, High-order above-threshold ionization: The uniform approximation and the effect of the binding potential, *Phys. Rev. A* **66**, 043413 (2002).
- [16] D. B. Milošević and W. Becker, Role of long quantum orbits in high-order harmonic generation, *Phys. Rev. A* **66**, 063417 (2002).
- [17] C. Figueira de Morisson Faria, H. Schomerus, X. Liu, and W. Becker, Electron-electron dynamics in laser-induced nonsequential double ionization, *Phys. Rev. A* **69**, 043405 (2004).
- [18] D. B. Milošević, G. G. Paulus, and W. Becker, Ionization by few-cycle pulses: Tracing the electron orbits, *Phys. Rev. A* **71**, 061404 (2005).
- [19] D. B. Milošević, E. Hasović, M. Busuladžić, A. Gazibegović-Busuladžić, and W. Becker, Intensity-dependent enhancements in high-order above-threshold ionization, *Phys. Rev. A* **76**, 053410 (2007).
- [20] D. Dimitrovski, C. P. J. Martiny, and L. B. Madsen, Strong-field ionization of polar molecules: Stark-shift-corrected strong-field approximation, *Phys. Rev. A* **82**, 053404 (2010).
- [21] T.-M. Yan, S. V. Popruzhenko, M. J. J. Vrakking, and D. Bauer, Low-Energy Structures in Strong Field Ionization Revealed by Quantum Orbits, *Phys. Rev. Lett.* **105**, 253002 (2010).
- [22] T. Shaaran, M. T. Nygren, and C. Figueira de Morisson Faria, Laser-induced nonsequential double ionization at and above the recollision-excitation-tunneling threshold, *Phys. Rev. A* **81**, 063413 (2010).
- [23] T. Shaaran, C. Figueira de Morisson Faria, and H. Schomerus, Causality and quantum interference in time-delayed laser-induced nonsequential double ionization, *Phys. Rev. A* **85**, 023423 (2012).
- [24] A. S. Maxwell and C. Figueira de Morisson Faria, Quantum interference in time-delayed nonsequential double ionization, *Phys. Rev. A* **92**, 023421 (2015).
- [25] A. S. Maxwell and C. Figueira de Morisson Faria, Controlling Below-Threshold Nonsequential Double Ionization via Quantum Interference, *Phys. Rev. Lett.* **116**, 143001 (2016).
- [26] R. Grobe and J. H. Eberly, Photoelectron Spectra for a Two-Electron System in a Strong Laser Field, *Phys. Rev. Lett.* **68**, 2905 (1992).
- [27] M. Lein, E. K. U. Gross, and V. Engel, Intense-Field Double Ionization of Helium: Identifying the Mechanism, *Phys. Rev. Lett.* **85**, 4707 (2000).
- [28] M. Ruggenthaler and D. Bauer, Rabi Oscillations and Few-Level Approximations in Time-Dependent Density Functional Theory, *Phys. Rev. Lett.* **102**, 233001 (2009).
- [29] T. N. Rescigno and C. W. McCurdy, Numerical grid methods for quantum-mechanical scattering problems, *Phys. Rev. A* **62**, 032706 (2000).
- [30] A. Scrinzi, Infinite-range exterior complex scaling as a perfect absorber in time-dependent problems, *Phys. Rev. A* **81**, 053845 (2010).
- [31] M. Weinmüller, M. Weinmüller, J. Rohland, and A. Scrinzi, Perfect absorption in Schrödinger-like problems using non-equidistant complex grids, *J. Comput. Phys.* **333**, 199 (2017).
- [32] T. J. Park and J. C. Light, Unitary quantum time evolution by iterative Lanczos reduction, *J. Chem. Phys.* **85**, 5870 (1986).
- [33] X. Guan, O. Zatsarinny, K. Bartschat, B. I. Schneider, J. Feist, and C. J. Noble, General approach to few-cycle intense laser interactions with complex atoms, *Phys. Rev. A* **76**, 053411 (2007).
- [34] R. Kosloff and H. Tal-Ezer, A direct relaxation method for calculating eigenfunctions and eigenvalues of the Schrödinger equation on a grid, *Chem. Phys. Lett.* **127**, 223 (1986).
- [35] L. Tao and A. Scrinzi, Photo-electron momentum spectra from minimal volumes: The time-dependent surface flux method, *New J. Phys.* **14**, 013021 (2012).
- [36] A. Scrinzi, *r*-SURFF: Fully differential two-electron photoemission spectra, *New J. Phys.* **14**, 085008 (2012).
- [37] A. Zielinski, V. P. Majety, and A. Scrinzi, Double photoelectron momentum spectra of helium at infrared wavelength, *Phys. Rev. A* **93**, 023406 (2016).
- [38] L. A. A. Nikolopoulos, T. K. Kjeldsen, and L. B. Madsen, Three-dimensional time-dependent Hartree-Fock approach for arbitrarily oriented molecular hydrogen in strong electromagnetic fields, *Phys. Rev. A* **76**, 033402 (2007).
- [39] A. Becker and F. H. M. Faisal, Intense-field many-body *S*-matrix theory, *J. Phys. B* **38**, R1 (2005).
- [40] A. Galstyan, O. Chuluunbaatar, A. Hamido, Y. V. Popov, F. Mota-Furtado, P. F. O'Mahony, N. Janssens, F. Catoire, and B. Piraux, Reformulation of the strong-field approximation for light-matter interactions, *Phys. Rev. A* **93**, 023422 (2016).
- [41] F. H. M. Faisal, Strong-field *S*-matrix theory with final-state Coulomb interaction in all orders, *Phys. Rev. A* **94**, 031401 (2016).
- [42] M. Kläiber, J. Daněk, E. Yakaboylu, K. Z. Hatsagortsyan, and C. H. Keitel, Strong-field ionization via a high-order Coulomb-corrected strong-field approximation, *Phys. Rev. A* **95**, 023403 (2017).

Copyright Licenses

The copyright license agreements for reusing our publications [91–93] in this thesis are attached.

**AMERICAN PHYSICAL SOCIETY LICENSE
TERMS AND CONDITIONS**

Sep 27, 2017

This Agreement between Chuan Yu ("You") and American Physical Society ("American Physical Society") consists of your license details and the terms and conditions provided by American Physical Society and Copyright Clearance Center.

License Number	4193720887522
License date	Sep 21, 2017
Licensed Content Publisher	American Physical Society
Licensed Content Publication	Physical Review A
Licensed Content Title	Ionization of helium by intense XUV laser pulses: Numerical simulations on channel-resolved probabilities
Licensed Content Author	Chuan Yu and Lars Bojer Madsen
Licensed Content Date	Apr 14, 2016
Licensed Content Volume	93
Type of Use	Thesis/Dissertation
Requestor type	Student
Format	Print, Electronic
Portion	chapter/article
Rights for	Main product
Duration of use	Life of Current Edition
Creation of copies for the disabled	no
With minor editing privileges	no
For distribution to	Worldwide
In the following language(s)	Original language of publication
With incidental promotional use	no
The lifetime unit quantity of new product	0 to 499
The requesting person/organization is:	Chuan Yu
Order reference number	
Title of your thesis / dissertation	Strong-field Ionization of Two-electron Model Atoms
Expected completion date	Sep 2017
Expected size (number of pages)	140
Requestor Location	Chuan Yu Department of Physics and Astronomy Aarhus University Aarhus C, 8000 Denmark Attn: Chuan Yu
Billing Type	Invoice

Billing Address

Chuan Yu
Department of Physics and Astronomy
Aarhus University

Aarhus C, Denmark 8000
Attn: Chuan Yu

Total

0.00 USD

Terms and Conditions**Terms and Conditions**

The American Physical Society (APS) is pleased to grant the Requestor of this license a non-exclusive, non-transferable permission, limited to **print** and/or **electronic** format, depending on what they chose], provided all criteria outlined below are followed.

1. You must also obtain permission from at least one of the lead authors for each separate work, if you haven't done so already. The author's name and affiliation can be found on the first page of the published Article.
2. For electronic format permissions, Requestor agrees to provide a hyperlink from the reprinted APS material using the source material's DOI on the web page where the work appears. The hyperlink should use the standard DOI resolution URL, <http://dx.doi.org/{DOI}>. The hyperlink may be embedded in the copyright credit line.
3. For print format permissions, Requestor agrees to print the required copyright credit line on the first page where the material appears: "Reprinted (abstract/excerpt /figure) with permission from [(FULL REFERENCE CITATION) as follows: Author's Names, APS Journal Title, Volume Number, Page Number and Year of Publication.] Copyright (YEAR) by the American Physical Society."
4. Permission granted in this license is for a one-time use and does not include permission for any future editions, updates, databases, formats or other matters. Permission must be sought for any additional use.
5. Use of the material does not and must not imply any endorsement by APS.
6. Under no circumstance does APS purport or intend to grant permission to reuse materials to which it does not hold copyright. It is the requestors sole responsibility to ensure the licensed material is original to APS and does not contain the copyright of another entity, and that the copyright notice of the figure, photograph, cover or table does not indicate that it was reprinted by APS, with permission from another source.
7. The permission granted herein is personal to the Requestor for the use specified and is not transferable or assignable without express written permission of APS. This license may not be amended except in writing by APS.
8. You may not alter, edit or modify the material in any manner.
9. You may translate the materials only when translation rights have been granted.
10. You may not use the material for promotional, sales, advertising or marketing purposes.

11. The foregoing license shall not take effect unless and until APS or its agent, Copyright Clearance Center (CCC), receives payment in full in accordance with CCC Billing and Payment Terms and Conditions, which are incorporated herein by reference.

12. Should the terms of this license be violated at any time, APS or CCC may revoke the license with no refund to you and seek relief to the fullest extent of the laws of the USA. Official written notice will be made using the contact information provided with the permission request. Failure to receive such notice will not nullify revocation of the permission.

13. APS reserves all rights not specifically granted herein.

14. This document, including the CCC Billing and Payment Terms and Conditions, shall be the entire agreement between the parties relating to the subject matter hereof.

Other Terms and Conditions

Version 1.1

Questions? customercare@copyright.com or +1-855-239-3415 (toll free in the US) or +1-978-646-2777.

**AMERICAN PHYSICAL SOCIETY LICENSE
TERMS AND CONDITIONS**

Sep 27, 2017

This Agreement between Chuan Yu ("You") and American Physical Society ("American Physical Society") consists of your license details and the terms and conditions provided by American Physical Society and Copyright Clearance Center.

License Number	4193721183245
License date	Sep 21, 2017
Licensed Content Publisher	American Physical Society
Licensed Content Publication	Physical Review A
Licensed Content Title	Sequential and nonsequential double ionization of helium by intense XUV laser pulses: Revealing ac Stark shifts from joint energy spectra
Licensed Content Author	Chuan Yu and Lars Bojer Madsen
Licensed Content Date	Nov 29, 2016
Licensed Content Volume	94
Type of Use	Thesis/Dissertation
Requestor type	Student
Format	Print, Electronic
Portion	chapter/article
Rights for	Main product
Duration of use	Life of Current Edition
Creation of copies for the disabled	no
With minor editing privileges	no
For distribution to	Worldwide
In the following language(s)	Original language of publication
With incidental promotional use	no
The lifetime unit quantity of new product	0 to 499
The requesting person/organization is:	Chuan Yu
Order reference number	
Title of your thesis / dissertation	Strong-field Ionization of Two-electron Model Atoms
Expected completion date	Sep 2017
Expected size (number of pages)	140
Requestor Location	Chuan Yu Department of Physics and Astronomy Aarhus University Aarhus C, 8000 Denmark Attn: Chuan Yu
Billing Type	Invoice

Billing Address

Chuan Yu
Department of Physics and Astronomy
Aarhus University

Aarhus C, Denmark 8000
Attn: Chuan Yu

Total

0.00 USD

[Terms and Conditions](#)**Terms and Conditions**

The American Physical Society (APS) is pleased to grant the Requestor of this license a non-exclusive, non-transferable permission, limited to **print** and/or **electronic** format, depending on what they chose], provided all criteria outlined below are followed.

1. You must also obtain permission from at least one of the lead authors for each separate work, if you haven't done so already. The author's name and affiliation can be found on the first page of the published Article.
2. For electronic format permissions, Requestor agrees to provide a hyperlink from the reprinted APS material using the source material's DOI on the web page where the work appears. The hyperlink should use the standard DOI resolution URL, <http://dx.doi.org/{DOI}>. The hyperlink may be embedded in the copyright credit line.
3. For print format permissions, Requestor agrees to print the required copyright credit line on the first page where the material appears: "Reprinted (abstract/excerpt /figure) with permission from [(FULL REFERENCE CITATION) as follows: Author's Names, APS Journal Title, Volume Number, Page Number and Year of Publication.] Copyright (YEAR) by the American Physical Society."
4. Permission granted in this license is for a one-time use and does not include permission for any future editions, updates, databases, formats or other matters. Permission must be sought for any additional use.
5. Use of the material does not and must not imply any endorsement by APS.
6. Under no circumstance does APS purport or intend to grant permission to reuse materials to which it does not hold copyright. It is the requestors sole responsibility to ensure the licensed material is original to APS and does not contain the copyright of another entity, and that the copyright notice of the figure, photograph, cover or table does not indicate that it was reprinted by APS, with permission from another source.
7. The permission granted herein is personal to the Requestor for the use specified and is not transferable or assignable without express written permission of APS. This license may not be amended except in writing by APS.
8. You may not alter, edit or modify the material in any manner.
9. You may translate the materials only when translation rights have been granted.
10. You may not use the material for promotional, sales, advertising or marketing purposes.

11. The foregoing license shall not take effect unless and until APS or its agent, Copyright Clearance Center (CCC), receives payment in full in accordance with CCC Billing and Payment Terms and Conditions, which are incorporated herein by reference.

12. Should the terms of this license be violated at any time, APS or CCC may revoke the license with no refund to you and seek relief to the fullest extent of the laws of the USA. Official written notice will be made using the contact information provided with the permission request. Failure to receive such notice will not nullify revocation of the permission.

13. APS reserves all rights not specifically granted herein.

14. This document, including the CCC Billing and Payment Terms and Conditions, shall be the entire agreement between the parties relating to the subject matter hereof.

Other Terms and Conditions

Version 1.1

Questions? customercare@copyright.com or +1-855-239-3415 (toll free in the US) or +1-978-646-2777.

**AMERICAN PHYSICAL SOCIETY LICENSE
TERMS AND CONDITIONS**

Sep 27, 2017

This Agreement between Chuan Yu ("You") and American Physical Society ("American Physical Society") consists of your license details and the terms and conditions provided by American Physical Society and Copyright Clearance Center.

License Number	4193721358218
License date	Sep 21, 2017
Licensed Content Publisher	American Physical Society
Licensed Content Publication	Physical Review A
Licensed Content Title	Above-threshold ionization of helium in the long-wavelength regime: Examining the single-active-electron approximation and the two-electron strong-field approximation
Licensed Content Author	Chuan Yu and Lars Bojer Madsen
Licensed Content Date	Jun 8, 2017
Licensed Content Volume	95
Type of Use	Thesis/Dissertation
Requestor type	Student
Format	Print, Electronic
Portion	chapter/article
Rights for	Main product
Duration of use	Life of Current Edition
Creation of copies for the disabled	no
With minor editing privileges	no
For distribution to	Worldwide
In the following language(s)	Original language of publication
With incidental promotional use	no
The lifetime unit quantity of new product	0 to 499
The requesting person/organization is:	Chuan Yu
Order reference number	
Title of your thesis / dissertation	Strong-field Ionization of Two-electron Model Atoms
Expected completion date	Sep 2017
Expected size (number of pages)	140
Requestor Location	Chuan Yu Department of Physics and Astronomy Aarhus University Aarhus C, 8000 Denmark Attn: Chuan Yu
Billing Type	Invoice

Billing Address

Chuan Yu
Department of Physics and Astronomy
Aarhus University

Aarhus C, Denmark 8000
Attn: Chuan Yu

Total

0.00 USD

Terms and Conditions**Terms and Conditions**

The American Physical Society (APS) is pleased to grant the Requestor of this license a non-exclusive, non-transferable permission, limited to **print** and/or **electronic** format, depending on what they chose], provided all criteria outlined below are followed.

1. You must also obtain permission from at least one of the lead authors for each separate work, if you haven't done so already. The author's name and affiliation can be found on the first page of the published Article.
2. For electronic format permissions, Requestor agrees to provide a hyperlink from the reprinted APS material using the source material's DOI on the web page where the work appears. The hyperlink should use the standard DOI resolution URL, <http://dx.doi.org/{DOI}>. The hyperlink may be embedded in the copyright credit line.
3. For print format permissions, Requestor agrees to print the required copyright credit line on the first page where the material appears: "Reprinted (abstract/excerpt /figure) with permission from [(FULL REFERENCE CITATION) as follows: Author's Names, APS Journal Title, Volume Number, Page Number and Year of Publication.] Copyright (YEAR) by the American Physical Society."
4. Permission granted in this license is for a one-time use and does not include permission for any future editions, updates, databases, formats or other matters. Permission must be sought for any additional use.
5. Use of the material does not and must not imply any endorsement by APS.
6. Under no circumstance does APS purport or intend to grant permission to reuse materials to which it does not hold copyright. It is the requestors sole responsibility to ensure the licensed material is original to APS and does not contain the copyright of another entity, and that the copyright notice of the figure, photograph, cover or table does not indicate that it was reprinted by APS, with permission from another source.
7. The permission granted herein is personal to the Requestor for the use specified and is not transferable or assignable without express written permission of APS. This license may not be amended except in writing by APS.
8. You may not alter, edit or modify the material in any manner.
9. You may translate the materials only when translation rights have been granted.
10. You may not use the material for promotional, sales, advertising or marketing purposes.

11. The foregoing license shall not take effect unless and until APS or its agent, Copyright Clearance Center (CCC), receives payment in full in accordance with CCC Billing and Payment Terms and Conditions, which are incorporated herein by reference.

12. Should the terms of this license be violated at any time, APS or CCC may revoke the license with no refund to you and seek relief to the fullest extent of the laws of the USA. Official written notice will be made using the contact information provided with the permission request. Failure to receive such notice will not nullify revocation of the permission.

13. APS reserves all rights not specifically granted herein.

14. This document, including the CCC Billing and Payment Terms and Conditions, shall be the entire agreement between the parties relating to the subject matter hereof.

Other Terms and Conditions

Version 1.1

Questions? customercare@copyright.com or +1-855-239-3415 (toll free in the US) or +1-978-646-2777.

Bibliography

- [1] T. H. Maiman, “*Stimulated Optical Radiation in Ruby*,” *Nature* **187**, 493 (1960).
- [2] F. Krausz and M. Ivanov, “*Attosecond physics*,” *Rev. Mod. Phys.* **81**, 163 (2009).
- [3] G. Voronov and N. Delone, “*Many-photon ionization of the xenon atom by ruby laser radiation*,” *Sov. Phys. JETP* **23**, 54 (1966).
- [4] P. Agostini, G. Barjot, J. Bonnal, G. Mainfray, C. Manus, and J. Morelle, “*Multiphoton ionization of hydrogen and rare gases*,” *IEEE J. Quantum Electron.* **4**, 667 (1968).
- [5] P. Lambropoulos, “*Multiphoton Ionization of One-Electron Atoms with Circularly Polarized Light*,” *Phys. Rev. Lett.* **29**, 453 (1972).
- [6] S. Augst, D. D. Meyerhofer, D. Strickland, and S. L. Chin, “*Laser ionization of noble gases by Coulomb-barrier suppression*,” *J. Opt. Soc. Am. B* **8**, 858 (1991).
- [7] V. Krainov and B. Shokri, “*Energy and angular distributions of electrons resulting from barrier-suppression ionization of atoms by strong low-frequency radiation*,” *Sov. Phys. JETP* **80**, 657 (1995).
- [8] V. P. Krainov, “*Ionization rates and energy and angular distributions at the barrier-suppression ionization of complex atoms and atomic ions*,” *J. Opt. Soc. Am. B* **14**, 425 (1997).
- [9] D. Bauer and P. Mulser, “*Exact field ionization rates in the barrier-suppression regime from numerical time-dependent Schrödinger-equation calculations*,” *Phys. Rev. A* **59**, 569 (1999).
- [10] X. M. Tong and C. D. Lin, “*Empirical formula for static field ionization rates of atoms and molecules by lasers in the barrier-suppression regime*,” *J. Phys. B* **38**, 2593 (2005).

-
- [11] L. D. Landau and E. M. Lifshitz, *Quantum Mechanics: Non-relativistic Theory*, 3rd ed. (Pergamon, 1977).
- [12] A. Perelomov, V. Popov, and M. Terent'ev, "Ionization of atoms in an alternating electric field," *Sov. Phys. JETP* **23**, 924 (1966).
- [13] L. V. Keldysh, "Ionization in the field of a strong electromagnetic wave," *Sov. Phys. JETP* **20**, 1307 (1965).
- [14] F. H. M. Faisal, "Multiple absorption of laser photons by atoms," *J. Phys. B* **6**, L89 (1973).
- [15] H. R. Reiss, "Effect of an intense electromagnetic field on a weakly bound system," *Phys. Rev. A* **22**, 1786 (1980).
- [16] M. Lewenstein, P. Balcou, M. Y. Ivanov, A. L'Huillier, and P. B. Corkum, "Theory of high-harmonic generation by low-frequency laser fields," *Phys. Rev. A* **49**, 2117 (1994).
- [17] A.-T. Le, H. Wei, C. Jin, and C. D. Lin, "Strong-field approximation and its extension for high-order harmonic generation with mid-infrared lasers," *J. Phys. B* **49**, 053001 (2016).
- [18] S. V. Popruzhenko, "Keldysh theory of strong field ionization: history, applications, difficulties and perspectives," *J. Phys. B* **47**, 204001 (2014).
- [19] S. V. Popruzhenko, G. G. Paulus, and D. Bauer, "Coulomb-corrected quantum trajectories in strong-field ionization," *Phys. Rev. A* **77**, 053409 (2008).
- [20] S. V. Popruzhenko and D. Bauer, "Strong field approximation for systems with Coulomb interaction," *J. Mod. Opt.* **55**, 2573 (2008).
- [21] D. B. Milošević, "Phase space path-integral formulation of the above-threshold ionization," *J. Math. Phys.* **54**, 042101 (2013).
- [22] M. Klaiber, E. Yakaboylu, and K. Z. Hatsagortsyan, "Above-threshold ionization with highly charged ions in superstrong laser fields. I. Coulomb-corrected strong-field approximation," *Phys. Rev. A* **87**, 023417 (2013).
- [23] X.-Y. Lai, C. Poli, H. Schomerus, and C. Figueira de Morisson Faria, "Influence of the Coulomb potential on above-threshold ionization: A quantum-orbit analysis beyond the strong-field approximation," *Phys. Rev. A* **92**, 043407 (2015).

-
- [24] A. Galstyan, O. Chuluunbaatar, A. Hamido, Y. V. Popov, F. Mota-Furtado, P. F. O'Mahony, N. Janssens, F. Catoire, and B. Piraux, "*Reformulation of the strong-field approximation for light-matter interactions*," Phys. Rev. A **93**, 023422 (2016).
- [25] F. H. M. Faisal, "*Strong-field S-matrix theory with final-state Coulomb interaction in all orders*," Phys. Rev. A **94**, 031401 (2016).
- [26] M. Klaiber, J. Daněk, E. Yakaboylu, K. Z. Hatsagortsyan, and C. H. Keitel, "*Strong-field ionization via a high-order Coulomb-corrected strong-field approximation*," Phys. Rev. A **95**, 023403 (2017).
- [27] A. S. Maxwell, A. Al-Jawahiry, T. Das, and C. Figueira de Morisson Faria, "*Coulomb-corrected quantum interference in above-threshold ionization: Working towards multitrajectory electron holography*," Phys. Rev. A **96**, 023420 (2017).
- [28] P. Agostini, F. Fabre, G. Mainfray, G. Petite, and N. K. Rahman, "*Free-Free Transitions Following Six-Photon Ionization of Xenon Atoms*," Phys. Rev. Lett. **42**, 1127 (1979).
- [29] J. H. Eberly, J. Javanainen, and K. Rzażewski, "*Above-threshold ionization*," Phys. Rep. **204**, 331 (1991).
- [30] W. Becker, F. Grasbon, R. Kopold, D. B. Milošević, G. Paulus, and H. Walther, "*Above-Threshold Ionization: From Classical Features to Quantum Effects*," Adv. At. Mol. Opt. Phys. **48**, 35 (2002).
- [31] D. B. Milošević, G. G. Paulus, D. Bauer, and W. Becker, "*Above-threshold ionization by few-cycle pulses*," J. Phys. B **39**, R203 (2006).
- [32] P. B. Corkum, "*Plasma perspective on strong field multiphoton ionization*," Phys. Rev. Lett. **71**, 1994 (1993).
- [33] T. Zuo, A. Bandrauk, and P. Corkum, "*Laser-induced electron diffraction: a new tool for probing ultrafast molecular dynamics*," Chem. Phys. Lett. **259**, 313 (1996).
- [34] C. Blaga, F. Catoire, P. Colosimo, G. Paulus, H. Muller, P. Agostini, and L. DiMauro, "*Strong-field photoionization revisited*," Nat. Phys. **5**, 335 (2009).
- [35] W. Quan, Z. Lin, M. Wu, H. Kang, H. Liu, X. Liu, J. Chen, J. Liu, X. T. He, S. G. Chen, H. Xiong, L. Guo, H. Xu, Y. Fu, Y. Cheng, and Z. Z. Xu,

- “Classical Aspects in Above-Threshold Ionization with a Midinfrared Strong Laser Field,”* Phys. Rev. Lett. **103**, 093001 (2009).
- [36] C. Liu and K. Z. Hatsagortsyan, *“Origin of Unexpected Low Energy Structure in Photoelectron Spectra Induced by Midinfrared Strong Laser Fields,”* Phys. Rev. Lett. **105**, 113003 (2010).
- [37] T.-M. Yan, S. V. Popruzhenko, M. J. J. Vrakking, and D. Bauer, *“Low-Energy Structures in Strong Field Ionization Revealed by Quantum Orbits,”* Phys. Rev. Lett. **105**, 253002 (2010).
- [38] D. A. Telnov and S.-I. Chu, *“Low-energy structure of above-threshold-ionization electron spectra: Role of the Coulomb threshold effect,”* Phys. Rev. A **83**, 063406 (2011).
- [39] C. Lemell, K. I. Dimitriou, X.-M. Tong, S. Nagele, D. V. Kartashov, J. Burgdörfer, and S. Gräfe, *“Low-energy peak structure in strong-field ionization by midinfrared laser pulses: Two-dimensional focusing by the atomic potential,”* Phys. Rev. A **85**, 011403 (2012).
- [40] D. B. Milošević, *“Reexamination of the improved strong-field approximation: Low-energy structures in the above-threshold-ionization spectra for short-range potentials,”* Phys. Rev. A **88**, 023417 (2013).
- [41] D. B. Milošević, *“Low-frequency approximation for above-threshold ionization by a laser pulse: Low-energy forward rescattering,”* Phys. Rev. A **90**, 063423 (2014).
- [42] E. Pisanty and M. Ivanov, *“Slalom in complex time: Emergence of low-energy structures in tunnel ionization via complex-time contours,”* Phys. Rev. A **93**, 043408 (2016).
- [43] Y. Huismans, A. Rouzée, A. Gijsbertsen, J. H. Jungmann, A. S. Smolkowska, P. S. W. M. Logman, F. Lépine, C. Cauchy, S. Zamith, T. Marchenko, J. M. Bakker, G. Berden, B. Redlich, A. F. G. van der Meer, H. G. Muller, W. Vermin, K. J. Schafer, M. Spanner, M. Y. Ivanov, O. Smirnova, D. Bauer, S. V. Popruzhenko, and M. J. J. Vrakking, *“Time-Resolved Holography with Photoelectrons,”* Science **331**, 61 (2011).
- [44] M. V. Fedorov and A. M. Movsesian, *“Field-induced effects of narrowing of photoelectron spectra and stabilisation of Rydberg atoms,”* J. Phys. B **21**, L155 (1988).

- [45] M. Pont and M. Gavrilă, “*Stabilization of atomic hydrogen in superintense, high-frequency laser fields of circular polarization,*” *Phys. Rev. Lett.* **65**, 2362 (1990).
- [46] M. P. de Boer, J. H. Hoogenraad, R. B. Vrijen, L. D. Noordam, and H. G. Muller, “*Indications of high-intensity adiabatic stabilization in neon,*” *Phys. Rev. Lett.* **71**, 3263 (1993).
- [47] R. R. Jones, D. W. Schumacher, and P. H. Bucksbaum, “*Population trapping in Kr and Xe in intense laser fields,*” *Phys. Rev. A* **47**, R49 (1993).
- [48] M. P. de Boer, J. H. Hoogenraad, R. B. Vrijen, R. C. Constantinescu, L. D. Noordam, and H. G. Muller, “*Adiabatic stabilization against photoionization: An experimental study,*” *Phys. Rev. A* **50**, 4085 (1994).
- [49] J. H. Hoogenraad, R. B. Vrijen, and L. D. Noordam, “*Ionization suppression of Rydberg atoms by short laser pulses,*” *Phys. Rev. A* **50**, 4133 (1994).
- [50] N. J. van Druten, R. C. Constantinescu, J. M. Schins, H. Nieuwenhuize, and H. G. Muller, “*Adiabatic stabilization: Observation of the surviving population,*” *Phys. Rev. A* **55**, 622 (1997).
- [51] W. C. Henneberger, “*Perturbation Method for Atoms in Intense Light Beams,*” *Phys. Rev. Lett.* **21**, 838 (1968).
- [52] M. Gavrilă and J. Z. Kamiński, “*Free-Free Transitions in Intense High-Frequency Laser Fields,*” *Phys. Rev. Lett.* **52**, 613 (1984).
- [53] N. Manakov, V. Ovsiannikov, and L. Rapoport, “*Atoms in a laser field,*” *Phys. Rep.* **141**, 320 (1986).
- [54] S.-I. Chu and D. A. Telnov, “*Beyond the Floquet theorem: generalized Floquet formalisms and quasienergy methods for atomic and molecular multiphoton processes in intense laser fields,*” *Phys. Rep.* **390**, 1 (2004).
- [55] M. Gavrilă, “*Atomic stabilization in superintense laser fields,*” *J. Phys. B* **35**, R147 (2002).
- [56] A. M. Popov, O. V. Tikhonova, and E. A. Volkova, “*Strong-field atomic stabilization: numerical simulation and analytical modelling,*” *J. Phys. B* **36**, R125 (2003).
- [57] P. Gangopadhyay, X. Tang, P. Lambropoulos, and R. Shakeshaft, “*Theory of autoionization of Xe under two- and three-photon excitation,*” *Phys. Rev. A* **34**, 2998 (1986).

-
- [58] P. Lambropoulos and X. Tang, “*Multiple excitation and ionization of atoms by strong lasers*,” J. Opt. Soc. Am. B **4**, 821 (1987).
- [59] M. G. Makris and P. Lambropoulos, “*Theoretical interpretation of multiphoton ionization of neon by soft-x-ray intense radiation*,” Phys. Rev. A **77**, 023401 (2008).
- [60] M. G. Makris, P. Lambropoulos, and A. Mihelič, “*Theory of Multiphoton Multielectron Ionization of Xenon under Strong 93-eV Radiation*,” Phys. Rev. Lett. **102**, 033002 (2009).
- [61] N. Gerken, S. Klumpp, A. A. Sorokin, K. Tiedtke, M. Richter, V. Bürk, K. Mertens, P. Juranić, and M. Martins, “*Time-Dependent Multiphoton Ionization of Xenon in the Soft-X-Ray Regime*,” Phys. Rev. Lett. **112**, 213002 (2014).
- [62] M. Ilchen, T. Mazza, E. T. Karamatskos, D. Markellos, S. Bakhtiarzadeh, A. J. Rafipour, T. J. Kelly, N. Walsh, J. T. Costello, P. O’Keeffe, N. Gerken, M. Martins, P. Lambropoulos, and M. Meyer, “*Two-electron processes in multiple ionization under strong soft-x-ray radiation*,” Phys. Rev. A **94**, 013413 (2016).
- [63] A. Becker and F. H. M. Faisal, “*Intense-field many-body S-matrix theory*,” J. Phys. B **38**, R1 (2005).
- [64] A. Becker and F. H. M. Faisal, “*Mechanism of laser-induced double ionization of helium*,” J. Phys. B **29**, L197 (1996).
- [65] A. Becker and F. H. M. Faisal, “*Interplay of electron correlation and intense field dynamics in the double ionization of helium*,” Phys. Rev. A **59**, R1742 (1999).
- [66] A. Becker and F. H. M. Faisal, “*Interpretation of Momentum Distribution of Recoil Ions from Laser Induced Nonsequential Double Ionization*,” Phys. Rev. Lett. **84**, 3546 (2000).
- [67] A. Becker and F. H. M. Faisal, “*S-Matrix Analysis of Coincident Measurement of Two-Electron Energy Distribution for Double Ionization of He in an Intense Laser Field*,” Phys. Rev. Lett. **89**, 193003 (2002).
- [68] D. N. Fittinghoff, P. R. Bolton, B. Chang, and K. C. Kulander, “*Observation of nonsequential double ionization of helium with optical tunneling*,” Phys. Rev. Lett. **69**, 2642 (1992).

- [69] K. Kondo, A. Sagisaka, T. Tamida, Y. Nabekawa, and S. Watanabe, “*Wavelength dependence of nonsequential double ionization in He*,” Phys. Rev. A **48**, R2531 (1993).
- [70] B. Walker, B. Sheehy, L. F. DiMauro, P. Agostini, K. J. Schafer, and K. C. Kulander, “*Precision Measurement of Strong Field Double Ionization of Helium*,” Phys. Rev. Lett. **73**, 1227 (1994).
- [71] W. Becker, X. Liu, P. J. Ho, and J. H. Eberly, “*Theories of photoelectron correlation in laser-driven multiple atomic ionization*,” Rev. Mod. Phys. **84**, 1011 (2012).
- [72] M. Førre, S. Selstø, and R. Nepstad, “*Nonsequential Two-Photon Double Ionization of Atoms: Identifying the Mechanism*,” Phys. Rev. Lett. **105**, 163001 (2010).
- [73] H. Bachau, “*Theory of two-photon double ionization of helium at the sequential threshold*,” Phys. Rev. A **83**, 033403 (2011).
- [74] S. Selstø, X. Raynaud, A. S. Simonsen, and M. Førre, “*Distinction between sequential and direct ionization in two-photon double ionization of helium*,” Phys. Rev. A **90**, 053412 (2014).
- [75] W.-C. Jiang, J.-Y. Shan, Q. Gong, and L.-Y. Peng, “*Virtual Sequential Picture for Nonsequential Two-Photon Double Ionization of Helium*,” Phys. Rev. Lett. **115**, 153002 (2015).
- [76] A. Liu and U. Thumm, “*Criterion for Distinguishing Sequential from Nonsequential Contributions to the Double Ionization of Helium in Ultrashort Extreme-Ultraviolet Pulses*,” Phys. Rev. Lett. **115**, 183002 (2015).
- [77] J. S. Parker, L. R. Moore, K. J. Meharg, D. Dundas, and K. T. Taylor, “*Double-electron above threshold ionization of helium*,” J. Phys. B **34**, L69 (2001).
- [78] M. Lein, E. K. U. Gross, and V. Engel, “*Discrete peaks in above-threshold double-ionization spectra*,” Phys. Rev. A **64**, 023406 (2001).
- [79] K. Henrichs, M. Waitz, F. Trinter, H. Kim, A. Menssen, H. Gassert, H. Sann, T. Jahnke, J. Wu, M. Pitzer, M. Richter, M. S. Schöffler, M. Kunitski, and R. Dörner, “*Observation of Electron Energy Discretization in Strong Field Double Ionization*,” Phys. Rev. Lett. **111**, 113003 (2013).

- [80] X. Gong, Q. Song, Q. Ji, K. Lin, H. Pan, J. Ding, H. Zeng, and J. Wu, “*Channel-Resolved Above-Threshold Double Ionization of Acetylene*,” *Phys. Rev. Lett.* **114**, 163001 (2015).
- [81] M. Spanner, J. Mikosch, A. Gijsbertsen, A. E. Boguslavskiy, and A. Stolow, “*Multielectron effects and nonadiabatic electronic dynamics in above threshold ionization and high-harmonic generation*,” *New J. Phys.* **13**, 093010 (2011).
- [82] A. E. Boguslavskiy, J. Mikosch, A. Gijsbertsen, M. Spanner, S. Patchkovskii, N. Gador, M. J. J. Vrakking, and A. Stolow, “*The Multielectron Ionization Dynamics Underlying Attosecond Strong-Field Spectroscopies*,” *Science* **335**, 1336 (2012).
- [83] R. Pazourek, S. Nagele, and J. Burgdörfer, “*Attosecond chronoscopy of photoemission*,” *Rev. Mod. Phys.* **87**, 765 (2015).
- [84] J. Itatani, F. Quéré, G. L. Yudin, M. Y. Ivanov, F. Krausz, and P. B. Corkum, “*Attosecond Streak Camera*,” *Phys. Rev. Lett.* **88**, 173903 (2002).
- [85] M. Schultze, M. Fieß, N. Karpowicz, J. Gagnon, M. Korbman, M. Hofstetter, S. Neppl, A. L. Cavalieri, Y. Komninos, T. Mercouris, C. A. Nicolaides, R. Pazourek, S. Nagele, J. Feist, J. Burgdörfer, A. M. Azzeer, R. Ernstorfer, R. Kienberger, U. Kleineberg, E. Goulielmakis, F. Krausz, and V. S. Yakovlev, “*Delay in Photoemission*,” *Science* **328**, 1658 (2010).
- [86] M. Ossiander, F. Siegrist, V. Shirvanyan, R. Pazourek, A. Sommer, T. Latka, A. Guggenmos, S. Nagele, J. Feist, J. Burgdörfer, *et al.*, “*Attosecond correlation dynamics*,” *Nat. Phys.* **13**, 280 (2017).
- [87] M. Gavrilu and J. Shertzer, “*Two-electron atoms in superintense radiation fields: Dichotomy and stabilization*,” *Phys. Rev. A* **53**, 3431 (1996).
- [88] D. Bauer and F. Ceccherini, “*Electron correlation versus stabilization: A two-electron model atom in an intense laser pulse*,” *Phys. Rev. A* **60**, 2301 (1999).
- [89] T. Birkeland, R. Nepstad, and M. Førre, “*Stabilization of Helium in Intense XUV Laser Fields*,” *Phys. Rev. Lett.* **104**, 163002 (2010).
- [90] S. A. Sørngård, S. Askeland, R. Nepstad, and M. Førre, “*Multiphoton ionization and stabilization of helium in superintense XUV fields*,” *Phys. Rev. A* **83**, 033414 (2011).

-
- [91] C. Yu and L. B. Madsen, “*Ionization of helium by intense XUV laser pulses: Numerical simulations on channel-resolved probabilities,*” *Phys. Rev. A* **93**, 043412 (2016).
- [92] C. Yu and L. B. Madsen, “*Sequential and nonsequential double ionization of helium by intense XUV laser pulses: Revealing ac Stark shifts from joint energy spectra,*” *Phys. Rev. A* **94**, 053424 (2016).
- [93] C. Yu and L. B. Madsen, “*Above-threshold ionization of helium in the long-wavelength regime: Examining the single-active-electron approximation and the two-electron strong-field approximation,*” *Phys. Rev. A* **95**, 063407 (2017).
- [94] L. B. Madsen, “*Gauge invariance in the interaction between atoms and few-cycle laser pulses,*” *Phys. Rev. A* **65**, 053417 (2002).
- [95] E. Cormier and P. Lambropoulos, “*Optimal gauge and gauge invariance in non-perturbative time-dependent calculation of above-threshold ionization,*” *J. Phys. B* **29**, 1667 (1996).
- [96] Y.-C. Han and L. B. Madsen, “*Comparison between length and velocity gauges in quantum simulations of high-order harmonic generation,*” *Phys. Rev. A* **81**, 063430 (2010).
- [97] M. Førre, J. P. Hansen, L. Kocbach, S. Selstø, and L. B. Madsen, “*Nondipole Ionization Dynamics of Atoms in Superintense High-Frequency Attosecond Pulses,*” *Phys. Rev. Lett.* **97**, 043601 (2006).
- [98] M. Førre and A. S. Simonsen, “*Nondipole ionization dynamics in atoms induced by intense xuv laser fields,*” *Phys. Rev. A* **90**, 053411 (2014).
- [99] A. Ludwig, J. Maurer, B. W. Mayer, C. R. Phillips, L. Gallmann, and U. Keller, “*Breakdown of the Dipole Approximation in Strong-Field Ionization,*” *Phys. Rev. Lett.* **113**, 243001 (2014).
- [100] S. Chelkowski, A. D. Bandrauk, and P. B. Corkum, “*Photon-momentum transfer in multiphoton ionization and in time-resolved holography with photoelectrons,*” *Phys. Rev. A* **92**, 051401 (2015).
- [101] K. C. Kulander, “*Multiphoton ionization of hydrogen: A time-dependent theory,*” *Phys. Rev. A* **35**, 445 (1987).
- [102] J. L. Krause, K. J. Schafer, and K. C. Kulander, “*Calculation of photoemission from atoms subject to intense laser fields,*” *Phys. Rev. A* **45**, 4998 (1992).

- [103] J. L. Krause, K. J. Schafer, and K. C. Kulander, “*High-order harmonic generation from atoms and ions in the high intensity regime,*” *Phys. Rev. Lett.* **68**, 3535 (1992).
- [104] M. Awasthi, Y. V. Vanne, A. Saenz, A. Castro, and P. Decleva, “*Single-active-electron approximation for describing molecules in ultrashort laser pulses and its application to molecular hydrogen,*” *Phys. Rev. A* **77**, 063403 (2008).
- [105] M. Abu-samha and L. B. Madsen, “*Single-active-electron potentials for molecules in intense laser fields,*” *Phys. Rev. A* **81**, 033416 (2010).
- [106] D. Bauer and P. Koval, “*Qprop: A Schrödinger-solver for intense laser–atom interaction,*” *Comput. Phys. Commun.* **174**, 396 (2006).
- [107] V. Mosert and D. Bauer, “*Photoelectron spectra with Qprop and t-SURFF,*” *Comput. Phys. Commun.* **207**, 452 (2016).
- [108] S. Patchkovskii and H. Muller, “*Simple, accurate, and efficient implementation of 1-electron atomic time-dependent Schrödinger equation in spherical coordinates,*” *Comput. Phys. Commun.* **199**, 153 (2016).
- [109] Y. Fu, J. Zeng, and J. Yuan, “*PCTDSE: A parallel Cartesian-grid-based TDSE solver for modeling laser–atom interactions,*” *Comput. Phys. Commun.* **210**, 181 (2017).
- [110] E. S. Smyth, J. S. Parker, and K. Taylor, “*Numerical integration of the time-dependent Schrödinger equation for laser-driven helium,*” *Comput. Phys. Commun.* **114**, 1 (1998).
- [111] S. Laulan and H. Bachau, “*Correlation effects in two-photon single and double ionization of helium,*” *Phys. Rev. A* **68**, 013409 (2003).
- [112] S. Laulan and H. Bachau, “*One- and two-photon double ionization of beryllium with ultrashort ultraviolet laser fields,*” *Phys. Rev. A* **69**, 033408 (2004).
- [113] S. X. Hu, J. Colgan, and L. A. Collins, “*Triple-differential cross-sections for two-photon double ionization of He near threshold,*” *J. Phys. B* **38**, L35 (2005).
- [114] S. X. Hu and L. A. Collins, “*Attosecond Pump Probe: Exploring Ultrafast Electron Motion inside an Atom,*” *Phys. Rev. Lett.* **96**, 073004 (2006).

- [115] J. S. Parker, B. J. S. Doherty, K. T. Taylor, K. D. Schultz, C. I. Blaga, and L. F. DiMauro, “*High-Energy Cutoff in the Spectrum of Strong-Field Nonsequential Double Ionization*,” Phys. Rev. Lett. **96**, 133001 (2006).
- [116] J. Feist, S. Nagele, R. Pazourek, E. Persson, B. I. Schneider, L. A. Collins, and J. Burgdörfer, “*Nonsequential two-photon double ionization of helium*,” Phys. Rev. A **77**, 043420 (2008).
- [117] J. Feist, S. Nagele, R. Pazourek, E. Persson, B. I. Schneider, L. A. Collins, and J. Burgdörfer, “*Probing Electron Correlation via Attosecond XUV Pulses in the Two-Photon Double Ionization of Helium*,” Phys. Rev. Lett. **103**, 063002 (2009).
- [118] R. Nepstad, T. Birkeland, and M. Førre, “*Numerical study of two-photon ionization of helium using an ab initio numerical framework*,” Phys. Rev. A **81**, 063402 (2010).
- [119] S. X. Hu, “*Optimizing the FEDVR-TDCC code for exploring the quantum dynamics of two-electron systems in intense laser pulses*,” Phys. Rev. E **81**, 056705 (2010).
- [120] Z. Zhang, L.-Y. Peng, M.-H. Xu, A. F. Starace, T. Morishita, and Q. Gong, “*Two-photon double ionization of helium: Evolution of the joint angular distribution with photon energy and two-electron energy sharing*,” Phys. Rev. A **84**, 043409 (2011).
- [121] R. Pazourek, J. Feist, S. Nagele, and J. Burgdörfer, “*Attosecond Streaking of Correlated Two-Electron Transitions in Helium*,” Phys. Rev. Lett. **108**, 163001 (2012).
- [122] S. X. Hu, “*Boosting Photoabsorption by Attosecond Control of Electron Correlation*,” Phys. Rev. Lett. **111**, 123003 (2013).
- [123] L. Argenti, R. Pazourek, J. Feist, S. Nagele, M. Liertzer, E. Persson, J. Burgdörfer, and E. Lindroth, “*Photoionization of helium by attosecond pulses: Extraction of spectra from correlated wave functions*,” Phys. Rev. A **87**, 053405 (2013).
- [124] W.-C. Jiang, L.-Y. Peng, W.-H. Xiong, and Q. Gong, “*Comparison study of electron correlation in one-photon and two-photon double ionization of helium*,” Phys. Rev. A **88**, 023410 (2013).

- [125] S. Barmaki, P. Lanteigne, and S. Laulan, “Control of two-photon double ionization of helium with intense chirped attosecond laser pulses,” *Phys. Rev. A* **89**, 063406 (2014).
- [126] A. Liu and U. Thumm, “Laser-assisted XUV few-photon double ionization of helium: Joint angular distributions,” *Phys. Rev. A* **89**, 063423 (2014).
- [127] A. Liu and U. Thumm, “Laser-assisted XUV double ionization of helium: Energy-sharing dependence of joint angular distributions,” *Phys. Rev. A* **91**, 043416 (2015).
- [128] A. Zielinski, V. P. Majety, and A. Scrinzi, “Double photoelectron momentum spectra of helium at infrared wavelength,” *Phys. Rev. A* **93**, 023406 (2016).
- [129] H. Miyagi and L. B. Madsen, “Exterior time scaling with the stiffness-free Lanczos time propagator: Formulation and application to atoms interacting with strong midinfrared lasers,” *Phys. Rev. A* **93**, 033420 (2016).
- [130] J. Javanainen and J. H. Eberly, “Model *ab initio* study of intense laser photoionisation,” *J. Phys. B* **21**, L93 (1988).
- [131] J. Javanainen, J. H. Eberly, and Q. Su, “Numerical simulations of multiphoton ionization and above-threshold electron spectra,” *Phys. Rev. A* **38**, 3430 (1988).
- [132] J. H. Eberly, Q. Su, and J. Javanainen, “Nonlinear Light Scattering Accompanying Multiphoton Ionization,” *Phys. Rev. Lett.* **62**, 881 (1989).
- [133] J. H. Eberly, Q. Su, and J. Javanainen, “High-order harmonic production in multiphoton ionization,” *J. Opt. Soc. Am. B* **6**, 1289 (1989).
- [134] Q. Su, J. H. Eberly, and J. Javanainen, “Dynamics of atomic ionization suppression and electron localization in an intense high-frequency radiation field,” *Phys. Rev. Lett.* **64**, 862 (1990).
- [135] Q. Su and J. H. Eberly, “Stabilization of a model atom in superintense field ionization,” *J. Opt. Soc. Am. B* **7**, 564 (1990).
- [136] Q. Su and J. H. Eberly, “Model atom for multiphoton physics,” *Phys. Rev. A* **44**, 5997 (1991).
- [137] R. Grobe and J. H. Eberly, “Photoelectron spectra for a two-electron system in a strong laser field,” *Phys. Rev. Lett.* **68**, 2905 (1992).

- [138] R. Grobe and J. H. Eberly, “*Single and double ionization and strong-field stabilization of a two-electron system,*” *Phys. Rev. A* **47**, R1605 (1993).
- [139] R. Grobe and J. H. Eberly, “*One-dimensional model of a negative ion and its interaction with laser fields,*” *Phys. Rev. A* **48**, 4664 (1993).
- [140] S. L. Haan, R. Grobe, and J. H. Eberly, “*Numerical study of autoionizing states in completely correlated two-electron systems,*” *Phys. Rev. A* **50**, 378 (1994).
- [141] D. Bauer, “*Two-dimensional, two-electron model atom in a laser pulse: Exact treatment, single-active-electron analysis, time-dependent density-functional theory, classical calculations, and nonsequential ionization,*” *Phys. Rev. A* **56**, 3028 (1997).
- [142] M. Lein, E. K. U. Gross, and V. Engel, “*Intense-Field Double Ionization of Helium: Identifying the Mechanism,*” *Phys. Rev. Lett.* **85**, 4707 (2000).
- [143] M. Ruggenthaler and D. Bauer, “*Rabi Oscillations and Few-Level Approximations in Time-Dependent Density Functional Theory,*” *Phys. Rev. Lett.* **102**, 233001 (2009).
- [144] Z. Zhang, L.-Y. Peng, Q. Gong, and T. Morishita, “*Momentum space analysis of multiphoton double ionization of helium by intense attosecond XUV pulses,*” *Opt. Express* **18**, 8976 (2010).
- [145] Q. Liao, Y. Zhou, C. Huang, and P. Lu, “*Multiphoton Rabi oscillations of correlated electrons in strong-field nonsequential double ionization,*” *New J. Phys.* **14**, 013001 (2012).
- [146] J. Zhao and M. Lein, “*Probing Fano resonances with ultrashort pulses,*” *New J. Phys.* **14**, 065003 (2012).
- [147] Z. Q. Yang, D. F. Ye, T. Ding, T. Pfeifer, and L. B. Fu, “*Attosecond XUV absorption spectroscopy of doubly excited states in helium atoms dressed by a time-delayed femtosecond infrared laser,*” *Phys. Rev. A* **91**, 013414 (2015).
- [148] Z.-C. Li, A. Jaron-Becker, and F. He, “*Superelastic rescattering in single ionization of helium in strong laser fields,*” *Phys. Rev. A* **94**, 043406 (2016).
- [149] R. Kosloff and H. Tal-Ezer, “*A direct relaxation method for calculating eigenfunctions and eigenvalues of the Schrödinger equation on a grid,*” *Chem. Phys. Lett.* **127**, 223 (1986).

- [150] F. Martín, “*Ionization and dissociation using B-splines: photoionization of the hydrogen molecule,*” *J. Phys. B* **32**, R197 (1999).
- [151] H. Bachau, E. Cormier, P. Decleva, J. E. Hansen, and F. Martín, “*Applications of B-splines in atomic and molecular physics,*” *Rep. Prog. Phys.* **64**, 1815 (2001).
- [152] J. C. Light, I. P. Hamilton, and J. V. Lill, “*Generalized discrete variable approximation in quantum mechanics,*” *J. Chem. Phys.* **82**, 1400 (1985).
- [153] T. N. Rescigno and C. W. McCurdy, “*Numerical grid methods for quantum-mechanical scattering problems,*” *Phys. Rev. A* **62**, 032706 (2000).
- [154] B. I. Schneider, L. A. Collins, and S. X. Hu, “*Parallel solver for the time-dependent linear and nonlinear Schrödinger equation,*” *Phys. Rev. E* **73**, 036708 (2006).
- [155] K. Balzer, S. Bauch, and M. Bonitz, “*Efficient grid-based method in nonequilibrium Green’s function calculations: Application to model atoms and molecules,*” *Phys. Rev. A* **81**, 022510 (2010).
- [156] T. J. Park and J. C. Light, “*Unitary quantum time evolution by iterative Lanczos reduction,*” *J. Chem. Phys.* **85**, 5870 (1986).
- [157] E. S. Smyth, J. S. Parker, and K. Taylor, “*Numerical integration of the time-dependent Schrödinger equation for laser-driven helium,*” *Comput. Phys. Commun.* **114**, 1 (1998).
- [158] X. Guan, O. Zatsarinny, K. Bartschat, B. I. Schneider, J. Feist, and C. J. Noble, “*General approach to few-cycle intense laser interactions with complex atoms,*” *Phys. Rev. A* **76**, 053411 (2007).
- [159] A. L. Frapiccini, A. Hamido, S. Schröter, D. Pyke, F. Mota-Furtado, P. F. O’Mahony, J. Madroñero, J. Eiglsperger, and B. Piraux, “*Explicit schemes for time propagating many-body wave functions,*” *Phys. Rev. A* **89**, 023418 (2014).
- [160] R. Kosloff and D. Kosloff, “*Absorbing boundaries for wave propagation problems,*” *J. Comput. Phys.* **63**, 363 (1986).
- [161] J. Muga, J. Palao, B. Navarro, and I. Egusquiza, “*Complex absorbing potentials,*” *Phys. Rep.* **395**, 357 (2004).

- [162] J. Caillat, J. Zanghellini, M. Kitzler, O. Koch, W. Kreuzer, and A. Scrinzi, “*Correlated multielectron systems in strong laser fields: A multiconfiguration time-dependent Hartree-Fock approach,*” *Phys. Rev. A* **71**, 012712 (2005).
- [163] J. Zanghellini, C. Jungreuthmayer, and T. Brabec, “*Plasmon signatures in high harmonic generation,*” *J. Phys. B* **39**, 709 (2006).
- [164] H. Miyagi and L. B. Madsen, “*Time-dependent restricted-active-space self-consistent-field theory for laser-driven many-electron dynamics,*” *Phys. Rev. A* **87**, 062511 (2013).
- [165] H. Miyagi and L. B. Madsen, “*Time-dependent restricted-active-space self-consistent-field theory for laser-driven many-electron dynamics. II. Extended formulation and numerical analysis,*” *Phys. Rev. A* **89**, 063416 (2014).
- [166] S. Bauch, L. K. Sørensen, and L. B. Madsen, “*Time-dependent generalized-active-space configuration-interaction approach to photoionization dynamics of atoms and molecules,*” *Phys. Rev. A* **90**, 062508 (2014).
- [167] S. Chattopadhyay, S. Bauch, and L. B. Madsen, “*Electron-correlation effects in enhanced ionization of molecules: A time-dependent generalized-active-space configuration-interaction study,*” *Phys. Rev. A* **92**, 063423 (2015).
- [168] C. W. McCurdy and C. K. Stroud, “*Eliminating wavepacket reflection from grid boundaries using complex coordinate contours,*” *Comput. Phys. Commun.* **63**, 323 (1991).
- [169] C. W. McCurdy, C. K. Stroud, and M. K. Wisinski, “*Solving the time-dependent Schrödinger equation using complex-coordinate contours,*” *Phys. Rev. A* **43**, 5980 (1991).
- [170] C. W. McCurdy, M. Baertschy, and T. N. Rescigno, “*Solving the three-body Coulomb breakup problem using exterior complex scaling,*” *J. Phys. B* **37**, R137 (2004).
- [171] L. Tao, W. Vanroose, B. Reps, T. N. Rescigno, and C. W. McCurdy, “*Long-time solution of the time-dependent Schrödinger equation for an atom in an electromagnetic field using complex coordinate contours,*” *Phys. Rev. A* **80**, 063419 (2009).
- [172] A. Scrinzi, “*Infinite-range exterior complex scaling as a perfect absorber in time-dependent problems,*” *Phys. Rev. A* **81**, 053845 (2010).

- [173] M. Weinmüller, M. Weinmüller, J. Rohland, and A. Scrinzi, “*Perfect absorption in Schrödinger-like problems using non-equidistant complex grids,*” *J. Comput. Phys.* **333**, 199 (2017).
- [174] L. B. Madsen, L. A. A. Nikolopoulos, T. K. Kjeldsen, and J. Fernández, “*Extracting continuum information from $\Psi(t)$ in time-dependent wave-packet calculations,*” *Phys. Rev. A* **76**, 063407 (2007).
- [175] L. Tao and A. Scrinzi, “*Photo-electron momentum spectra from minimal volumes: the time-dependent surface flux method,*” *New J. Phys.* **14**, 013021 (2012).
- [176] A. Scrinzi, “*t-SURFF: fully differential two-electron photo-emission spectra,*” *New J. Phys.* **14**, 085008 (2012).
- [177] L. Yue and L. B. Madsen, “*Dissociation and dissociative ionization of H_2^+ using the time-dependent surface flux method,*” *Phys. Rev. A* **88**, 063420 (2013).
- [178] G. Sansone, L. Poletto, and M. Nisoli, “*High-energy attosecond light sources,*” *Nat. Photon.* **5**, 655 (2011).
- [179] M. Chini, K. Zhao, and Z. Chang, “*The generation, characterization and applications of broadband isolated attosecond pulses,*” *Nat. Photon.* **8**, 178 (2014).
- [180] W. Ackermann, G. Asova, V. Ayvazyan, A. Azima, N. Baboi, J. Bähr, V. Balandin, B. Beutner, A. Brandt, A. Bolzmann, *et al.*, “*Operation of a free-electron laser from the extreme ultraviolet to the water window,*” *Nat. Photon.* **1**, 336 (2007).
- [181] B. W. McNeil and N. R. Thompson, “*X-ray free-electron lasers,*” *Nat. Photon.* **4**, 814 (2010).
- [182] F. Krausz and M. I. Stockman, “*Attosecond metrology: from electron capture to future signal processing,*” *Nat. Photon.* **8**, 205 (2014).
- [183] K. Toyota, O. I. Tolstikhin, T. Morishita, and S. Watanabe, “*Siegert-state expansion in the Kramers-Henneberger frame: Interference substructure of above-threshold ionization peaks in the stabilization regime,*” *Phys. Rev. A* **76**, 043418 (2007).
- [184] K. Toyota, O. I. Tolstikhin, T. Morishita, and S. Watanabe, “*Interference substructure of above-threshold ionization peaks in the stabilization regime,*” *Phys. Rev. A* **78**, 033432 (2008).

- [185] P. V. Demekhin and L. S. Cederbaum, “*Dynamic Interference of Photoelectrons Produced by High-Frequency Laser Pulses*,” *Phys. Rev. Lett.* **108**, 253001 (2012).
- [186] M. Bagheri, U. Saalman, and J. M. Rost, “*Essential Conditions for Dynamic Interference*,” *Phys. Rev. Lett.* **118**, 143202 (2017).
- [187] A. N. Artemyev, A. D. Müller, D. Hochstuhl, L. S. Cederbaum, and P. V. Demekhin, “*Dynamic interference in the photoionization of He by coherent intense high-frequency laser pulses: Direct propagation of the two-electron wave packets on large spatial grids*,” *Phys. Rev. A* **93**, 043418 (2016).
- [188] L. Yue and L. B. Madsen, “*Characterization of Molecular Breakup by Very Intense Femtosecond XUV Laser Pulses*,” *Phys. Rev. Lett.* **115**, 033001 (2015).
- [189] M. Yabashi, H. Tanaka, T. Tanaka, H. Tomizawa, T. Togashi, M. Nagasono, T. Ishikawa, J. R. Harries, Y. Hikosaka, A. Hishikawa, K. Nagaya, N. Saito, E. Shigemasa, K. Yamanouchi, and K. Ueda, “*Compact XFEL and AMO sciences: SACLA and SCSS*,” *J. Phys. B* **46**, 164001 (2013).
- [190] J. Feldhaus, M. Krikunova, M. Meyer, T. Möller, R. Moshhammer, A. Rudenko, T. Tschentscher, and J. Ullrich, “*AMO science at the FLASH and European XFEL free-electron laser facilities*,” *J. Phys. B* **46**, 164002 (2013).
- [191] C. Bostedt, J. D. Bozek, P. H. Bucksbaum, R. N. Coffee, J. B. Hastings, Z. Huang, R. W. Lee, S. Schorb, J. N. Corlett, P. Denes, P. Emma, R. W. Falcone, R. W. Schoenlein, G. Doumy, E. P. Kanter, B. Kraessig, S. Southworth, L. Young, L. Fang, M. Hoener, N. Berrah, C. Roedig, and L. F. DiMauro, “*Ultra-fast and ultra-intense x-ray sciences: first results from the Linac Coherent Light Source free-electron laser*,” *J. Phys. B* **46**, 164003 (2013).
- [192] B. Wolter, M. G. Pullen, M. Baudisch, M. Sclafani, M. Hemmer, A. Sentsleben, C. D. Schröter, J. Ullrich, R. Moshhammer, and J. Biegert, “*Strong-Field Physics with Mid-IR Fields*,” *Phys. Rev. X* **5**, 021034 (2015).
- [193] P. Colosimo, G. Doumy, C. Blaga, J. Wheeler, C. Hauri, F. Catoire, J. Tate, R. Chirila, A. March, G. Paulus, *et al.*, “*Scaling strong-field interactions towards the classical limit*,” *Nat. Phys.* **4**, 386 (2008).
- [194] T. Popmintchev, M.-C. Chen, D. Popmintchev, P. Arpin, S. Brown, S. Aliauskas, G. Andriukaitis, T. Balčiunas, O. D. Mücke, A. Pugzlys, A. Baltuška, B. Shim, S. E. Schrauth, A. Gaeta, C. Hernández-García, L. Plaja,

- A. Becker, A. Jaron-Becker, M. M. Murnane, and H. C. Kapteyn, “*Bright Coherent Ultrahigh Harmonics in the keV X-ray Regime from Mid-Infrared Femtosecond Lasers*,” *Science* **336**, 1287 (2012).
- [195] C. Hernández-García, J. A. Pérez-Hernández, T. Popmintchev, M. M. Murnane, H. C. Kapteyn, A. Jaron-Becker, A. Becker, and L. Plaja, “*Zeptosecond High Harmonic keV X-Ray Waveforms Driven by Midinfrared Laser Pulses*,” *Phys. Rev. Lett.* **111**, 033002 (2013).
- [196] C. I. Blaga, J. Xu, A. D. DiChiara, E. Sistrunk, K. Zhang, P. Agostini, T. A. Miller, L. F. DiMauro, and C. Lin, “*Imaging ultrafast molecular dynamics with laser-induced electron diffraction*,” *Nature* **483**, 194 (2012).
- [197] M. G. Pullen, B. Wolter, A.-T. Le, M. Baudisch, M. Hemmer, A. Senftleben, C. D. Schröter, J. Ullrich, R. Moshhammer, C.-D. Lin, *et al.*, “*Imaging an aligned polyatomic molecule with laser-induced electron diffraction*,” *Nat. Commun.* **6**, 7262 (2015).
- [198] B. Wolter, M. G. Pullen, A.-T. Le, M. Baudisch, K. Doblhoff-Dier, A. Senftleben, M. Hemmer, C. D. Schröter, J. Ullrich, T. Pfeifer, R. Moshhammer, S. Gräfe, O. Vendrell, C. D. Lin, and J. Biegert, “*Ultrafast electron diffraction imaging of bond breaking in di-ionized acetylene*,” *Science* **354**, 308 (2016).
- [199] M. Awasthi, Y. V. Vanne, A. Saenz, A. Castro, and P. Decleva, “*Single-active-electron approximation for describing molecules in ultrashort laser pulses and its application to molecular hydrogen*,” *Phys. Rev. A* **77**, 063403 (2008).
- [200] I. A. Ivanov and A. S. Kheifets, “*Harmonic generation for atoms in fields of varying ellipticity: Single-active-electron model with Hartree-Fock potential*,” *Phys. Rev. A* **79**, 053827 (2009).
- [201] M. Abu-samha and L. B. Madsen, “*Single-active-electron potentials for molecules in intense laser fields*,” *Phys. Rev. A* **81**, 033416 (2010).
- [202] L. A. A. Nikolopoulos, T. K. Kjeldsen, and L. B. Madsen, “*Three-dimensional time-dependent Hartree-Fock approach for arbitrarily oriented molecular hydrogen in strong electromagnetic fields*,” *Phys. Rev. A* **76**, 033402 (2007).
- [203] R. Kopold, W. Becker, and M. Kleber, “*Quantum path analysis of high-order above-threshold ionization*,” *Opt. Commun.* **179**, 39 (2000).

- [204] C. Figueira de Morisson Faria, H. Schomerus, and W. Becker, “*High-order above-threshold ionization: The uniform approximation and the effect of the binding potential,*” *Phys. Rev. A* **66**, 043413 (2002).
- [205] D. B. Milošević, G. G. Paulus, and W. Becker, “*Ionization by few-cycle pulses: Tracing the electron orbits,*” *Phys. Rev. A* **71**, 061404 (2005).
- [206] D. B. Milošević, E. Hasović, M. Busuladžić, A. Gazibegović-Busuladžić, and W. Becker, “*Intensity-dependent enhancements in high-order above-threshold ionization,*” *Phys. Rev. A* **76**, 053410 (2007).
- [207] D. B. Milošević, “*Reexamination of the improved strong-field approximation: Low-energy structures in the above-threshold-ionization spectra for short-range potentials,*” *Phys. Rev. A* **88**, 023417 (2013).
- [208] R. Kopold, W. Becker, H. Rottke, and W. Sandner, “*Routes to Nonsequential Double Ionization,*” *Phys. Rev. Lett.* **85**, 3781 (2000).
- [209] C. Figueira de Morisson Faria, H. Schomerus, X. Liu, and W. Becker, “*Electron-electron dynamics in laser-induced nonsequential double ionization,*” *Phys. Rev. A* **69**, 043405 (2004).
- [210] T. Shaaran, M. T. Nygren, and C. Figueira de Morisson Faria, “*Laser-induced nonsequential double ionization at and above the recollision-excitation-tunneling threshold,*” *Phys. Rev. A* **81**, 063413 (2010).
- [211] T. Shaaran, C. Figueira de Morisson Faria, and H. Schomerus, “*Causality and quantum interference in time-delayed laser-induced nonsequential double ionization,*” *Phys. Rev. A* **85**, 023423 (2012).
- [212] A. S. Maxwell and C. Figueira de Morisson Faria, “*Quantum interference in time-delayed nonsequential double ionization,*” *Phys. Rev. A* **92**, 023421 (2015).
- [213] A. S. Maxwell and C. Figueira de Morisson Faria, “*Controlling Below-Threshold Nonsequential Double Ionization via Quantum Interference,*” *Phys. Rev. Lett.* **116**, 143001 (2016).
- [214] K. L. Ishikawa and T. Sato, “*A Review on Ab Initio Approaches for Multi-electron Dynamics,*” *IEEE J. Sel. Top. Quantum Electron.* **21**, 1 (2015).
- [215] D. J. Haxton, K. V. Lawler, and C. W. McCurdy, “*Multiconfiguration time-dependent Hartree-Fock treatment of electronic and nuclear dynamics in diatomic molecules,*” *Phys. Rev. A* **83**, 063416 (2011).

- [216] D. J. Haxton, K. V. Lawler, and C. W. McCurdy, “*Single photoionization of Be and HF using the multiconfiguration time-dependent Hartree-Fock method,*” *Phys. Rev. A* **86**, 013406 (2012).
- [217] L. Greenman, P. J. Ho, S. Pabst, E. Kamarchik, D. A. Mazziotti, and R. Santra, “*Implementation of the time-dependent configuration-interaction singles method for atomic strong-field processes,*” *Phys. Rev. A* **82**, 023406 (2010).
- [218] A. Karamatskou, S. Pabst, Y.-J. Chen, and R. Santra, “*Calculation of photoelectron spectra within the time-dependent configuration-interaction singles scheme,*” *Phys. Rev. A* **89**, 033415 (2014).
- [219] J. J. Omiste, W. Li, and L. B. Madsen, “*Electron correlation in beryllium: Effects in the ground state, short-pulse photoionization, and time-delay studies,*” *Phys. Rev. A* **95**, 053422 (2017).